AN INVESTIGATION OF THE DIFFUSE GAS IN THE INTERSTELLAR MEDIUM

Thesis submitted for the degree of
Doctor of Philosophy
at the University of Leicester.

by

Ian B. Hutchinson
X-ray Astronomy Group
Department of Physics and Astronomy
University of Leicester

January 1999

ProQuest LLC
789 East Eisenhower Parkway
P.O. Box 1346
Ann Arbor, MI 48106-1346

Declaration

I hereby declare that no part of this thesis has been previously submitted to this or any other university as part of the requirement for a higher degree. The work described herein was conducted by the undersigned except for contributions from colleagues and other workers who are acknowledged in the text.

Ian B. Hutchinson

January 1999

AN INVESTIGATION OF THE DIFFUSE GAS IN THE INTERSTELLAR MEDIUM

Ian B. Hutchinson

ABSTRACT

This thesis considers the nature of the diffuse gas in the interstellar medium. In Chapter 3, the ROSAT EUV/X-ray spectra of 1987 late-type stars are studied in detail so that the absorption along the line of sight can be determined. Using two-colour plots, it is shown that the data are best described by two temperature coronal models, although no single model provides an adequate fit for all the sources.

These data are combined with Hipparcos parallaxes and a further 490 sources from other published data sets in Chapter 4 to investigate the distribution of cool gas within 400 pc of the Sun. Using a spherical harmonic analysis it is shown that the best fit is obtained for a non-spherical cavity model in which the Solar System resides in a region of space with a density typically between 0.045 cm^{-3}-0.08 cm^{-3}. The average radius of the cavity is 60 pc although it varies between 29-280 pc with sky direction.

Chapters 5 and 6 consider the X-ray emission from hot components of the diffuse gas. It is shown that spatial fluctuations with a magnitude of 1σ=4% are observed across the sky and that they cannot be explained by source confusion or background subtraction errors alone. A spectral analysis indicates that they are possibly caused by "clumps" of gas in the Galactic halo, although the possibility that they are caused by differential absorption across the field of view cannot be ruled out.

In Chapter 7, the techniques used to calibrate the CCD's to be flown on the CUBIC satellite are presented. A combination of laboratory measurements and semiconductor modelling are used to produce response matrices for post launch data analysis.

Publications

Hutchinson I.B., Warwick R.S., Willingale R. 1997, 'The Local Bubble and Beyond' Proc. Garching conference. "Mapping Cool Gas in the ISM with ROSAT"

Warwick R.S., Hutchinson I.B., Willingale R., Kuntz K., Snowden S., 1997, 'The Local Bubble and Beyond' Proc. Garching conference. "Tracing Small-Scale Fluctuations in the Soft X-ray Background"

Contents

Chapter 1

The Structure of the Interstellar Medium

Overview

In this chapter, the nature of the diffuse gas found in the Milky Way is discussed and a detailed description of its various phases and their interaction is presented. The current perception of the interstellar structure derived from radio, infrared, optical and EUV observations is summarised while the information offered by X-ray observations is discussed in detail.

1.1 Introduction

The Milky Way is an evolving system with a complex structure governed by the interaction of stars, interstellar gas and dust. Gravitational forces constrain the majority of its mass to an orbital plane although some material extends well above (and below) the disc to form a Galactic halo. Studies of the distribution of bright O and B stars have indicated that our Galaxy is an Sbc spiral (diameter$\sim$30 kpc) and that the Solar System is situated in an inter-arm region $\sim$8.5 kpc from the central nucleus.

This thesis is concerned with the properties and distribution of the interstellar gas, and more particularly, with what we can learn about it from EUV and X-ray observations. The current chapter gives a review of the information gathered from previous studies at these and other wavelengths and describes the physical processes that are relevant to the study of X-rays.

1.2 The components of the interstellar medium

The interstellar medium (ISM) is a dynamic medium consisting of gas, plasma, dust, high energy particles and magnetic fields. These components are in a state of continual change, with supernovae and stellar winds pumping heated material into some regions and star formation removing it from others (see Longair (1994) for a general discussion). Here, the four main constituents of the ISM are reviewed before their detailed interaction is discussed.

1.2.1 Gas

The interstellar gas exists in atomic, molecular and ionised forms and has an approximately cosmic composition (by mass: 74% hydrogen, 24% helium and 1-2% heavier elements). The individual characteristics and distributions of each one of these phases are discussed below:

Molecular. The molecular gas is found in the form of giant clouds and is distributed throughout the Milky Way although generally confined to the Galactic plane. The gas is extremely dense, containing about 40% of the ISM by mass but filling only half a percent of it by volume. The clouds consist mainly of molecular hydrogen although many other molecular species such as CO and NH_3 have also been observed. A typical cloud has a mass of 10^6 $M_\odot$ and a temperature between 10-100 K. It is within these dense regions that star formation is thought to take place.

Atomic. The atomic phase of the gas is also generally confined to the plane but can be found throughout the Galaxy. It is observed in two forms; firstly as cool (T$\sim$80 K) diffuse clouds with densities approaching 10^6 m^{-3}, and secondly as a hotter (T$\sim$8000 K) inter-cloud medium occupying over 40% of the ISM's volume. At these high temperatures, this second form is usually accompanied by ionised gas (HII).

Ionised. The hot plasma components generally have temperatures above 10^4 K and can be observed around young or hot, dying stars where the gas is shock heated to temperatures of about 10^5 K or as bubbles of "coronal" gas at $\sim 10^6$ K, formed by supernovae. Additionally, as indicated above, HII is also found in the tenuous inter-cloud medium. It is thought that it was formed from gas previously heated by a stellar remnant which has pervaded the cooler regions and as a consequence of its buoyancy with respect to the cooler gas, it extends much further out of the plane.

1.2.2 Dust

Nearly one percent of the mass of the ISM is in the form of solid dust grains. These are found throughout the Galaxy with a typical size of 10^{-5} cm. They are thought to be a fundamental ingredient in the requirements for star formation (they allow a protostar to radiate energy and protect molecules from radiation which would otherwise break them apart). Their presence was first inferred from their obscuring effects on optical images of stellar sources. However they are also identified from their infrared emission (with a characteristic temperature of 30-500 K) and their polarising effects on starlight. The grains have various compositions, but consist predominantly of the heavier elements present in the interstellar medium. Depending on their size, the grains are strong absorbers at

wavelengths between the ultraviolet and infrared.

1.2.3 High Energy Particles

Very high energy particles (e.g. cosmic rays) are found throughout the galaxy. They can be observed through the synchrotron emission they radiate when spiralling through magnetic fields or through the gamma rays emitted during collisions with components of the interstellar gas. It is thought that the particles gain their high energies in supernova explosions or pulsars.

1.2.4 Magnetic Field

It is from observations of the synchrotron emission emitted by some of the high energy particles discussed above, that the presence of a large-scale, relatively weak Galactic magnetic field was first inferred (B$\sim 10^{-10}$-10^{-8} T). Its presence is also verified by the Zeeman splitting of the 21cm line of neutral hydrogen and the polarisation effects of dust on starlight.

1.3 Structure of the ISM

At the temperatures and densities of the phases outlined above, the interstellar gas is in approximate pressure equilibrium with $\frac{P}{k} \sim 10^4$ cm^{-3} K. An interesting aspect of the ISM is the apparent stability of the gas and plasma temperatures described above. The reason for the stability of these phases can be explained as follows (see Longair (1994) for a more complete description of the work by Field, Goldsmith & Habing (1969)).

At equilibrium, the rates of heating and cooling are equal (in the ISM, the cooling is due to radiation from both electronic transitions and bremsstrahlung while the heating rate is due to ionisation losses of low energy cosmic rays and shock heating from supernova remnants or stellar winds). An analysis by Field, Goldsmith & Habing (1969) shows that a particular state is unstable if the heat loss decreases with increasing temperature. That is, if the density of a region of gas increases, then (through the mechanisms of bremsstrahlung

and electronic transitions) the rate of heat loss increases so that the region contracts. This contraction is only stable if the pressure that the region reaches maintains pressure equilibrium with its surroundings.

Using this analysis, Field, Goldsmith & Habing (1969) were able to infer that temperatures of 80K and 8000 K result in stable phases of the gas. These temperatures are clearly in good agreement with those observed.

Observations of high velocity clouds in the Galactic halo have questioned the picture of a completely static ISM in pressure equilibrium. These clouds, observed through their 21cm emission and spectral lines associated with the CO molecule, are seen to fall towards the Galactic plane. One model that does satisfy the co-existence of gas at very different temperatures and the falling of cool clouds towards the Galactic plane is described by Spitzer (1978); it is thought that shock heating by supernova remnants forms "bubbles" of highly ionised tenuous gas which, because of their buoyancy relative to the gas of the cooler clouds, expand and rise into the Galactic halo. Slight local compression then leads to increased cooling which, through thermal instability, cause the formation of cooler clouds which then fall back down to the disc completing a "Galactic fountain" cycle.

1.4 Observations into the ISM

1.4.1 Radio

It is at radio wavelengths that most has been learned about the distribution of atomic hydrogen in the Milky Way. Neutral hydrogen emits radiation through a hyperfine transition in which the spins of the electron and proton change from a parallel to anti-parallel configuration. The small energy separation of these two states results in the emission of a photon with a wavelength in the radio regime. This 21cm line is one of only two direct tracers of neutral hydrogen. Since the Galaxy is almost transparent at these energies, information can be obtained on material distributed across the entire Galaxy. Observations of the Galactic disk at 21cm have shown that the neutral hydrogen closely follows the spiral arm structure outlined by the O and B stars while observations perpendicular to

this plane show that it forms a very flat disk, with a half density height of about 240 pc (see Figure 1.1).

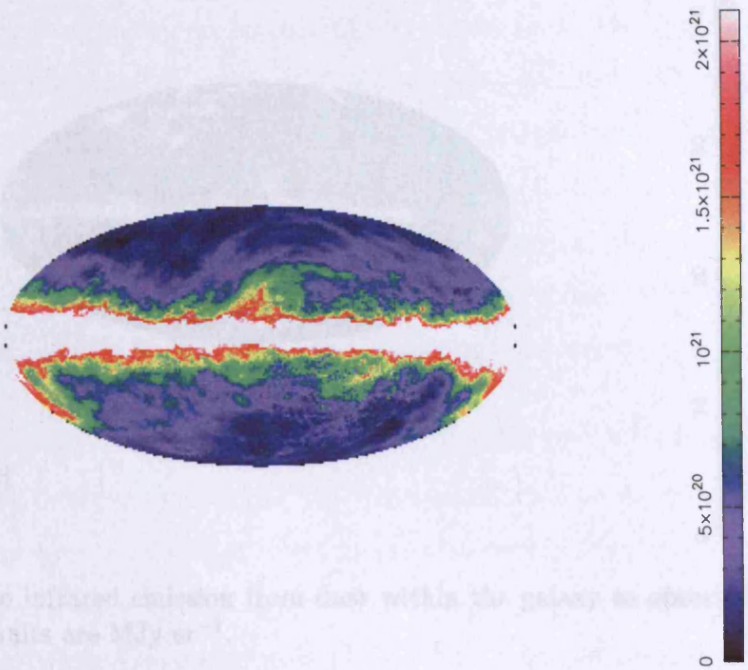

Figure 1.1: The 21cm view of the galaxy (Dickey & Lockman 1990). The units are atoms cm^{-2}.

1.4.2 Infrared

It is in the infrared regime that the rotational and molecular transitions of molecules can be detected. Consequently, observations at these wavelengths map out the distribution of the cool, dense molecular clouds. It is actually the emission from the CO molecule that is most prevalent, and since it generally only form in regions where H_2 also forms it provides an indirect tracer with which to map out the distribution of molecular hydrogen. CO maps show that the molecular hydrogen is confined very closely to the disk with a half density height of 120 pc, forming a thick ring between radii of 3 and 8 kpc. At these wavelengths it also possible to trace the distribution of dust through its infrared emission and the 100 μm view of this determined by the IRAS satellite is shown in Figure 1.2.

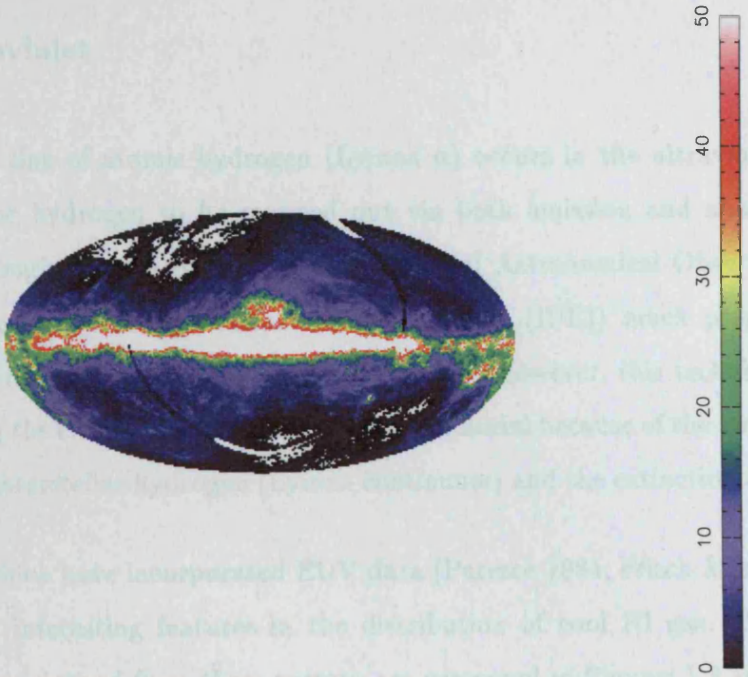

Figure 1.2: The infrared emission from dust within the galaxy as observed by the IRAS satellite. The units are MJy sr^{-1}.

1.4.3 Optical

The first indications that material might occupy the vast space between stars came from optical studies of stellar sources which revealed the reddening effects of dust. The presence of absorption features (due to sodium and calcium atoms) in stellar spectra, shown not to be associated with the stellar source (stationary lines), provided further evidence. Unfortunately, the absorption due to dust (optical extinction) in the plane of the ISM prevents the analysis of material any further out than 500 pc so that optical studies in these directions are limited to the local ISM. In fact, the interstellar reddening caused by dust absorption can also be used to determine the column density of HI along the line-of-sight to a stellar source. A study by Heiles, Kulkarni & Stark (1981) has shown that if the line-of-sight absorption is dominated by neutral hydrogen then interstellar reddening, E(B-V), and N_H, are related by $\frac{N_H}{E(B-V)} \sim 6\times 10^{21}$ mag^{-1} atoms cm^{-2}. However, the values obtained for N_H using this relationship can be inaccurate by up to a factor of two because of assumptions about the zero point of reddening and the abundance ratio of atomic to molecular hydrogen.

1.4.4 Ultraviolet

The resonance line of atomic hydrogen (Lyman α) occurs in the ultraviolet wave-band, allowing atomic hydrogen to be mapped out via both emission and absorption at UV energies. Through a series of observatories (Orbital Astronomical Observatory (OAO), Copernicus and International Ultraviolet Observatory (IUE)) much progress has been made in this area during the past couple of decades. However, this technique only offers information on the closest few hundred parsecs of material because of the strong continuum absorption of interstellar hydrogen (Lyman continuum) and the extinction caused by dust.

Two studies which have incorporated EUV data (Paresce 1984; Frisch & York 1983) have revealed some interesting features in the distribution of cool HI gas. The HI column density contours derived from these surveys are presented in Figures 1.3 and 1.4, where it can be seen that the Solar System appears to be located in a region of the local interstellar medium (LISM) where the density ($\sim$0.07 cm^{-3}) is much less than that typically found beyond 100 pc. It is also clear from these figures that the cavity is far from uniform. Its walls appear to approach to within 10 pc in the direction of the Galactic centre, while they are as far out as 150 pc in the direction of the star, βCMa (l^{II}=225 degrees). In addition, it is also known that the material within the cavity is far from homogeneous. For example, it has been shown (using studies of the backscattering of solar Hydrogen Lyman and Helium I) that the solar system resides in a local cloud of material (sometimes referred to as the "Local Fluff") which has a significantly greater density ($n \sim 0.1$ cm^{-3}) than generally found within the cavity described above. It is thought that this material extends out to $\sim$10 pc in most directions and has a temperature of $\sim 10^4$K.

As a result of the large photo-electric absorption cross sections associated with these energies, the distribution of the most local absorbing material can also be probed using the source counts and spatial distributions of EUV sources, typically; white dwarfs and late-type stars. This has been completed for the sources observed by both the ROSAT WFC (Warwick *et al.* 1993) and EUVE (Vallerga 1996). Results from these studies confirm that the Solar System is located in a low density ($n \sim 0.05$ cm^{-3}) cavity which has an average radius of $\sim$ 80 pc and exterior density of ($n \sim 0.50$ cm^{-3}). However, three regions of variance are also identified: towards the Galactic centre the distance to the cavity wall

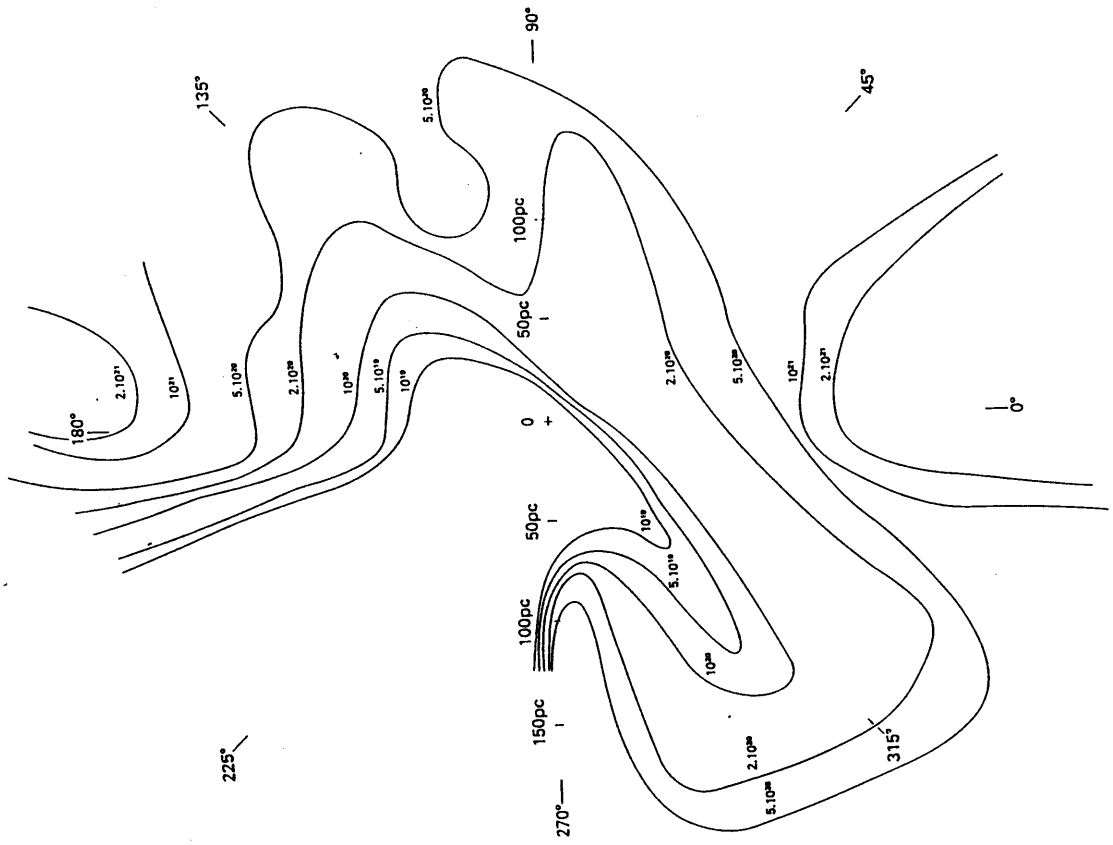

Figure 1.3: The N_H contours derived by Paresce (1984).

is less than 20 pc, towards the high positive latitude region in the direction of l^{II}=140° the cavity extends to ~120 pc and towards the high negative latitude region in the direction of l^{II}=220°, the cavity edge is 100-150 pc distant.

Since a very large number of high energy transitions of interstellar atoms and molecules are observed at these energies (eg. OVI associated with hot HII regions) the interstellar abundances, ionisation states and temperatures of the heavy elements can be investigated in detail using EUV observations. Particularly interesting results of such studies include; the fact that the interstellar abundances of heavy elements are found to be less than their cosmic values by factors of up to $10^3 - 10^4$ and that the abundance of deuterium relative to neutral hydrogen is fairly constant. A general discussion of these points can be found in (Spitzer & Jenkins 1975) which describes some of the results obtained with data from the Copernicus satellite.

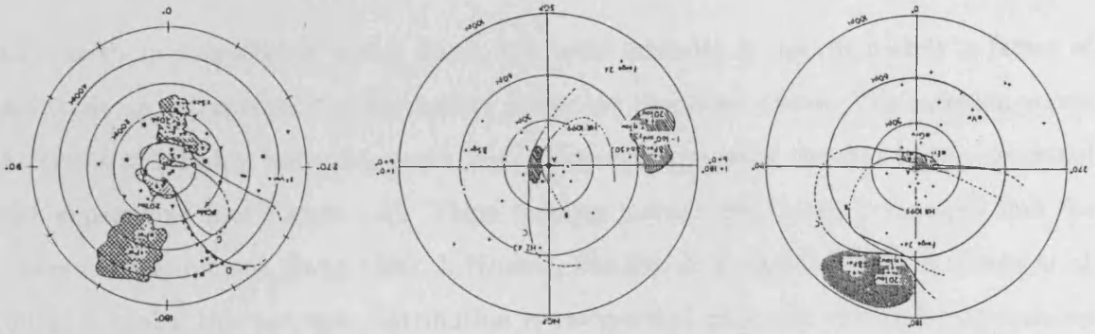

Figure 1.4: The N_H contours derived by Frisch & York (1983). Contour A is for N_H=5×10^{17} cm^{-2}, contour B is for N_H=2.5×10^{18} cm^{-2}, contour C is for N_H=5×10^{18} cm^{-2} and contour D is for N_H=5×10^{19} cm^{-2}. The symbols, which represent individual measurements correspond to: small dots=5-25×10^{17} cm^{-2}, large dots=25-50×$10^{17}$$cm^{-2}$, crosses=> 5×$10^{18}$$cm^{-2}$, open circles=<5×$10^{18}$$cm^{-2}$, open triangles=5-50×$10^{18}$$cm^{-2}$, filled circles=5-10×$10^{19}$$cm^{-2}$, filled triangles=1-5×$10^{20}$$cm^{-2}$ and filled squares=5-10×$10^{20}$$cm^{-2}$.

1.4.5 X-ray

All-sky X-ray surveys have been conducted in various energy bands over the past few years. Images with the best spatial resolution (all-sky) have been produced by the recent ROSAT all-sky survey. These were obtained in the three relatively independent energy bands; the 0.25 keV (see Figure 1.5), 0.75 keV (see Figure 1.6) and 1.5 keV (Snowden *et al.* 1997) and these bands are also used below to review the current interpretations of these observations.

1.5 keV. Apart from some faint Galactic features (see for example; Warwick, Pye & Fabian 1980; Worral *et al.* 1982; Iwan *et al.* 1982), the emission in this band is fairly isotropic and thought to originate from various populations of extragalactic sources. The

energy spectrum of these sources is fairly well modelled by a power law with photon index $\sim$ 1.7 (see Georgantopoulos *et al.* 1996). It is not clear exactly which source populations contribute (Fabian & Barcons 1992), but it is has been shown that the majority of the soft X-ray sources so far resolved from the background are AGN(QSOs and Seyfert 1 galaxies), (Georgantopoulos *et al.* 1996).

0.75 keV. In this slightly softer band, the total intensity is approximately a factor of two above an extrapolation of the harder power law described above. The emission across the sky is still highly isotropic, apart from a few enhancements thought to be associated with supernovae (see Figure 1.5). These features include the North Polar Spur and the Eridanus enhancement (Iwan 1980; J. Nousek, Sanders & Kraushaar 1982; Burrows *et al.* 1993). Actually, this isotropic distribution is unexpected, since any extragalactic emission should be highly attenuated by the cool gas in the Galactic plane. Consequently, these observations have led to the suggestion that there must be a more local source of emission which enhances the reduced extragalactic intensity expected in this region (J. Nousek, Sanders & Kraushaar 1982). It is thought that a hot tenuous Galactic halo (Spitzer 1956; Shapiro & Field 1976; Cox 1981) is the most likely form for this material.

0.25 keV. Observations of the diffuse intensity in the softer X-ray band have shown it to be a factor of three above an extrapolation of the hard extra galactic source contribution. This additional intensity is thought to originate from a hot 10^6K gas (Rocchia *et al.* 1984; Hasinger 1992; Bloch *et al.* 1986) that fills the local cavity, rather than from a distant absorbed source. This is primarily because, even though there is a distinct correlation between X-ray intensity and latitude (and hence HI column density); (see Figure 1.5), its depth does not agree with predictions based on current estimates of atomic cross sections. Theoretically, this could be accounted for by clumping of the absorbing gas, but multiple attempts to observe such clumping have failed (Jahoda *et al.* 1985; Jahoda, McCammon & Lockman 1986).

Instead, a displacement model was proposed to explain the observed correlation (Sanders *et al.* 1977, Fried *et al.* 1980 and Snowden *et al.* 1990).

In this model it is suggested that increases in X-ray intensity are attributed to increases

is the path length of the emitting material such that high intensity regions are associated with extended regions of hot X-ray emitting gas which have displaced the cool gas in the ISM. Not only does this mechanism produce the required change in X-ray intensity with Galactic latitude, but it also approaches the correct depth of correlation. Current arguments centre on how this cavity was originally formed and how the gas inside it was heated to such a high temperature. It is predicted that an energy of at least 4×10^{50} ergs (Snowden *et al.* 1990; Cox & Reynolds 1987) would be required. The most favourable model is one in which a supernovae occurred in a region of the ISM where a previous remnant had already reduced its density to about 0.004 cm^{-3}. The most recent remnant would then still be actively expanding, shock heating any gas it encounters to X-ray emitting temperatures (Cox & Anderson 1982). The variation of X-ray intensity with latitude would be accounted for by the reduced amount of material impeding the progress of the blast wave at higher latitudes.

The most recent results from an analysis of the ROSAT all-sky survey data in this band (Snowden *et al.* 1998) suggest that the emission temperature of the gas within the local bubble peaks at $\sim10^6$K with an intensity that varies by up to a factor of three with Galactic latitude. In addition it has been shown in several studies of these data that extensive 0.25 keV emission arises from within the Galactic halo (Burrows & Mendenhall 1991; Snowden *et al.* 1991). The emission temperature of the gas in the halo also peaks at around 10^6K while the emission can be seen to vary by up to a factor of two over angular scales of $\sim20^o$.

A detailed analysis of the X-ray emission at these energies has revealed fluctuations which are not associated with the distribution of cool, absorbing gas (Barber 1994). These have been associated with both "bubbles" of hot gas in the field of view and non-equilibrium emission, which are probably associated with the shock front of the active blast wave.

1.5 X-ray emission

High temperature, low density plasmas are optically thin and consequently their emission spectrum is the sum of many microscopic processes. These include bremsstrahlung

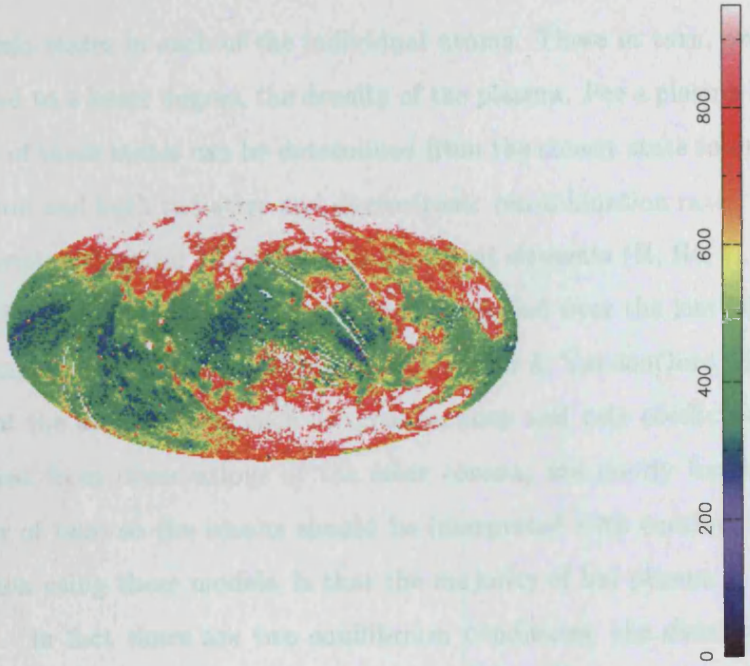

Figure 1.5: The image of the 0.25 keV X-ray background derived from the ROSAT all-sky survey. The units are 10^{-6} counts s^{-1} cm^{-2}.

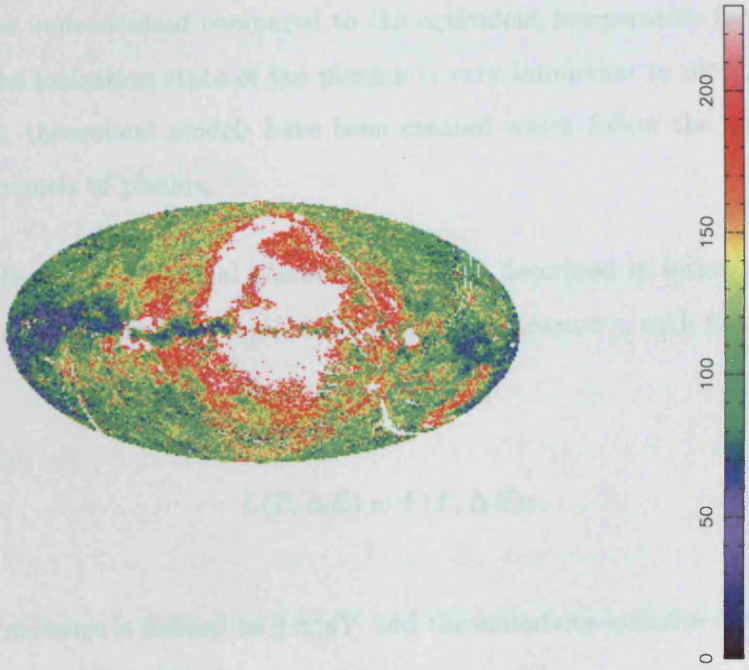

Figure 1.6: The image of the 0.75 keV X-ray background derived from the ROSAT all-sky survey. The units are 10^{-6} counts s^{-1} cm^{-2}.

from electrons and ions as well as emission from individual electronic transitions. At lower temperatures, metals retain more and more of their electrons so line emission tends to dominate the emissivity. The detailed spectrum depends on the populations of the

various electronic states in each of the individual atoms. These in turn, are a function of temperature and to a lesser degree, the density of the plasma. For a plasma in equilibrium, the population of these states can be determined from the steady state solution of electron impact ionisation and both radiative and di-electronic recombination rates. Spectral models, which determine these for 13 of the most abundant elements (H, He, C, N, O, Ne, Mg, Si, S, Ar, Ca, Fe and Ni) in the ISM have been developed over the last 20 years (see for example, Raymond & Smith 1977; Mewe, Gronenschild & VandenOord 1985). However, the majority of the atomic data, such as cross sections and rate coefficients, which have been determined from observations of the solar corona, are poorly known (accurate to within a factor of two) so the results should be interpreted with caution. A major point to consider when using these models, is that the majority of hot plasma in the ISM is not in equilibrium. In fact there are two equilibrium conditions; the distribution of energy between ions and electrons and the distribution of ionisation states. Even in very hot plasmas, the time-scales for ionising heavy elements are very long (typically 10^4 years) so they tend to be under-ionised compared to the equivalent temperature for an equilibrium state. Since the ionisation state of the plasma is very important in determining the correct emissivity, theoretical models have been created which follow the ionisation history of individual parcels of plasma.

The emission from an isothermal plasma is generally described in terms of its emissivity, F (power per unit emission measure) and an emission measure ϵ, such that the luminosity is given by:

$$L(T, \Delta E) = F(T, \Delta E)\epsilon$$

The emission measure is defined as $\int n_e^2 dV$ and the emissivity includes contributions from both continuum and line emission.

The emission spectra determined from the Raymond and Smith (Raymond & Smith 1977) and Mewe (Mewe, Gronenschild & VandenOord 1985) codes (these are referred to as the *raymond* and *mekal* models in the XSPEC spectral fitting package) are plotted as a function of energy in Figure 1.7 for a 10^6K plasma.

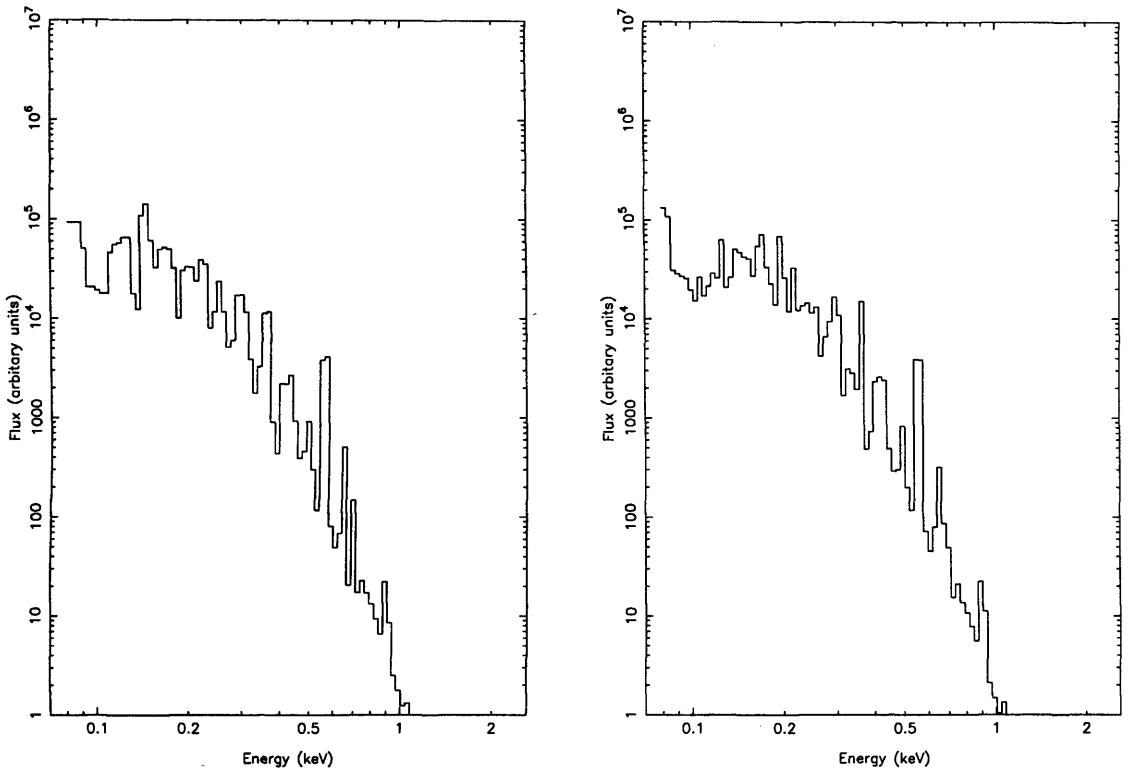

Figure 1.7: The energy spectra of a thermal plasma at 10^6 K derived using the Raymond & Smith code (left) and the Mewe code (right).

1.6 X-ray Absorption

The dominant interaction with matter for soft X-rays is photo-electric absorption. The cross sections and edge energies for each atom in the ISM are dependent on the ionisation state of the material. These have been calculated for the 13 most abundant elements in the ISM (see above) by Morrison & McCammon (1983) and are used for the work throughout this thesis. The total amount of absorption along the line of sight is expressed in terms of the total column density of Hydrogen, N_H, with the contributions from the heavier elements determined from their relative abundances, such that, the effective cross section per hydrogen atom is given by:

$$\sigma_{eff} = \Sigma \frac{n_i \sigma_i}{n_H}$$

where n_H is the density of neutral hydrogen, n_i is the density of element i and σ_i is the elements absorption cross-section. Consequently, the total transmission (T) can be

written:

$$T = e^{-\sigma_{eff} N_H}$$

where N_H is the total column density towards a particular source and is defined as:

$$N_H = \int n(l) dl$$

Here, $n_H(l)$ represents the distribution in hydrogen density along the line-of-sight and l is the distance along the line-of-sight.

A plot of the variation in transmission as a function of energy is given in Figure 1.8 for column densities of 10^{19}, 5×10^{19}, 10^{20} and 5×10^{20} atoms cm^{-2} and the cross sections determined by Morrison & McCammon (1983). The effects that such column densities have on the spectrum of a 10^6K plasma (using the Raymond-Smith code) can be seen in Figure 1.9.

1.7 Thesis Outline

The next chapter describes the satellites and instruments which have produced the data used in this thesis. Future missions which will have an impact on the field are also briefly reviewed. The third chapter discusses the effects of line-of-sight absorption on the observed EUV/X-ray spectra of late-type stars and presents the results of spectral modelling of a sample of such sources. Chapter four describes an investigation of the distribution of cool gas in the local interstellar medium using the column density estimates derived in Chapter three together with other published column density measurements. Chapter five presents a detailed study of the diffuse X-ray emission observed by the ROSAT PSPC in the direction of the Lockman Hole, particularly the small scale ($\sim 20'$) fluctuations seen in deep pointings. In Chapter six, a further six deep ROSAT PSPC fields are analysed to determine if the fluctuations in X-ray emission are observed globally. Chapter seven considers the detailed spectroscopic calibration and simulations of the CCD's to be launched on the

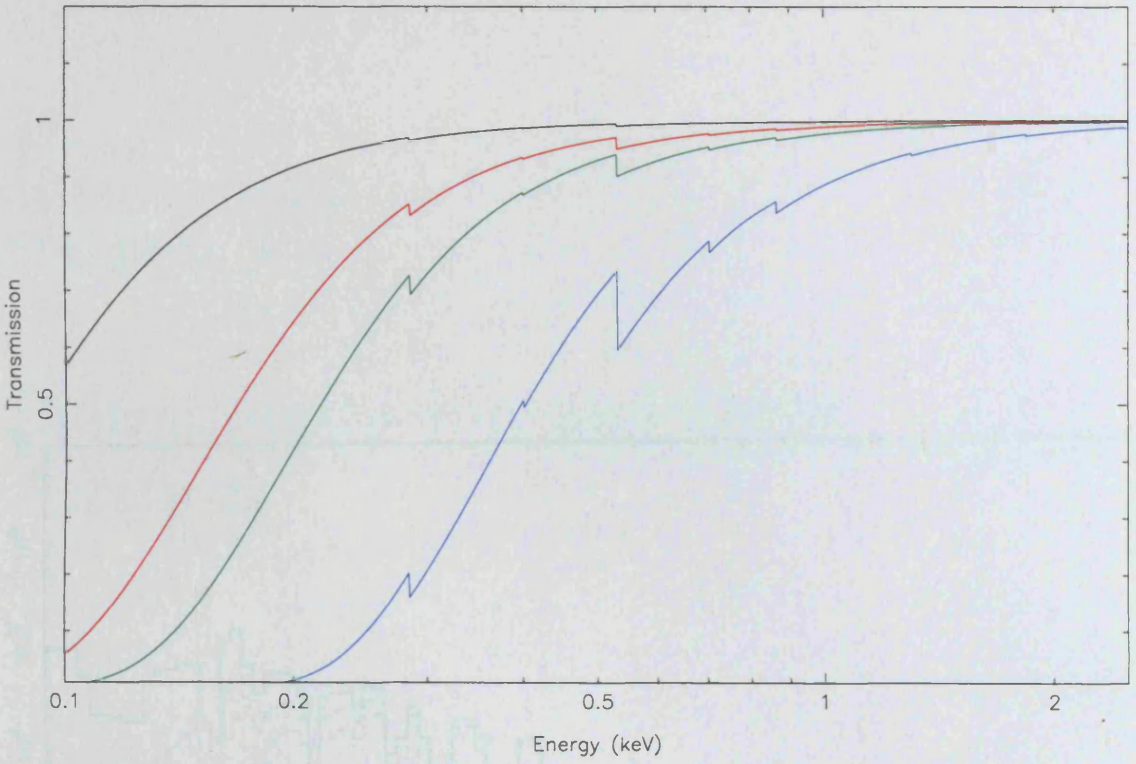

Figure 1.8: The transmission as a function of energy for column densities of 10^{19} atoms cm^{-2} (top), $5\times$ 10^{19} atoms cm^{-2}, 10^{20} atoms cm^{-2} and $5\times$ 10^{20} atoms cm^{-2} (bottom) derived from the Morrison & McCammon (1983) cross sections.

CUBIC satellite (Cosmic Unresolved X-ray Background Instrument using CCD's). Finally, Chapter eight provides general conclusions to all the work presented as well as some simulations which show what we expect to learn from future observations of the interstellar gas.

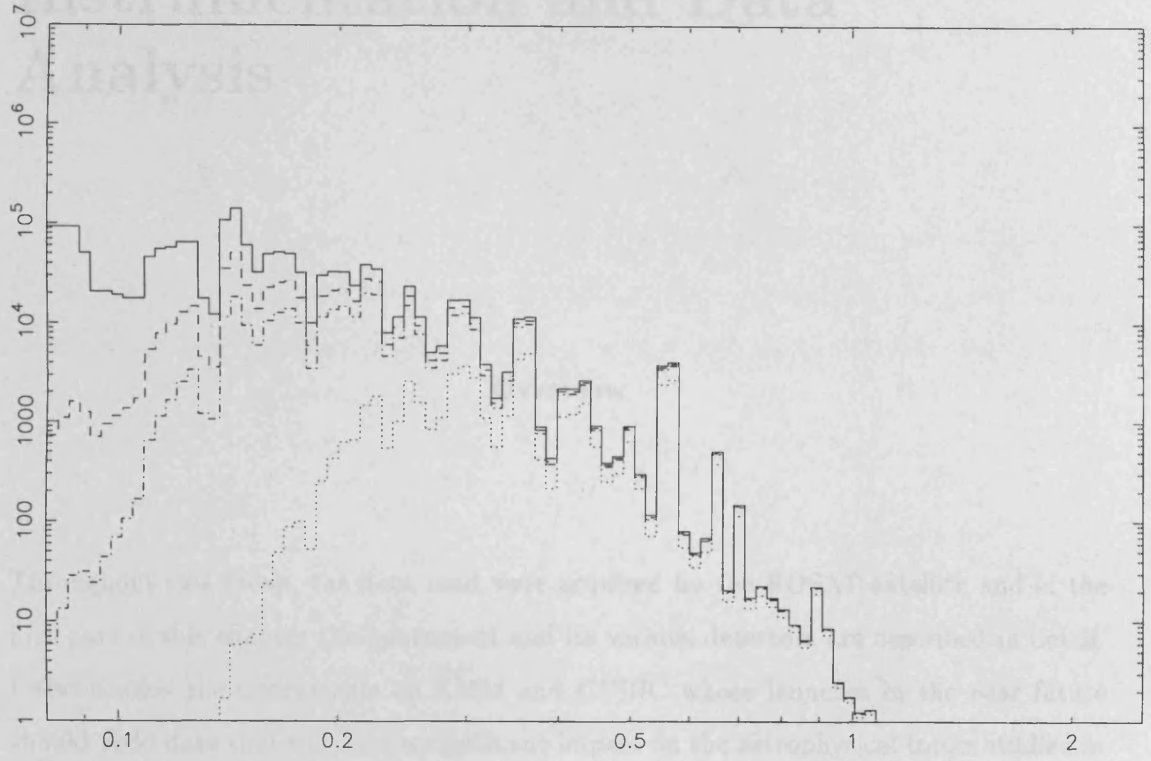

Figure 1.9: The absorbed spectra of a 10^6K plasma (using the Raymond-Smith code) for column densities of 10^{19} atoms cm^{-2} (top), $5\times$ 10^{19} atoms cm^{-2}, 10^{20} atoms cm^{-2} and $5\times$ 10^{20} atoms cm^{-2}

Chapter 2

Instrumentation and Data Analysis

Overview

Throughout this thesis, the data used were acquired by the ROSAT satellite and in the first part of this chapter the instrument and its various detectors are described in detail. I also discuss the instruments on XMM and CUBIC whose launches in the near future should yield data that will have a significant impact on the astrophysical topics studied in this thesis. In the second part of the chapter the data analysis techniques used to analyse the ROSAT data are discussed.

2.1 ROSAT

The Röntgen satellite (ROSAT; Trümper 1984) is a three-axis stabilised vehicle which contains two co-aligned instruments; the Wide Field Camera (WFC; Sims *et al.* 1990) and the X-ray Telescope (XRT; Aschenbach 1988) (see Figure 2.1). It was launched into a circular orbit on June 1st 1990 with the primary aim of producing the first ever all-sky X-ray survey using an imaging telescope. This was successfully completed on January 25th 1991. Thereafter, ROSAT has operated in a pointing mode so that prolonged observations of individual targets can be made. An attitude control system maintains the pointing accuracy to within 1′.

On the 12th of February 1999, ROSAT was finally shut down as two of its detectors (the High Resolution Imager and the Wide Field Camera) had failed, while the supply of gas used in the proportional counter had also run out. The highlights of the mission have included the detection of X-ray emission from comets (such as Hyakutake) and the observation of the supernova 1987A.

2.1.1 The XRT

The X-ray Telescope consists of an X-ray mirror assembly and two types of detector; a position sensitive proportional counter (PSPC) built by MPE (the Max-Plank Institut für Extraterrestriche Physik) and a high resolution imager (HRI) built by NASA. The two detectors, (along with a spare PSPC) are mounted on a carousel so that any one of them can be placed at the focus of the "optics".

The mirror assembly consists of four concentric grazing mirrors in a Wolter Type I configuration. Each mirror is composed of a glass ceramic and is coated with a thin layer of gold to enhance its X-ray reflectivity. In total, the mirrors provide a geometric area of 1141 cm^2 although the actual effective area drops off with energy due to a combination of vignetting, variation in gold reflectivity and small angle scattering from the mirror surface. A focal length of 240 cm provides a circular field of view with ~one degree radius for each detector.

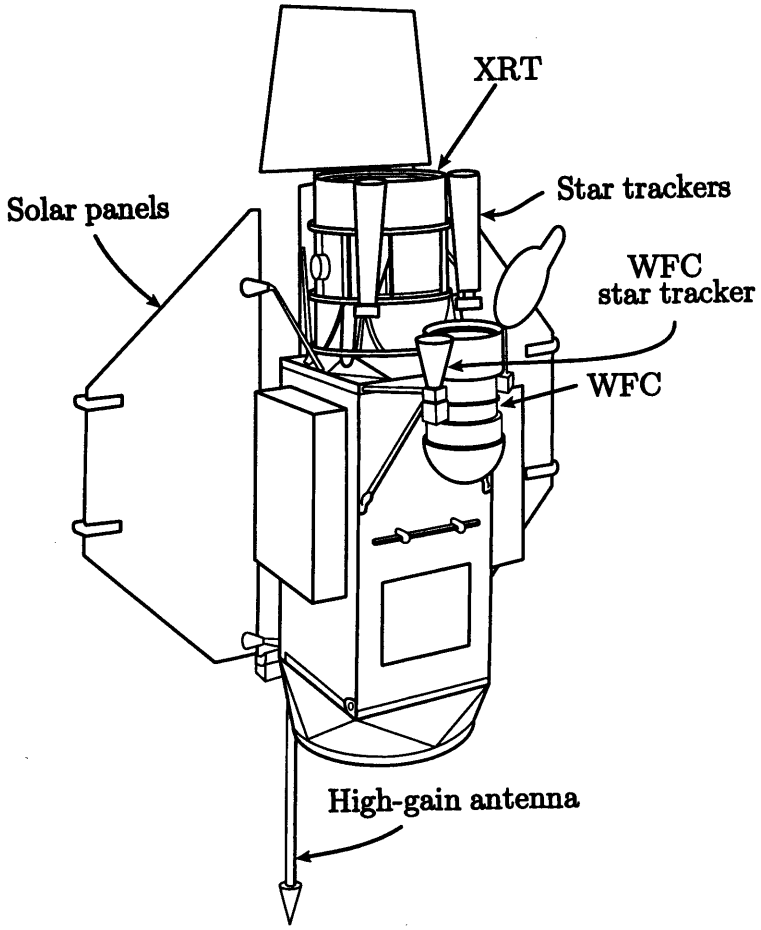

Figure 2.1: A sketch of the various detectors on the ROSAT payload.

The resolution of the mirrors is dependent on both the scattering due to the micro-roughness of the mirror surface and the off-axis blur. These effects result in an energy dependent point spread function which increases from $5''$ on axis to $> 10'$ at the edge of the field of view.

The PSPC is a typical imaging proportional counter. It comprises two anodes and two cathodes (K1 and K2) which each consist of a wire grid supported by a ceramic frame. The first anode (A1) and the two cathodes provide a position sensitive count-rate, while the second anode (A2) provides an anti-coincidence count rate (master veto rate) which is used for background rejection. The gas in the counter is a mixture of 65% Argon, 20% Xenon and 15% of the quench gas methane. Its 1 atm. pressure is contained by a thin plastic entrance window which has a ribbed support structure. The structure consists of an inner circular ring of radius $\sim 20'$ which is supported by 8 struts, and two sets of wires.

One set of wires are thick ($\sim 12''$) and have a $3'$ separation and one set are thin ($\sim 3''$) and have a $\sim 36''$ separation. To avoid the obscuration of sources by this structure, the pointing direction is "wobbled" with a period of 400 seconds and amplitude of $3'$. The window itself is made from a 1μm propylene foil and is coated with 50 μg cm^{-2} of graphite to conduct away any charge on the window which would otherwise build up and affect the electron drift velocity. A further coat of Lexan is also applied to the window to decrease the transmission of UV photons.

X-ray photons interact with the gas in a proportional counter through the photo-electric effect. Many electrons are produced through collisions between the gas atoms and the photoelectron and a charge cloud is formed. The electrons in this cloud are attracted towards the positive potential of the anode, and they accelerate towards it, ionising more and more atoms. Finally, this accumulated charge reaches the anode, resulting in a current flow which is proportional in magnitude to the energy of the original photon. Electronic circuits are used to shape this pulse and digitise it into one of 256 channels. The position of this interaction within the plane of the detector is determined from the charge produced by positive ions which are attracted to the crossed K1 and K2 cathodes (see Fraser (1989), Briel *et al.* (1994) and Adams (1980)).

The quantum efficiency of the PSPC drops off at low energies due to photon absorption within the window material and also at high energies due to the lack of an interaction within the detector volume.

The energy dependence of the quantum efficiency is shown in Figure 2.2. The X-ray absorption in the gas is actually close to 100% at energies between 0.1-2.0 keV so the total QE of the device is determined by the window transmission (including the effects of the support structure). The energy resolution of the device has the form:

$$\frac{\Delta E}{E} = 0.43 \times (\frac{E}{0.93})^{-0.5}$$

where E is the energy in keV.

Because of their nature, these devices are also sensitive to charged particles and gamma rays, so steps have to be taken to veto these events. This is achieved using the anti-

coincidence counter. This comprises an additional anode placed around the five walls of the counter. Any event which triggers this in addition to the main counter is ignored.

For calibration and monitoring of the particle background, a filter wheel is mounted at the front of the PSPC. It has four separate positions. The first holds an Al Kα source for spectral calibration, the second holds a Boron filter to increase spectral resolution at low energies, the third holds an aluminium shield which completely blocks the X-ray count so that the particle background can be monitored and the fourth is fully open for normal observation mode.

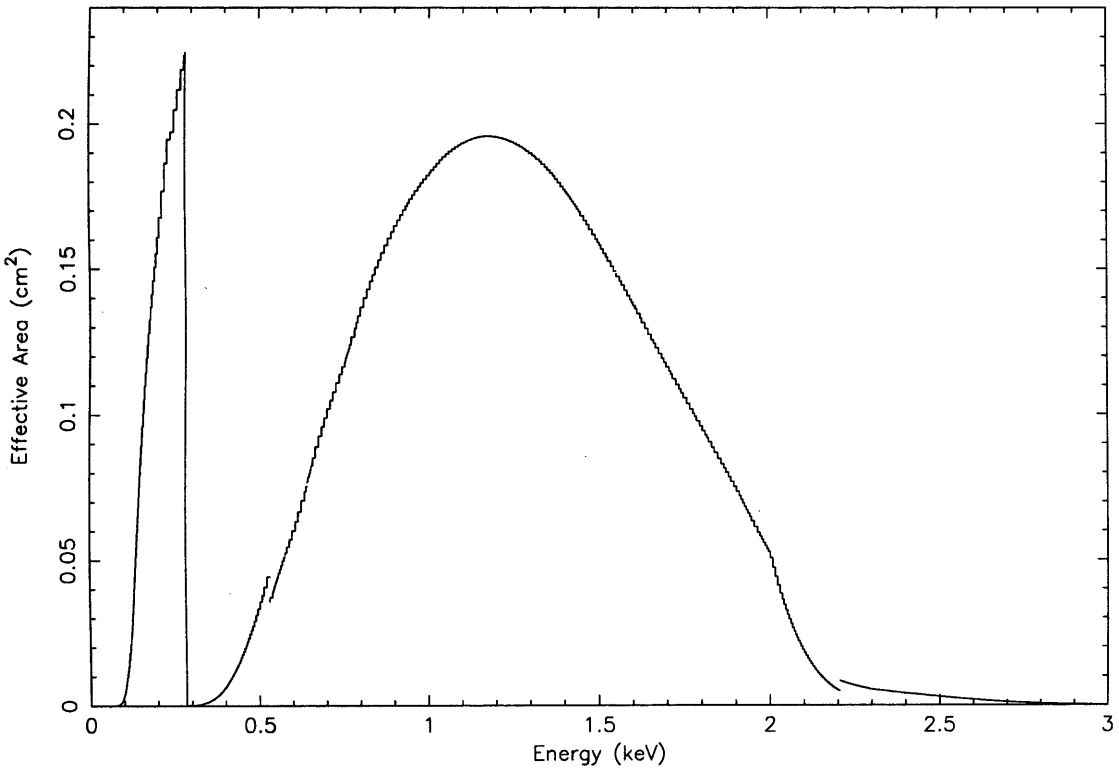

Figure 2.2: The effective area (normalised) of the ROSAT PSPC as a function of energy.

2.1.2 The Wide Field Camera

The ROSAT Wide Field Camera (WFC) was built by five British research groups; Leicester University, Birmingham University, Mullard Space Science Laboratory (of University College London), Imperial College of Science, Technology and Medicine and the Rutherford Appleton Laboratory. It was combined with the X-ray telescope to extend ROSAT's spectral coverage to EUV energies. It operates as a relatively independent instrument

providing its own star tracker, thermal control, and command and handling system. The camera itself consists of 3 grazing incidence mirrors, 8 filters and 2 micro-channel plate detectors (MCP's). The three concentric mirror shells, built in a Wolter-Schwarzschild type I configuration, provide a geometric area of 475 cm^2 and a focal length of 525 mm. The grazing incidence focal length translates to a circular field of view of 2.5 degree radius for each of the detectors. The MCP's are optimised (curved) to take full advantage of the focal surface and are also coated with a thin layer of CsI to enhance their XUV quantum efficiency. Since micro-channel plates have effectively no energy resolution, the ROSAT WFC makes use of 8 filters to obtain some colour information. Each filter is installed on a turntable such that any one of them can be selected by space-craft command. Two of these, the S2 and S1 filters, were used throughout the ROSAT survey phase. A combination of Carbon, Lexan and Boron in the S1 filter provide good transmission for energies of 90-210 eV while the Beryllium and Lexan used for the S2 filter have a peak response between 60-110 eV (see Figure 2.3).

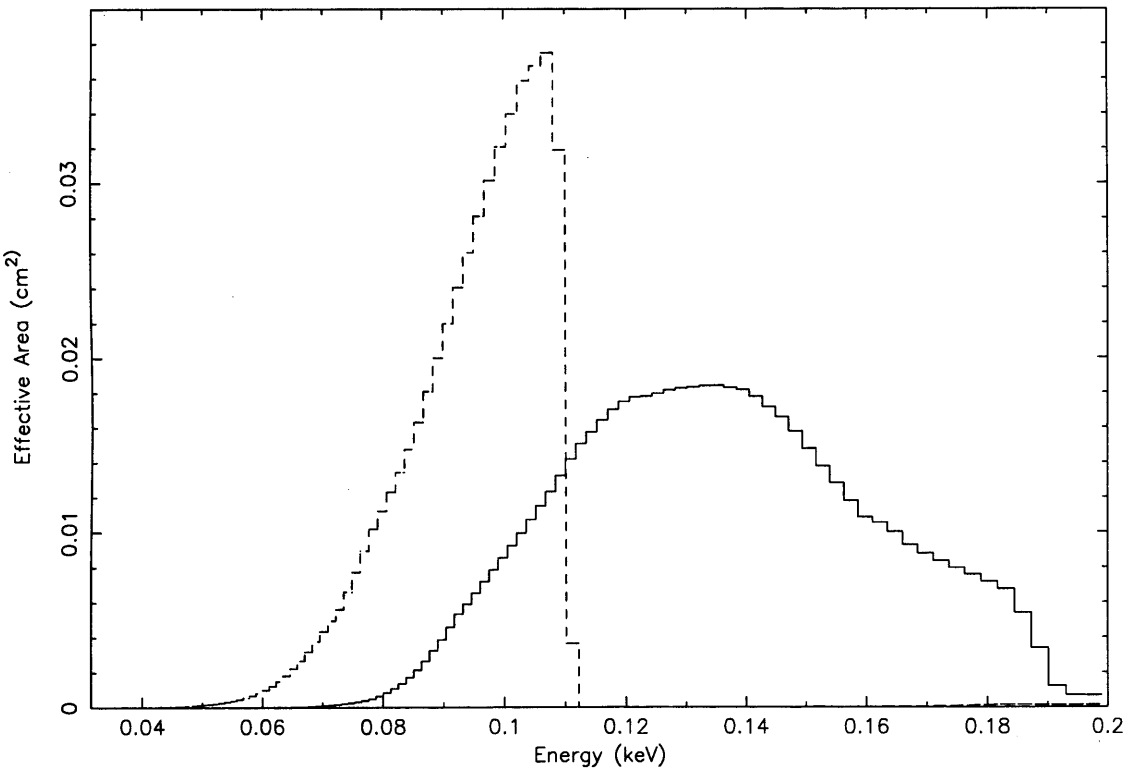

Figure 2.3: The effective areas (normalised) of the S2 (left) and S1 (right) filters on the ROSAT WFC.

2.2 CUBIC

The Cosmic Unresolved X-ray Background Instrument using CCD's (CUBIC) was designed and built by the Penn State University X-ray astronomy group (Burrows *et al.* 1995a). It was launched as part of the NASA/CONAE satellite SAC-B (Satelite de Aplicaciones Cientificas) on a Pegasus V5 launch vehicle on October 10th 1996. Unfortunately, although the launch was succesful, the final stage did not separate from SAC-B once in orbit and consequently overshadowed the solar panels. This led to a reduction in power and ultimately to a loss of control over the satellite and its instruments. Proposals for the launch of CUBIC II are currently under consideration.

The experiment was designed to study the spectrum of the diffuse X-ray background with unprecedented sensitivity and spectral resolution between 0.2 and 10.0 keV. It consisted of a pair of Charge Coupled Device (CCD) detectors and a coarse "pinhole" collimator (see Figure 2.4). The geometry was such that each CCD viewed a solid angle of ~90 square degrees and offered a "cross eyed" view of the sky. This not only increased the total instrument field-of-view to 176 square degrees but also allowed simultaneous on source and off source measurements, essential for the detailed analysis of extended objects such as supernova remnants where detailed background measurements are required.

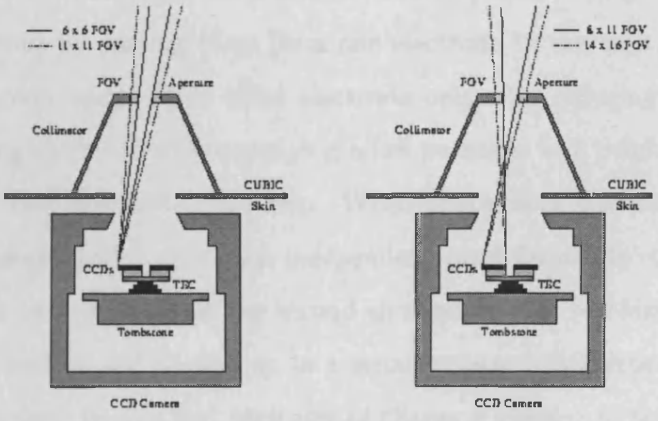

Figure 2.4: The CUBIC instrument. The outer aperture is formed from Be foil which transmits above 2 keV (Burrows *et al.* 1995b).

The CCD's were built by EEV Ltd of Chelmsford, UK, specifically for soft X-ray imaging spectroscopy. They are three-phase front-side illuminated devices incorporating a thinned

gate structure which offers improved soft X-ray quantum efficiency over the more typical CCD design. The use of high resistivity epitaxial material provides good sensitivity up to energies of 10 keV. The CCD's provide an energy resolution as low as 30 eV over the 0.1-10 keV range (Burrows *et al.* 1995b). The optimum spectral response (Fano limited) is degraded by the read-noise of the CCD which is typically 4 electrons rms.

The quantum efficiency of CUBIC is limited at soft energies by the electrode structure of the CCD's and an aluminium/titanium filter used to shield out UV photons (see Chapter 7 for a more detailed discussion of the CUBIC QE).

2.2.1 X-ray CCD's

A charge coupled device consists of an array of elements which are capable of storing and transferring charge. Each element is composed of a metal oxide/semiconductor junction in an MOS CCD. By applying a positive potential to the polysilicon electrode a depletion region is formed in the underlying silicon and a potential well is created where charge can be stored. In practice, a two dimensional array of elements is formed by applying a series of parallel electrodes to the surface of the silicon orthogonally to a set of implants beneath the surface. The implants, called channel stops, electrically isolate one row of elements from another, while the electrodes form the columns. Charge packets can be transferred across the device for readout by passing them from one electrode to the next. This is achieved by collecting electrons under every third electrode only. By reducing the potential on the charge collecting electrode whilst applying a full potential to a neighbouring electrode the electrons pass from one well to the next. When operated in this manner the CCD is known as a three phase device with each independent pixel formed by three electrodes in one dimension and two implants in the second dimension. On reaching the edge of the device, the charge packets are clocked on to a serial register which repeats the process in an orthogonal direction. In this way each row of charge is clocked to the output node for measurement. The output node is a capacitor, onto which the charge forms a voltage. This voltage is amplified by a field effect transistor which is built into the CCD. A second transistor is used to reset the voltage on the output node after each charge packet has been read out. On leaving the device the signal is passed through a correlated double

sampler circuit to remove as much noise (associated with variations in the reset level) as possible. Finally, an analogue to digital converter is used to convert the signal amplitude to a digital value which is then stored in computer memory.

In a CCD, the charge clouds are created by the photo-electric absorption of a photon in the silicon. The magnitude of the charge cloud is proportional to the energy of the photon. If charge is collected over a very short exposure, then no more than one photon is collected in each pixel and the magnitude of the charge is directly proportional to the energy of the photon so that an energy spectrum can be acquired. If however, the exposure time is long, then more than one photon may be collected in each pixel and only an image of the X-ray source can be obtained. Consequently, for high count-rates, the CCD is often operated in frame store mode where charge is shifted to a shielded region of the CCD while it is clocked out. This prevents charge collection during the readout cycle which would otherwise smear the image. To optimise the sensitivity of a CCD to X-rays, the electrode structure needs to be as thin as possible to reduce the number of photons absorbed before reaching the silicon, while the resistivity needs to be as large as possible to increase the depth of depletion for sensitivity to high energy photons.

2.3 XMM

The ESA high throughput X-ray Multi-Mirror satellite (XMM; Mason *et al.* 1995b) is due for launch in 1999. A sketch of the XMM payload is given in Figure 2.5. The aims of the mission are to provide good enough sensitivity to perform medium-resolution X-ray spectroscopy of faint sources ($\sim 10^{-15}$ erg s^{-1} cm^{-2}). This is to be achieved using 3 mirror modules, each containing 58 shells built in a Wolter-I configuration. In combination, the mirrors provide an effective area of 10000 cm^2 at 2 keV and 5000 cm^2 at 7 keV which will provide sensitivity to a limiting flux of 1×10^{-15} ergs s^{-1} cm^{-2} in the 0.1-2 keV band. The spatial resolution varies from $<20''$ at 3 keV to $<30''$ at 8 keV.

There are three types of instrument on XMM; the European Photon Imaging Camera (EPIC; Villa *et al.* 1996) which consists of three CCD cameras (each one at the prime focus of a mirror module), two Reflection Grating Spectrometers (RGS; Brinkmann *et al.* 1996)

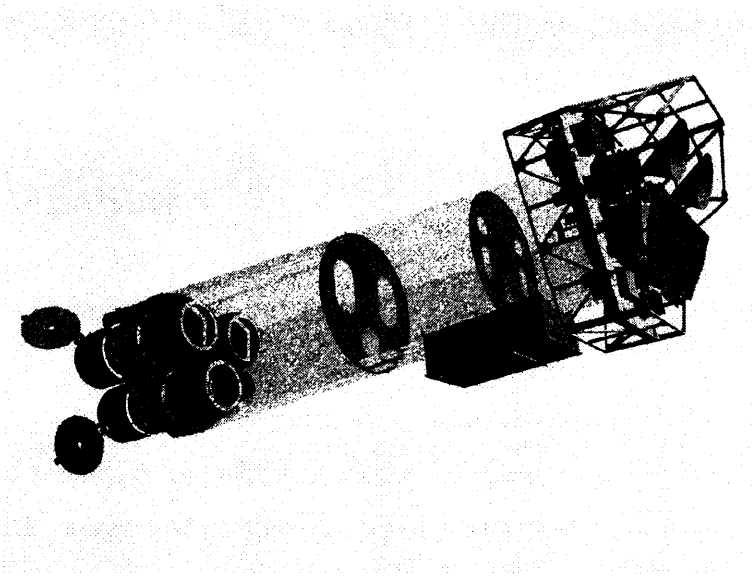

Figure 2.5: A sketch of the XMM payload taken from the XMM Users' Handbook Issue 1.0 (courtesy of Dornier Satellitensysteme GmbH). The three mirror modules can be seen to the left of the diagram and the focal plane instruments to the right.

and a co-aligned Optical Monitor (OM; Mason *et al.* 1996) which will provide simultaneous optical coverage of each X-ray field.

EPIC incorporates two types of CCD; two cameras based on MOS technology (Holland *et al.* 1996) and one based on pn technology (Meidinger *et al.* 1996). Both cameras have a field-of-view of $\sim 30'$ diameter, are sensitive to X-rays in the 0.1-10 keV band and can provide medium resolution spectroscopy ($\Delta E/\mathrm{E} \sim 10$ at 0.5 keV). The MOS devices include a frame transfer mode so that they don't suffer from charge smearing, while the pn devices have superior efficiency at high energies and are less sensitive to pile-up. The pn camera receives the full beam from one mirror module while the two MOS cameras receive approximately half the beam from each of the other two mirror modules. The two MOS cameras can be identified through their distinctive radiator "horns" in Figure 2.5. The two RGS are situated between the mirror modules and the MOS detectors and receive approximately half of the beam from a mirror module.

The OM is a Ritchey-Chretien telescope (30 cm aperture) with a microchannel-plate intensified CCD at its focus. The instrument is capable of performing photometry and imaging in the wavelength range: 1700-5500 $\AA$. Its limiting magnitude is ~ 24.5 for a 1000 second, un-filtered exposure of a B0 star. A grism is also available for low resolution spectroscopy.

The RGS use CCD's for readout and are capable of performing moderately high resolution spectroscopy ($E/\Delta E \sim$ 100-1000) in the 0.3-2.5 keV energy band.

2.4 Data Analysis

2.4.1 Spectral Modelling

The response of an X-ray detector (such as a proportional counter or a CCD) depends on both spectral resolution and efficiency. These components can be complicated and can vary rapidly with energy and so they are usually described by a response matrix. The matrix consists of two separate elements; an effective area component which describes the QE, mirror area and filter response and a redistribution component that describes the mapping of a mono-energetic X-ray beam to the output PHA channels. Theoretically, the application of the inverse response matrix to the background subtracted data should yield the source spectrum. However, such matrices are ill determined and often have no unique solution. Consequently, a fitting method is usually adopted in which a trial spectrum is convolved with the response matrix and a minimum χ^2 fit is performed on the data by altering the parameters of the trial model (Bevington & Robinson 1992). The goodness of the fit is expressed in terms of the χ^2 statistic and the errors on each parameter are quoted for a $\Delta\chi^2$ of 2.7, equal to 90% confidence for one degree of freedom.

2.4.2 PSPC Data

As discussed in Section 2.1.1, the PSPC data is digitised into 1 of 256 channels. However, due to variations in spatial and electronic gain the pulse heights determined for a given photon would vary depending on the position of its interaction in the detector. Consequently, these pulse heights are corrected by the the ROSAT Standard Analysis Software System into pulse height invariant (PI) channels. The relationship between PI channel range and energy band is given in Table 2.1.

Given the resolution of the PSPC, source spectra can be interpreted using only a modest number of relatively independent energy bands (Snowden *et al.* 1994b, Briel *et al.* 1994).

Table 2.1: The relationship between PI channels and energy band.

PI_{low}	PI_{high}	E_{low}	E_{high}	PI_{low}	PI_{high}	E_{low}	E_{high}
7	8	0.07	0.09	84	90	0.84	0.91
9	10	0.09	0.11	91	98	0.91	0.99
11	13	0.11	0.14	99	106	0.99	1.07
14	16	0.14	0.17	107	114	1.07	1.15
17	19	0.17	0.20	115	122	1.15	1.23
20	23	0.20	0.24	123	131	1.23	1.32
24	27	0.24	0.28	132	140	1.32	1.41
28	31	0.28	0.32	141	149	1.41	1.50
32	36	0.32	0.37	150	159	1.50	1.60
37	41	0.37	0.42	160	169	1.60	1.70
42	46	0.42	0.47	170	179	1.70	1.80
47	51	0.47	0.52	180	190	1.80	1.91
52	57	0.52	0.58	191	201	1.91	2.02
58	63	0.58	0.64	202	212	2.02	2.13
64	69	0.64	0.70	213	223	2.13	2.24
70	76	0.70	0.77	224	235	2.24	2.36
77	83	0.77	0.84	236	247	2.36	2.48

The optimum mapping of the PI channels to seven such bands is described by Snowden *et al.* (1994b) and used for all the data presented in this thesis (see Table 2.2).

Table 2.2: PSPC Channel bands according to Snowden *et al.* (1994b).

Band	PI Channel	10% Peak Energy Range keV
R1	8-19	0.11-0.28
R1L	11-19	0.11-0.28
R2	20-41	0.14-0.28
R3	42-51	0.20-0.83
R4	52-69	0.44-1.01
R5	70-90	0.56-1.21
R6	91-131	0.73-1.56
R7	132-201	1.05-2.04

For the analysis of diffuse objects it is important to correct for spatial variations in the quantum efficiency of the detector and vignetting effects associated with the XRT. In the standard analysis software, this is achieved using exposure maps, such that a flat fielded image can be obtained by dividing the count map by the exposure map. These maps were obtained from the all-sky survey data (with point sources and background contamination

removed) and provide the response of the telescope and detector to a flat field.

For a particular observation, the variations in roll angle, RA and Dec must be accounted for and a time averaged exposure map produced. Since the vignetting and QE of the detector vary as a function of energy, a different map must be produced for each of the energy bands given in Table 2.2. During its lifetime, both of the PSPC's on ROSAT have been used. The first (PSPCB) failed on the 25th of January 1991 and the second, (PSPCC) has been used thereafter. Consequently, different detector maps must be used for data taken before and after this date (since the gains of the two detectors are slightly different). In addition, the gain of the second detector was reduced on the 11th of October 1991. For observations made when the PSPC was operated in this mode, the R1L (see Table 2.2) band (and associated detector maps) should be used to maintain the same energy range as for the R1 band.

Also particularly important to the analysis of diffuse objects such as those considered in Chapters five and six, is the careful removal of all non-cosmic contaminants (Snowden *et al.* 1992; Snowden & Freyberg 1993; Plucinsky *et al.* 1993; Snowden *et al.* 1994b). Once again, the standard analysis software was used to subtract an estimate of these components. The techniques used in the software are described in detail below.

2.4.3 Solar contamination in the PSPC

Solar photons excite the chemical components of the Earth's atmosphere and produce X-rays. Given the correct sun-satellite angle these can impinge on the detector and are indistinguishable from cosmic photons. Consequently, detailed modelling involving the variation of sun-satellite angle and the temporally varying composition of the atmosphere is required to estimate the magnitude of this component (Snowden & Freyberg 1993). At the altitude of the ROSAT orbit (550km) and for the typical PSPC zenith angle, this scattering is dominated by atomic oxygen, nitrogen and helium. There are two mechanisms for the production of X-rays that need to be considered; Thomson scattering from oxygen, helium and molecular nitrogen which dominates the emission at 0.25 keV, and the fluorescence of molecular nitrogen and oxygen which dominates at the corresponding (higher) line energies. Ideally, a full radiative transfer treatment is required that takes into account

the absorption as well as scattering properties of the atmosphere. However, it has been shown that at PSPC energies, the atmosphere can be treated as optically thin if the zenith angle for the observation is kept below 97°. If this constraint is adhered to, it is just the flux scattered from the illuminated column along the observations line of sight that needs to be determined. This can be calculated from; the solar spectrum and its intensity, the atmospheric column densities and the geometry of the observation. Atmospheric column densities may be obtained using the COSPAR International Reference Atmosphere (CIRA 72; Jacchia 1972), which provides 3-dimensional and temporal data relating to the column densities of the six most abundant chemical species. The geometry of the observation can be calculated from the satellite attitude data which is recorded every sixty seconds. However, there is no *a priori* knowledge of the solar soft X-ray spectrum for a given observation, so it has to be determined from the X-ray data itself. This is most easily achieved by sampling some of the high count-rate regions of the data (those most heavily affected by solar scattering), determining a spectrum and comparing it to a spectrum of data from low count-rate periods. Since the solar contamination is a very strong function of increasing zenith angle, there can often be a large count-rate gradient across the detector. This is accounted for by determining the extent of the gradient and distributing counts across the detector accordingly.

2.4.4 Particle Contribution

Particles (significantly) present in the Earth's radiation belts, interact with the gas in the proportional counter in much the same way as X-rays. Consequently, their contribution to the total X-ray count has to be removed. Much of this is achieved on-board, where events are accepted only if; electrodes on each of the five sides of the device have not been triggered, the event energy is not too large and the morphology of the event is acceptable. This method vetoes in excess of 99.5 % of all particle induced events (Plucinsky *et al.* 1993). However, for diffuse source analysis, the remaining particle induced events are important and further modelling is required to account for them. This is achieved using a correlation between particle count-rate and Master Veto Rate (MVR). However, this correlation is only valid for master veto rates below 170 counts sec^{-1} so all data collected during periods when the MVR exceeded this value must be ignored. Three separate particle components

are identified; internal, external and Al Kα, and a contribution is calculated for each one. The distribution across the detector varies for each of these components and maps to model this are provided in the standard software. In particular, it should be noted that the external component is shadowed by the window support structure.

2.4.5 Afterpulses

A further source of contamination primarily associated with the PSPC particle background is the afterpulse component. It has been shown that low level afterpulses can be produced after some events. These generally occur very soon after the initial event so a significant fraction can be identified and removed by ignoring all events which are separated by less than 0.35 ms. However, because the majority of particle events are vetoed on board, the initial event (i.e. that produced by the particle) is very often removed from the data so that its associated afterpulse cannot be easily identified. Instead, an estimate of the remaining afterpulse events has to be made by performing a spectral fit to the low energy data. The spectral form of the afterpulses can be determined by fitting a Polya function to all the events which occurred within 0.35 ms of a precursor event. This model can then be used along with the particle background spectrum and a thermal plasma model to fit the low energy data to determine the amplitude of the afterpulse model. The distribution of this contamination across the detector has been determined and the resulting afterpulse map (provided in the SASS distribution) has been used throughout the analysis presented here. It should be noted that this contamination only became apparent in the Summer of 1991 and does not affect data obtained before that time.

2.4.6 Short Term Enhancements

These are caused by any other mechanism (non-cosmic) which results in the variation of the X-ray level impinging on the detector over intervals less than the orbital period. The primary contributors are auroral X-rays, which reveal themselves as large gradients in the light-curve of an observation. The best way to remove their contribution, is to simply discard all data collected during the contaminated period.

2.4.7 Long Term Enhancements

Even after the removal of the above components, it has become apparent from the all-sky survey data (see Snowden & Schmitt 1990) and previous missions (including both rocket and satellite platforms) that a further background component is present in X-ray data. This is seen to vary over time periods much longer than the orbital period and doesn't appear to correlate with any of the satellite parameters. Consequently, its contribution has to be modelled from the light curve of the observation whilst accounting for each of the above components. The model varies from one observation to another but the best fit over the time scale of a typical observation is often achieved using a polynomial of fourth order or less.

Chapter 3

X-ray/EUV Spectral Analysis of Late Type Stars

Overview

This chapter describes an investigation of the ROSAT X-ray/EUV spectra of late-type stars. The aim is to use the absorption characteristics in their spectra to determine the HI column density along the line-of-sight to each source. Only sources with HIPPARCOS parallaxes are selected so that the measurements can be used (in the following chapter) to map out the distribution of cool absorbing gas in the local (<400 pc) interstellar medium.

3.1 Introduction

During the last 20 years a detailed picture of the interstellar medium surrounding the Sun has begun to emerge (see for example Fruscione *et al.* 1994 which details many of the measurements made so far). Lyman α absorption features observed in the optical/UV spectra of stars have revealed the cool gas distribution over scale sizes of several hundred parsecs (see Bohlin, Savage & Drake (1978) for details of the technique and Frisch & York (1983) for interpretations of such observations), while EUV spectra collected during surveys performed by the ROSAT WFC (Pounds *et al.* 1993; Pye *et al.* 1995) and EUVE (Bowyer *et al.* 1994; Bowyer *et al.* 1996) have provided information on material within 100 pc of the Sun (eg. Warwick *et al.* 1993; Diamond, Jewell & Ponman 1995). Indirect measurements of N_H provided by observations of NaID lines in conjunction with an empirical relationship between NaI and HI column densities (Ferlet, Vidal-Madjar & Gry 1985), have also provided a large amount of data which have been used to map out the very local ISM (see Welsh, Vedder & Vallerga 1990; Welsh *et al.* 1994; Paresce 1984). A significant problem with all of these studies however, has been the lack of sky coverage caused by the relatively small number of sources which have both an accurate N_H measurement and an accurate distance measurement.

Recently, the publication of the ROSAT PSPC bright source catalogue (RBSC) has provided a large number of X-ray observations of stellar sources. As indicated in a number of studies (eg. Diamond, Jewell & Ponman 1995), the X-ray spectra of such sources are sensitive to HI column density, and in theory a spectral analysis should be able to quantify N_H along the line-of-sight to each source. Additionally, the recent availability of the HIPPARCOS catalogue has provided accurate parallaxes for a large number of stellar sources, so that in combination with N_H information, it should be possible to map out the three-dimensional distribution of cool absorbing gas in the local ISM with greater accuracy than previously possible.

The aim of this chapter is to compile as large a sample of stars as possible which have an accurate HIPPARCOS parallax and HI column density so that they can be used in the following chapter to investigate the distribution of cool absorbing gas within the local ISM.

3.2 The Data

The data used for this study were obtained from LEDAS (the Leicester Database and Archive System). They incorporate a combination of observations made by the ROSAT PSPC and Wide Field Camera during the ROSAT all-sky survey as well as measurements from the HIPPARCOS mission. The information available and its format is discussed below.

3.2.1 ROSAT WFC

During 1990 the ROSAT Wide Field Camera performed an all-sky EUV survey in the two colours defined by its S1(60-140 Å) and S2(112-200 Å) filters. From an initial analysis of source detections the bright source catalogue (RBSC) was produced containing 383 objects. In 1995 this was superseded by the 2RE catalogue (Pye *et al.* 1995), which as a result of improved data rejection, background screening and superior source detection techniques, listed a total of 479 sources. All of these sources have a detection significance in one band of at least three. Of these, 387 have a significance > 3.0 in both bands which results in a combined significance of > 5.5. The S2 and S1 count-rates along with errors and the significance of each detection are listed in the catalogue. In some cases, only a count-rate upper limit is quoted (90% confidence) and these sources are identified in the catalogue by a count-rate error of zero.

A comprehensive search of astronomical catalogues in conjunction with an optical follow-up program (Mason *et al.* 1995a) identified 256 of the sources as late-type stars, 125 as white dwarfs and 17 as cataclysmic variables. The 2RE catalogue also lists spectral type and absolute magnitude for those sources which could be found in catalogues, such as the MK (Buscombe 1992).

3.2.2 ROSAT PSPC

While the WFC performed its EUV survey, the PSPC recorded an all-sky survey at X-ray wavelengths. Approximately 18000 relatively bright sources detected during the survey are

listed in the ROSAT all-sky survey bright source catalogue (RBSC). Every entry includes two hardness ratios and a broad-band count-rate along with associated errors(1 σ). For this analysis we have converted these to three X-ray count-rates: P1, P2 and P3, where P1 is the count-rate in SASS channels 11-46 (0.1-0.4 keV), P2 is the rate for channels 47-90 (0.5-0.9 keV) and P3 is the rate for channels 91-201 (1.0-2.0 keV). The errors associated with these count-rates were determined by scaling to those quoted for the broad band count-rate.

3.2.3 HIPPARCOS Data

Accurate source distances are determined from parallaxes measured by the HIPPARCOS satellite. These are supplied along with spectral information for over 90000 nearby stars in the HIPPARCOS catalogue. The HIPPARCOS input catalogue (HIC) was used to define the observations made by the satellite and was used throughout this work for correlations with the other catalogues.

3.3 The Samples

This study makes use of two separate stellar samples and the content and nature of these data sets are discussed in detail below.

3.3.1 Sample 1

The first sample consists of all the late-type stars in the 2RE catalogue whose positions fall within 1′ of detections in the RBSC and which also have counterparts in the HIPPARCOS input catalogue (HIC). There are 378 objects common to the 2RE and RBSC listings, with 240 classified as stars in the 2RE catalogue. Of those, 225 are late-type stars (40 F, 74 G, 64 K and 47 M) and 5 are unclassified. We have included the unclassified stars in the sample since 95% of the stars detected by the ROSAT WFC are late-type. A cross correlation of the late-type stars with the HIPPARCOS catalogue defines our final sample of 178 sources. For cases where the HIPPARCOS source appeared to be different to the

2RE identification (i.e. significantly different spectral types, luminosity class or apparent magnitude) the HIPPARCOS identification was assumed.

3.3.2 Sample 2

Sample 2 consists of the 2728 late-type stars in the RBSC catalogue which have counterparts in the HIPPARCOS input catalogue. According to the spectral types quoted in the HIPPARCOS input catalogue, there are 1045 F-stars, 947 G-stars, 533 K-stars and 134 M-stars (3 dM stars). The remainder were unclassified stars, but since over 90 percent of stars detected with a significant X-ray flux are expected to be late-type, we have included them in this analysis. It should be noted that the sources in this sample include those in Sample 1.

3.4 Sample Properties

The sky distributions of the two samples are shown in Figure 3.1. To discuss the distribution of these sources, both here and in the following chapter, we split the sky into four Galactic quadrants. Each quadrant is equally spaced in Galactic longitude and spans all Galactic latitudes;

Quadrant I	$0^o \leq l^{II} < 90^o$
Quadrant II	$90^o \leq l^{II} < 180^o$
Quadrant III	$180^o \leq l^{II} < 270^o$
Quadrant IV	$270^o \leq l^{II} \leq 360^o$

Sample 1 reveals a slight source density enhancement in the north of Galactic quadrant II and the south of Galactic quadrant III and a deficit of sources towards the Galactic centre. The coverage across the remainder of the sky is relatively uniform. Sample 2 provides an almost uniform coverage across the entire sky.

The distance distribution of the sources in Sample 1 (see Figure 3.2) ranges from 4 to $\sim$100 pc with the peak of the frequency distribution at about 20 pc, while the late-type stars in Sample 2 have a much broader coverage with a distribution which spans 3 to 300 pc and peaks at about 50 pc.

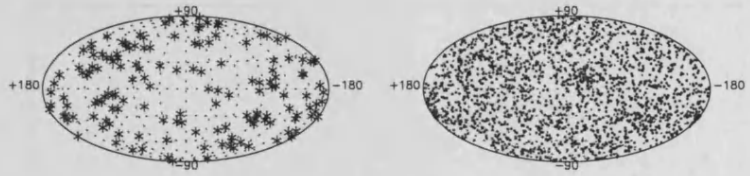

Figure 3.1: An Aitoff projection of the sky distribution of sources in Galactic coordinates for; (a) the late type stars in Sample 1 and (b) the late type stars in Sample 2.

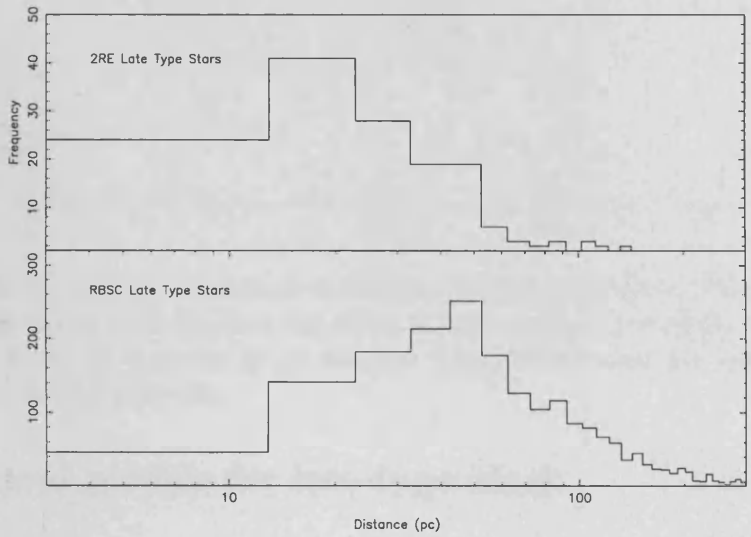

Figure 3.2: The distance distributions of the two samples which indicate the different regions of the ISM that they sample.

The unit optical depth of the S2 energy band corresponds to an N_H of about 1×10^{19} cm^{-2} and the unit optical depth of the S1 band corresponds to an N_H of about 3×10^{19} cm^{-2}. Consequently, there should be a significant up turn in the S1:S2 ratio with distance as an increasing HI column density is sampled. However, a plot of the $\frac{S1}{S2}$ ratio versus distance for the sources in Sample 1 (Figure 3.3) does not demonstrate a very strong correlation, indicating that either there is a considerable spread in average HI density across the sky, or that the intrinsic emission from the stars themselves has a dominant effect on the observed $\frac{S1}{S2}$ ratio. The work in this thesis considers both of these possibilities. In this chapter we consider the form that such intrinsic emission may take within the energy bands considered here. Then in the following chapter, we use the constraints on the predicted $\frac{S1}{S2}$ ratios to determine to what extent the variations are due to the distribution of absorbing material in the local ISM.

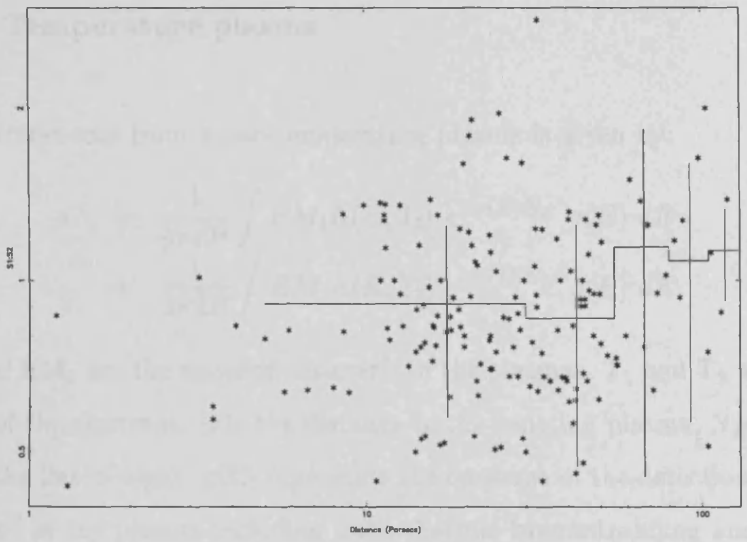

Figure 3.3: The $\frac{S1}{S2}$ ratio as a function of distance for late-type stars. The ratios are generally seen to increase with distance but there is not a strong correlation. The histogram represents the mean $\frac{S1}{S2}$ ratio for 30 pc distance bins and the error bar represents the 1σ spread of ratios within each bin.

3.5 Spectral models for late-type stars

The X-ray spectrum of a late-type star is thought to originate from hot, dense coronal gas (see Vaiana *et al.* 1981; Pallavicini 1989). Consequently, early spectral models consisted of the absorbed emission from a single temperature plasma (in both thermal and ionisation equilibrium). Refinements during the EINSTEIN/ROSAT era resulted in two temperature models although these had no theoretical basis (see, for example, Schmitt *et al.* 1990). In attempts to create more "physical solutions" continuous emission measure models have been formulated in which the emission from a continuum of temperatures is summed according to a power law weighting scheme (see Preibisch 1997). However, spectral fitting results obtained using such models prove to be no better than for those obtained with a two temperature fit. Recently attempts have been made to model the emission from individual coronal loops (eg. Ciaravella *et al.* 1996; Maggio & Peres 1996) in which a distribution of temperatures is derived from hydrostatic equilibrium equations. However, these models are not yet refined and for an individual source a large number of data points are required to model parameters such as loop height and surface coverage. Consequently, only the power law and two temperature models are considered in this study.

3.5.1 Two Temperature plasma

The observed count-rate from a two temperature plasma is given by:

$$\begin{aligned} C &= \frac{1}{4\pi D^2} \int EM_1 \Lambda(E,T_1)\ e^{-\sigma(E)N_H}\ g(E)\ dE \\ &+ \frac{1}{4\pi D^2} \int EM_2 \Lambda(E,T_2)\ e^{-\sigma(E)N_H}\ g(E)\ dE. \end{aligned} \tag{3.1}$$

where EM_1 and EM_2 are the emission measures of the plasmas, T_1 and T_2 are the thermal temperatures of the electrons, D is the distance to the emitting plasma, N_H is the column density along the line-of-sight, g(E) represents the response of the detection system and Λ is the emissivity of the plasma including both thermal bremsstrahlung and line emission (primarily Si, S, O and Fe). Consequently, such a model requires five spectral parameters; N_1, T_1, N_2, T_2 and N_H (where $N_{1,2}$ are normalisations which include the emission measures and plasma distance).

3.5.2 Power law distribution of temperatures

The count-rate observed from a power law emission model is given by:

$$C = \frac{1}{4\pi D^2} \int \int_{T_{min}}^{T_{max}} EM_{max} \left(\frac{T}{T_{max}}\right)^{\alpha}\ \Lambda(E,T) \frac{dT}{T}\ e^{-\sigma(E)N_H}\ \ dE. \tag{3.2}$$

where, T_{min} and T_{max} are the minimum and maximum of the temperature range, EM_{max} is the differential emission measure at the maximum temperature, and α is the power law index describing the distribution of emission measures between the two temperature limits. Again, five parameters are required; (T_{min}, T_{max}, α, N, N_H).

3.5.3 Plasma emission model

We have used the MEKAL code (see Mewe, Lemen & VandenOord 1986; Mewe, Gronenschild & VandenOord 1985) in the spectral fitting package, XSPEC, throughout this analysis with the assumption that the EUV/X-ray spectra of late-type stars can be adequately modelled by hot equilibrium plasmas with solar element abundance.

3.6 Spectral Analysis

3.6.1 Sample 1

Since the models described above each require five parameters, the five available data-points provide no degrees of freedom for spectral fitting. Consequently, to determine which parameters may be fixed in the spectral fitting, and to see which model best describes this combination of EUV and X-ray data, each model is now considered in terms of its ability to describe the global data set. To remove the normalisation as an interesting parameter, the data are considered in terms of four softness ratios: $\frac{S2}{S1}$, $\frac{S1}{P1}$, $\frac{P2}{P1}$ and $\frac{P3}{P2}$.

Two temperature model

Figure 3.4 shows a two "colour plot", namely the $\frac{S2}{S1}$ ratio plotted versus the $\frac{P1}{S1}$ ratio for every source in Sample 1. The data points with $\frac{S2}{S1}$ ratios plotted as arrows are those sources with only an upper limit quoted for the S2 count-rate. The solid loci represent the ratios obtained from XSPEC for various spectral models. The black locus is for plasma temperatures in the range kT=$10^{-0.8}$ to $10^{-0.2}$ keV and an N_H of $10^{18.0}$ atoms cm^{-2} while the red green and blue loci are for the same temperature range but with N_H values of $10^{18.4}$, $10^{18.8}$ and $10^{19.2}$ atoms cm^{-2} respectively. For a given spectral model, the $\frac{S2}{S1}$ ratio is sensitive to N_H values in the range 10^{18}-$10^{19.6}$ atoms cm^{-2} and the $\frac{P1}{S1}$ ratio is sensitive to values in the range $10^{18.4}$-$10^{20.0}$ atoms cm^{-2} so that the effect of increasing N_H is to move the points towards the top left corner of Figure 3.4.

In Figure 3.4, the possible ratios for a two temperature model lie on the straight line which connects the two temperatures (T_{low} and T_{high}) on a particular N_H locus. The actual position along the line is dependent on the relative normalisations of the two temperature components. The ratios for the models with kT_{low}=$10^{-0.8}$ keV and kT_{high}=$10^{-0.2}$ keV are shown as dashed lines in Figure 3.4. The fact that almost all the sources in Figure 3.4 fall within the polygon defined by the single temperature locus with a column density of 10^{18} atoms cm^{-2} and the line which defines the two temperature model with kT_1=$10^{-0.8}$ keV and kT_2=$10^{-0.2}$ keV indicates that the temperature range used here is adequate for modelling the EUV emission from most late-type stars. For comparison, Figure 3.5

shows the $\frac{P1}{P2}$ and $\frac{P3}{P2}$ ratios and corresponding spectral loci. Clearly, most sources in this plot fall within the polygon defined by a temperature range of $kT_{Low}=10^{-0.8}$ keV and $kT_{High}=10^{0.2}$ keV indicating a harder component in the X-ray spectra. Consequently, it is apparent that the X-ray data and the EUV data are sensitive to different spectral components.

In addition it is evident from Figure 3.4 that no single two-temperature (or one temperature) model can successfully describe the spectral properties of the whole source population. Thus we are unable to freeze any of the parameters in our model to enable a spectral fit to column density. Instead, we have adopted a more conservative approach and considered the upper and lower limits to the N_H of a source given the spectral diversity of the models.

As discussed above, the EUV and X-ray data are sensitive to different spectral components and so they need to be treated separately. As a result we only consider the $\frac{S2}{S1}$ and $\frac{P1}{S1}$ ratios for the sources in Sample 1. In Figure 3.4 it can be seen that a two temperature fit with $kT_{Low}=10^{-0.8}$ keV and $kT_{High}=10^{-0.2}$ keV will result in an upper limit estimate of N_H while a single temperature model (with kT in the range $10^{-0.8}$ to $10^{-0.2}$ keV) will result in a lower limit estimate. Consequently, we have assigned upper and lower limits to the N_H towards each source using the following procedure.

For the lower limit, the N_H of each source was determined by performing a χ^2 fit to a single temperature model with kT in the range $10^{-0.8}$ to $10^{-0.2}$ keV and N_H in the range $10^{18.0}$ to $10^{19.6}$ atoms cm^{-2} (using a grid with temperature steps of $\log_{10}(kT)=0.1$ keV and N_H steps of $\log_{10}(N_H)=0.2$ atoms cm^{-2}). Specifically, the assigned value corresponds to the N_H at which the distance of a particular point (weighted by the error of each ratio) from the single temperature locus is minimised in Figure 3.4.

The N_H upper limit was determined using a two temperature model with $kT_1=10^{-0.8}$ keV and $kT_2=10^{-0.2}$ keV (the dashed lines in Figure 3.4). In this case, the χ^2 fit is performed on the ratio of the plasma emission measures and a choice of N_H values in the range $10^{18.0}$ atoms cm^{-2} to $10^{19.6}$ atoms cm^{-2}.

The few sources which lie outside the set of polygons defined by the above procedure

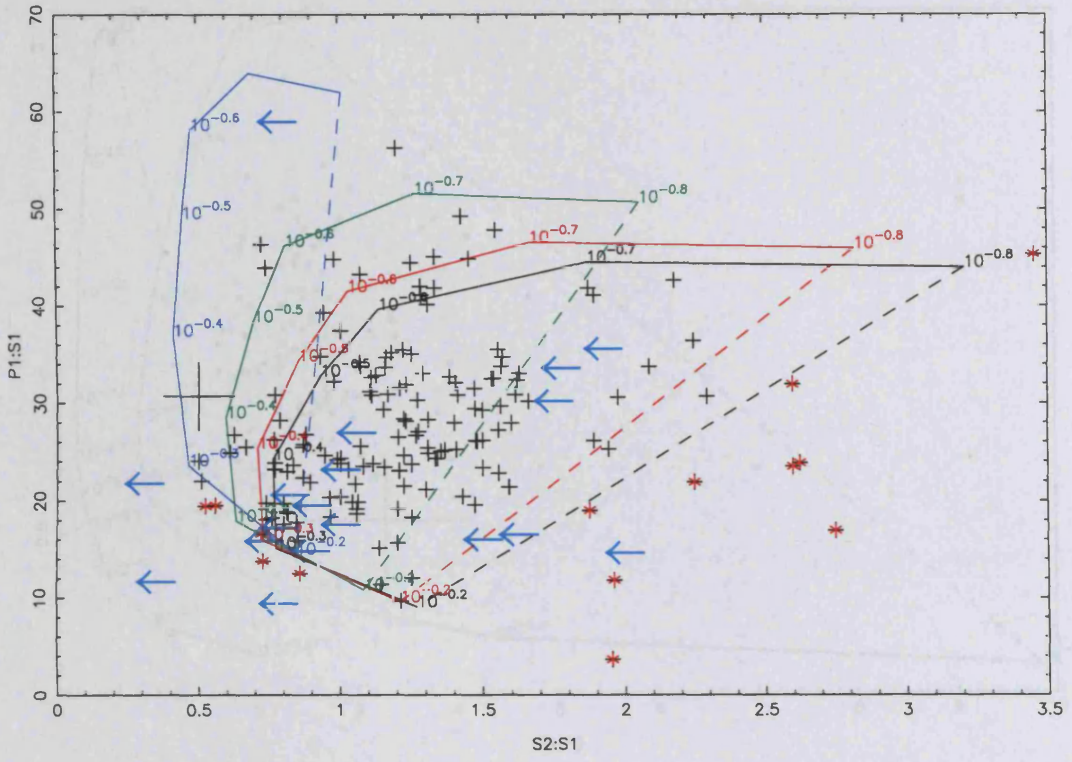

Figure 3.4: Two colour plot for the late-type stars sample 1. The curves (solid) represent the ratios obtained for a single temperature plasma for various column densities. Moving from right to left these column densities are: 10^{18} (black), $10^{18.4}$ (red), $10^{18.8}$ (green)& $10^{19.2}$ cm^{-2} (blue). The dashed lines represent the ratios obtained for a two temperature plasma with T_1=$10^{-0.8}$ and T_2=$10^{+0.2}$ keV. The sources which are plotted as arrows are those which only have an upper limit quoted for the S2 count-rate and the sources labelled with red asterisks are those which fall outside all of the polygons. The ratio errors have been omitted for clarity, although typical error bars are given for the source with $\frac{S1}{S2}$=0.5 and $\frac{P2}{P1}$=30.

represent sources with relatively extreme spectral colours and are excluded from further analysis. Sources which initially have ratios to the right of the single temperature locus and can consequently never be modelled with a sensible column density are assigned the minimum N_H value (10^{18} cm^{-2}) as a lower limit. This minimum value is based on the very local studies of the LISM which have indicated that the Sun resides at the edge of a cloud of warm (10^4K), partially ionised gas (the "local fluff"). It has been shown that this material extends out to distances of $\sim$10 pc and that with a typical density of $\sim$0.1 cm^{-3} (McClintock *et al.* 1976), it contributes a HI column density of $\sim 10^{18}$ atoms cm^{-2} to all observations beyond this distance.

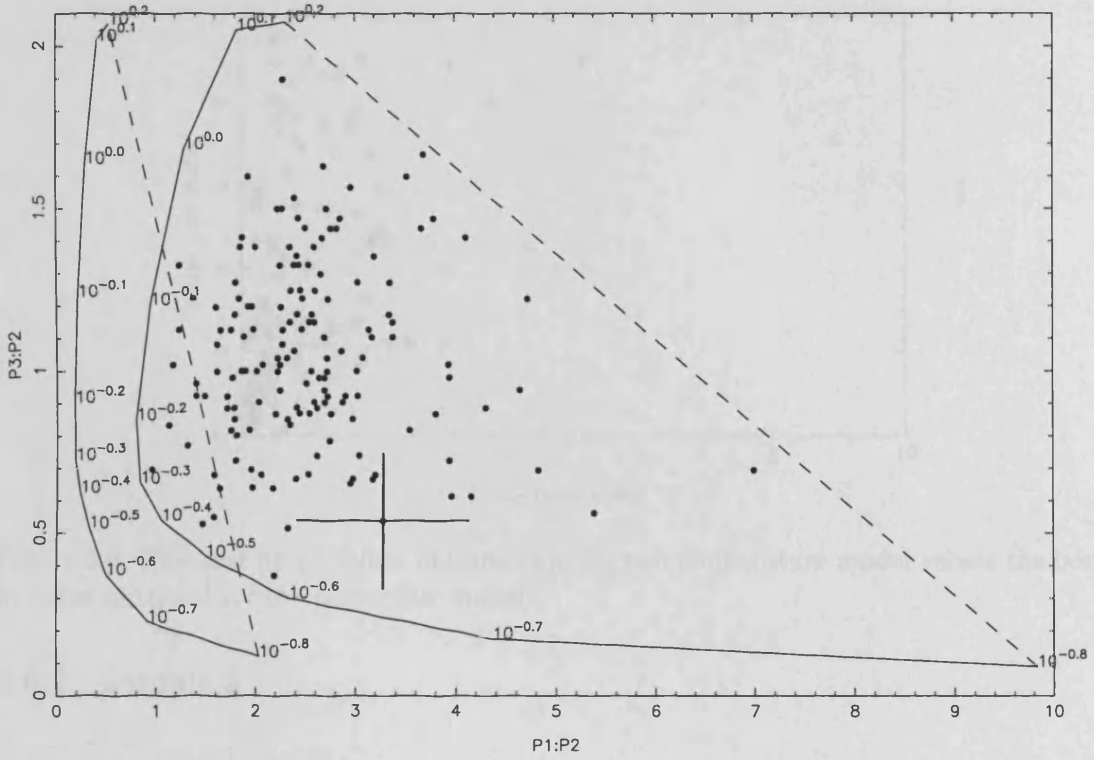

Figure 3.5: The X-ray two colour plot for the late-type stars in Sample 2. The curves (solid) represent the ratios obtained with a single temperature plasma for absorption columns of $10^{19.6}$ cm^{-2} (left) and $10^{21.2}$ cm^{-2} (right), while the dashed lines represent the ratios obtained for a two temperature plasma with T_1=$10^{-0.8}$ and T_2=$10^{+0.2}$ keV. The ratio errors have been omitted for clarity although typical error bars are given for the source with $\frac{P1}{P2}$=3.3 and $\frac{P3}{P2}$=0.5

Power law model

A similar procedure was repeated to investigate the ability of the power law emission model to represent the data. Again, a χ^2 fitting technique applied to the $\frac{S2}{S1}$, $\frac{S1}{P1}$, $\frac{P1}{P2}$, $\frac{P2}{P3}$ ratios was used to obtain the absorption column towards each source which minimised the χ^2 for all the ratios. Figure 3.6 shows the χ^2 values obtained using the two temperature model versus those obtained using the power law model. It is clear that much better values are obtained using the two temperature model and despite the fact that the power law model is slightly more physical, we now concentrate on only the two temperature solution.

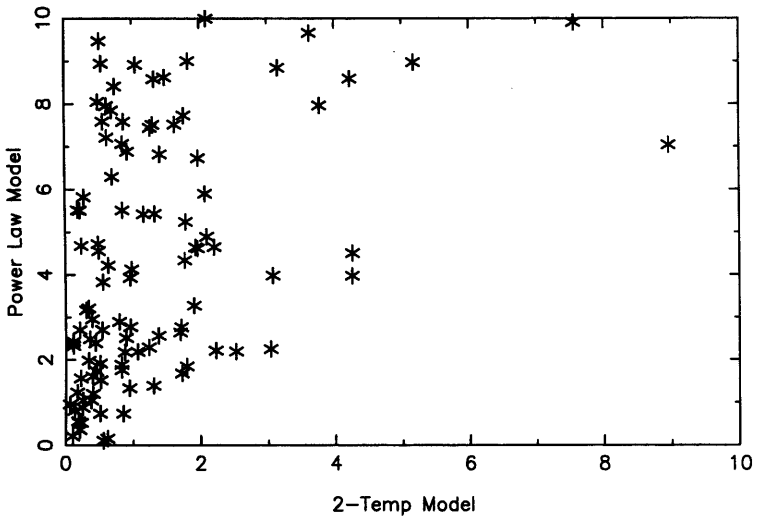

Figure 3.6: The best fit χ^2 values obtained for the two temperature model versus the best fit value obtained for the power law model.

3.6.2 Sample 2

The sources in this sample do not have EUV detections and so they are sensitive to much larger column densities (they are insensitive to N_H values less than 3×10^{19} atoms cm^{-2}) than those in Sample 1. The $\frac{P1}{P2}$ ratio is most sensitive to the absorption column because of its lower energy, and is sensitive to N_H in the range $10^{19.6}$-$10^{21.2}$ cm^{-2}. In this case the dataset is considered in terms of the $\frac{P1}{P2}$ versus $\frac{P3}{P2}$ two-colour diagram (see Figure 3.7). As discussed in the last section, in the X-ray two colour plot, a slightly higher upper temperature of $kT_{high} = 10^{+0.2}$ keV is required for the polygon to encompass the majority of sources. The polygons in Figure 3.7 are for temperatures in the range kT_{Low}=$10^{-0.8}$ to kT_{High}=$10^{+0.2}$ keV and N_H equal to $10^{19.6}$ (black), $10^{20.0}$ (red), $10^{20.4}$ (green) and $10^{20.8}$ (blue) atoms cm^{-2}.

Adopting the same method as described for Sample 1, but using a temperature range of $10^{-0.8}$ to $10^{+0.2}$ keV and an N_H range of $10^{19.6}$-$10^{21.2}$ cm^{-2} we have assigned upper and lower limits for the N_H towards each source. Again, sources with extreme colour ratios are excluded from the analysis (these sources are plotted as red dots in Figure 3.7).

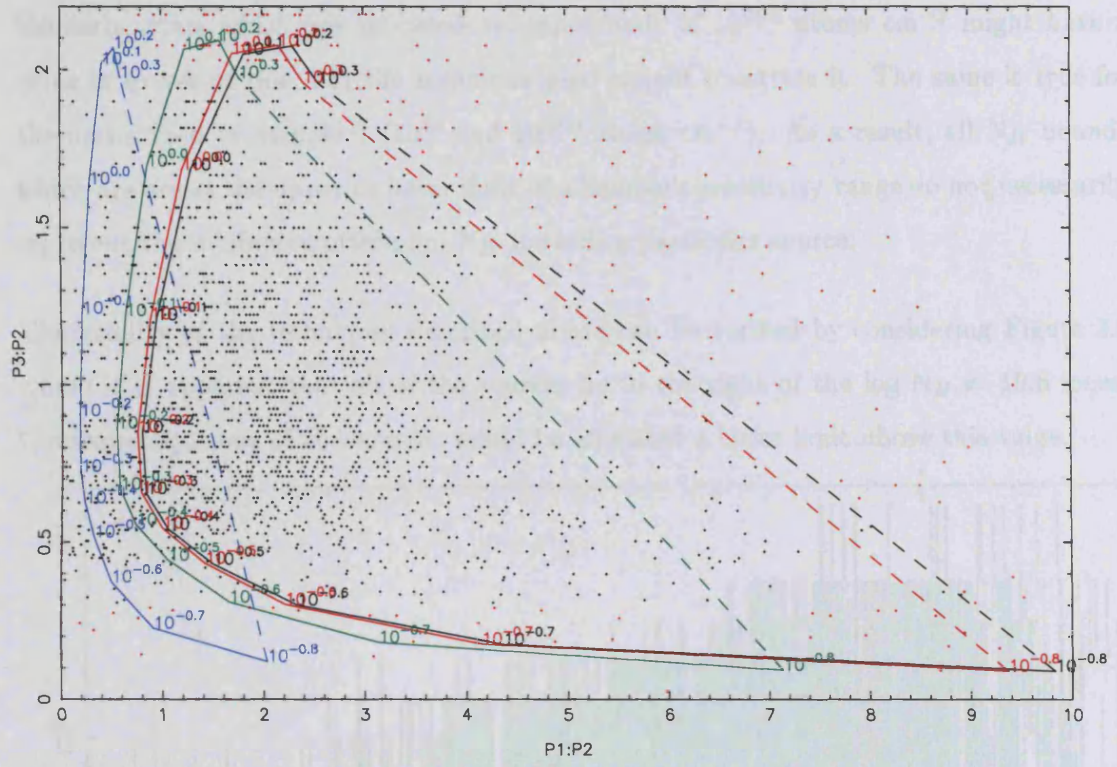

Figure 3.7: Two colour plot for the Sample 2 stars. The ratio errors have been omitted for clarity (see figure 3.5 for typical errors). The curves represent the ratios obtained with a single temperature plasma for absorption columns of $10^{19.6}$ (black), $10^{20.0}$ (red), $10^{20.4}$ (green), $10^{20.8}$ (blue) cm^{-2}. The points plotted in red are those excluded from this analysis.

3.7 Discussion

Figure 3.8 presents the HI column density ranges for the sources in both samples as a function of distance (derived from the HIPPARCOS parallax). The column density ranges are $\sim$ 90% confidence limits in the worst case. This is because for the cases where only an upper limit is provided for the S2 count-rate, there is only a 90% range on the S2:S1 ratio to constrain the fit to N_H.

The dashed lines represent the range of values determined for stars in Sample 1 and the solid lines represent the ranges for sources in Sample 2. When comparing the N_H limits for the two different samples in Figure 3.8, it should be noted that the minimum value of N_H allocated to Sample 2 stars was $10^{19.6}$ atoms cm^{-2}. This does not mean that the HI column density towards these stars is in excess of this value, but rather, $10^{19.6}$ atoms cm^{-2} represents the limit of the sensitivity to N_H of the technique used for that sample.

Similarly, stars which are allocated an upper limit of $10^{21.2}$ atoms cm^{-2} might have a value in excess of this, but the technique used cannot constrain it. The same is true for the limits used in Sample 1 (10^{18} and $10^{19.6}$ atoms cm^{-2}). As a result, all N_H bounds which are are at the upper or lower limit of a Sample's sensitivity range do not necessarily represent the minimum/maximum N_H towards a particular source.

The validity of the techniques described above can be verified by considering Figure 3.5 where it is apparent that all of the sources lie to the right of the log $N_H = 19.6$ locus. Consequently, none of the sources would be allocated a lower limit above this value.

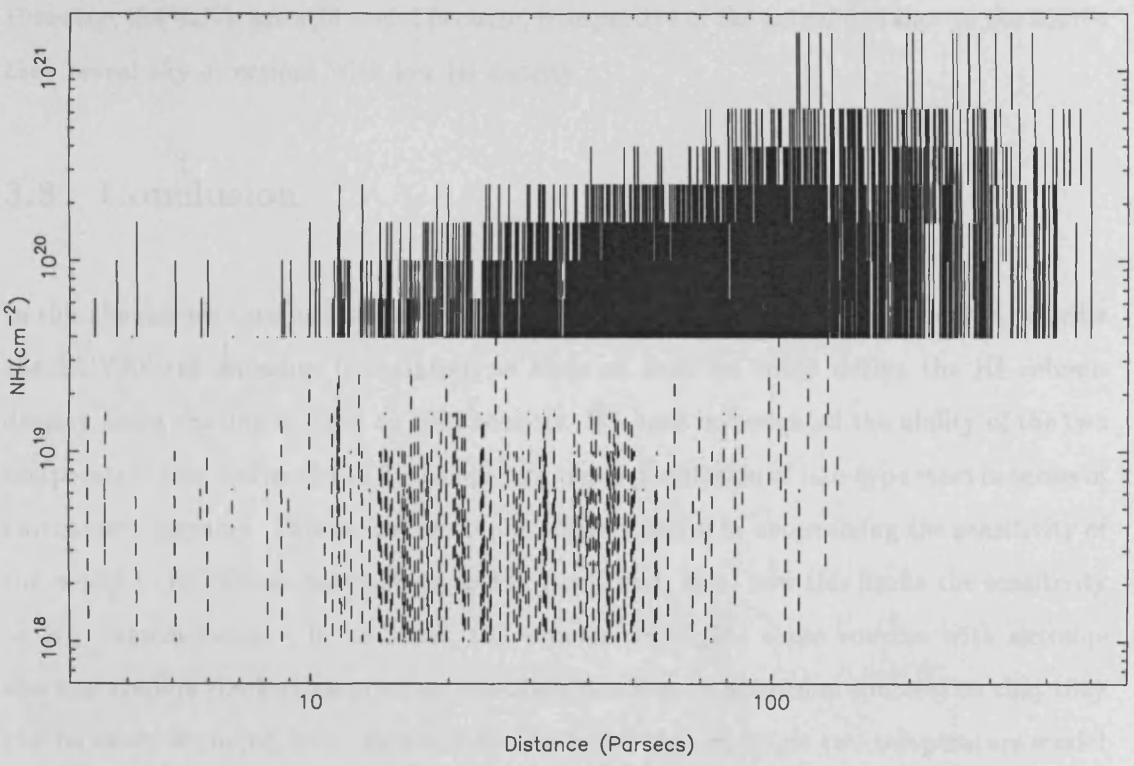

Figure 3.8: The range of column densities derived for the sources in each sample. The dashed lines define the ranges derived for sources in Sample 1 while the solid lines define the ranges derived for sources in Sample 2.

The combination of the two datasets provides 1987 column density estimates over the range 10^{18} to $10^{21.2}$ atoms cm^{-2}. The distance distribution of the sources provides sensitivity to regions of the local ISM between 3 and 500 pc, while the total number of sources provides a sky coverage of approximately 1 source in every 5 degree^2 of sky. The distance versus N_H correlation in Figure 3.8 for the sources in Sample 2 is clear, and indicates that the procedure for allocating column densities is reasonably successful. However there is a large

spread in the column density measurements obtained for a given distance bin (by up to an order of magnitude) which indicates that there is substantial variation in HI density for a given sky direction. This is consistent with the sky coverage obtained for the sources in Sample 1 where there is clear evidence for reduced number densities towards the Galactic centre and increased densities in clusters elsewhere (see Section 3.4 for details).

Although there is a trend of increasing N_H with distance for stars in Sample 1, it is not very strong because of the large error band associated with the upper and lower limits. Consequently it is difficult to determine the radial HI distribution for these sources. However, the bands are still useful because, irrespective of the actual distance to the source they reveal sky directions with low HI density.

3.8 Conclusion

In this chapter we have used a standard two-temperature thermal plasma model to describe the EUV/X-ray emission from late-type stars so that we could derive the HI column density along the line-of-sight to 1987 sources. We have investigated the ability of the two temperature thermal model to fit the spectra of our population of late-type stars in terms of two colour diagrams. This procedure is particularly useful in determining the sensitivity of the model to its various parameters, and in particular, as to how this limits the sensitivity to N_H determination. In addition, the process highlights those sources with extreme spectral colours (indicating possible mis-identifications or abnormal sources) so that they can be easily excluded from the analysis. We found that no single two temperature model could be used for all the sources since the variation in spectral ratios obtained for different choices of T_1 and T_2 was at least as large as that due to HI absorption. This led to the use of N_H limits (90% confidence) to describe the range of HI which could be accurately allocated allowing for the diversity in intrinsic emission. The correlation between these column densities and source distances indicates that the procedure is reasonably successful, but that the scatter in N_H for a given distance bin is indicative of a non-uniform distribution of HI in the local ISM. The actual distribution of this material is considered in detail in the following chapter.

Chapter 4

Investigating the Structure of the Local ISM

Overview

This chapter describes an investigation of the distribution of cool absorbing gas in the local interstellar medium. The line of sight HI column density observed towards 2477 stellar sources is used along with accurate HIPPARCOS parallaxes to map out the distribution of cool gas within 500 pc of the Sun. The stellar data set includes the two samples derived in the previous chapter as well as two further samples taken from the literature.

4.1 Introduction

Previous investigations of the local interstellar medium (LISM) have revealed some interesting features in the distribution of cool, absorbing gas. EUV surveys, such as those by; Frisch & York (1983) (hereafter FY83) and Paresce (1984) (hereafter P84) have made use of data from the Copernicus and International Ultraviolet Explorer (IUE) missions to map out the distribution of HI out to distances >300 pc. Such maps demonstrate that the neutral gas distribution is asymmetric and that the typical interstellar density within 100 pc of the Sun is considerably lower ($\sim$0.07)cm^{-3} than the Galactic average (n_H $\sim$0.5cm^{-3}; Dickey & Lockman 1990). These studies also revealed evidence for large density discontinuities towards the Sco-Cen and Per associations and for a region of very low HI column density towards l^{II}=220°, the direction of the star Beta Canis Majoris (β CMa).

Further evidence for a cavity in the local distribution of cool interstellar gas arises from studies of the soft X-ray background. As discussed in Chapter 2, it has been shown that there is a tight correlation between soft X-ray intensity and Galactic latitude which has been interpreted in terms of the displacement model. It is proposed that the cavity is filled with hot 10^6K gas and that as the distance to the cavity edge increases so does the path length of the emitting material and hence the emission measure of the gas. Clearly, in this model, variations in the intensity of the soft X-ray background provide an indirect method for mapping the extent and shape of the cavity. The results of such studies indicate that the emitting volume has a mean radius of 60-90 pc with evidence for extensions out to 100-200 pc at high Galactic latitudes.

Adopting an alternative technique, Welsh *et al.* (1994) (hereafter W94) mapped the local distribution of HI using a relationship between NaI column density and HI column density. In their study, the authors used high resolution NaI D1 and D2 interstellar absorption lines towards 293 early-type stars (within 300 pc) to infer N_H. Their results verify the presence of a low density cavity with mean radius $\sim$ 60 pc and also indicate the presence of an interstellar tunnel towards the star β CMa.

More recently, statistical studies of the brightest EUV sources, (late-type stars and white

dwarfs) have revealed further evidence for an inhomogeneous LISM. Work on the ROSAT WFC all-sky survey by Warwick *et al.* (1993) (hereafter WK93) and on the EUVE all-sky survey by Vallerga (1996) have demonstrated that the sky density of sources is far from uniform. In both studies there is clear evidence for a reduction in source density towards the Galactic centre and for an enhancement towards the south of Galactic quadrant III. Warwick *et al.* (1993) also demonstrate evidence for the local cavity and comment on a source density enhancement in the North of Galactic Quadrant II, towards (l^{II}=120°, b^{II}=45°) where it appears the cavity is particularly extended. The presence of a bright feature in the soft X-ray background in this direction is at least qualitatively in agreement with the displacement model (see Snowden *et al.* 1990). Diamond, Jewell & Ponman (1995) (hereafter D95) have also used a subset of the ROSAT WFC sources to investigate the distribution of cool absorbing gas. In their study, the authors derived N_H by fitting the absorbed EUV spectra of 79 late-type stars and white dwarfs. As a result, they demonstrated that there is good evidence for a low density ($n \sim 0.1$ cm^{-3}) cavity and that there is a large increase in N_H towards the Galactic centre. However, at odds with previous studies, they demonstrated that N_H does not rise to greater than 10^{20} atoms cm^{-2} within 100 pc of the Sun.

The different data sets discussed above give varying pictures of the local interstellar medium (see Table 4.1 for a summary), but nevertheless the presence of a low density cavity is reported in all of the studies. In addition, a "wall" of absorbing material ~30 pc away in the direction of the Galactic centre is reported by FY83, P84, WK93 & D95) and a region in the direction of β CMa is identified as sampling an ultra-low gas density by most of the studies. The differences between the various views of the LISM arise from inaccuracies in the stellar distances, poor sky coverage and limitations in the measurements of N_H.

As indicated in the previous chapter, there now exists a very large database of late-type stars with ROSAT EUV and X-ray data which have accurate distance measurements as a result of the HIPPARCOS survey. Consequently, we are now in a position to expand on the survey conducted by Diamond, Jewell & Ponman (1995) with improved sky coverage and distance estimates. To improve on the statistics even further, we combine these data with two published data sets to obtain a total of 2477 HI column density measurements

across the sky. This translates to an average sky coverage of ~1 source per 12 degree^2.

Study	Technique	d_c pc	n_1 cm^{-3}	n_2 cm^{-3}	$d_{\beta CMa}$ pc	d_{near} pc
FY83	UV/Optical	-	-	-	>200	-
P84	UV	-	0.07	-	>200	10
W94	NaI	60	-	0.5	-	20
WK93	EUV	80	0.05	0.5	250	30
D95	EUV	70	0.04	0.5	250	25-30

Table 4.1: A summary of the features identified in the various studies of the local interstellar medium, d_c is the average radius of the low density cavity, n_1 is the internal cavity density, n_2 is the typical ISM density beyond the cavity edge, $d_{\beta CMa}$ is the distance to the cavity edge in the direction of βCMa and d_{near} is the minimum distance to the cavity edge.

4.2 The Data

The data considered here were obtained from four separate studies of stellar sources and include the HI column density (and its error), the distance to the source, the spectral classification and the Galactic coordinates. The nature of each sample is discussed in detail below.

4.2.1 Sample 1

This is the collection of late-type stars derived in the previous chapter which have EUV, X-ray and HIPPARCOS data. The energy band covered by these observations is sensitive to HI column densities in the range 10^{18}-$10^{19.6}$ atoms cm^{-2} and the sources sample distances out to 60 pc. The ranges quoted for the N_H are ~90% confidence intervals. It should be noted that the column densities in this dataset are limited to the above range so that sources which hit the lower band are upper limits and the sources which hit the upper bound are lower limits.

4.2.2 Sample 2

Sample 2 consists of the late-type stars from the second sample in Chapter 3. It includes the late-type stars found in the RASS catalogue which also have HIPPARCOS parallaxes. This energy band is sensitive to column densities in the range $10^{19.6}$ atoms cm^{-2}-$10^{21.2}$ atoms cm^{-2}. Again, the values are quoted with ~90% confidence intervals and values at the extremes of the range are upper and lower limits.

4.2.3 Sample 3

This sample consists of the DA white dwarfs detected by the ROSAT WFC. The data are taken from a study conducted by Marsh *et al.* (1997). The authors combined EUV data from the WFC with ROSAT PSPC X-ray fluxes and optically determined temperatures and gravities to fit detailed atmospheric models. As a result, they determine both HI column densities and distances for 89 of the 125 white dwarfs listed in the 2RE catalogue.

4.2.4 Sample 4

Sample 4 incorporates a subset of the data published by Fruscione *et al.* (1994). In their paper they list the HI column density and distance towards 594 individual stars. The data in our subset of 242 stars consists of the most accurate N_H measurement for a particular source and excludes those values which are upper or lower limits. It should be noted that the distances quoted for these sources are those that appear in the literature and not those derived from HIPPARCOS parallaxes. Consequently, some distances could be inaccurate by up to a factor of two. The column densities were determined from a variety of surveys which include several different techniques for determining N_H. These techniques are discussed in detail below, particularly in terms of the accuracy to which they can determine N_H.

1. NaID Line

This technique adopts an indirect method for determining N_H. The equivalent width of the optical interstellar absorption lines of NaI, D1(5896Å) and D2(5890Å) are used in

conjunction with an empirical relationship between NaI column density and HI column density (Ferlet, Vidal-Madjar & Gry 1985). As indicated by Welsh (1991), the N_H values estimated from NaI measurements can be subject to large errors due to the wide range of electron temperatures and densities assumed in the empirical relationship. Fruscione *et al.* (1994) suggest that this can lead to errors in column density of up to a factor of three.

2. EUV observation

Observations of stellar sources at EUV and X-ray energies are very sensitive to the column densities of HI and He. These measurements are generally very accurate, but in extreme cases the error may be up to a factor of 5.

3. Lyα

Observations of the interstellar Lyα absorption feature towards emission from early or late-type stars can be used to derive N_H column densities. This technique can be accurate to within 30% for column densities $>10^{19}cm^{-2}$, but can only determine lower column densities to within factors of 2-5.

4. Curve of growth

This technique uses the abundance of ionisation species found in HI clouds to determine the HI column density towards stars. The curve of growth analysis determines the column densities of the ion species from their line strengths which are then combined with the observed correlation between the average depletion of metal ions and N_H column density to determine N_H. The curve of growth technique yields errors of approximately 50% because of uncertainties in the equivalent width measurements.

4.3 Data Analysis

The sky coverage of the four samples is shown in Figure 4.1. The spatial distribution of the white dwarfs is similar to that of the late-type stars in terms of the source deficient area towards the Galactic centre. As discussed in Chapter 3, the late-type stars selected from the RASS catalogue give an almost all-sky coverage. The Fruscione dataset gives patchy coverage with the majority of observations centered on the plane of the Galaxy

and the southern region of Galactic quadrant III.

The distance distributions of the four samples are shown in Figure 4.2, where it can be seen that Sample 4 spans the entire distance and N_H range of the other three samples. This is useful for checking consistency between the data sets. The HI column density is plotted as a function of distance for all four samples in Figure 4.3. In this plot the N_H bounds (determined in Chapter 3) have been replaced by the geometric mean of the upper and lower limits to improve clarity. Once again, it should be noted that the N_H range was limited to values between 10^{18} and $10^{19.6}$ atoms cm^{-2} for the fits to sources in Sample 1 so that N_H values of 10^{18} atoms cm^{-2} are actually upper limit estimates of the column density and N_H values of $10^{19.6}$ atoms cm^{-2} are lower limit estimates. Similarly, in Sample 2, the N_H range was limited to values between $10^{19.6}$ atoms cm^{-2} and $10^{21.2}$ atoms cm^{-2} so that allocations of N_H equal to $10^{19.6}$ and $10^{21.2}$ atoms cm^{-2} are upper and lower limit estimates respectively.

Accounting for these limits, there is clearly good agreement between the sources in Samples 1 and 2 and the sources in Sample 4. Since the HI column density measurements for the sources in the fourth sample are completely independent of those in Samples 1 and 3, this demonstrates that the N_H values determined in Chapter 3 are reasonable. However, the column densities for the white dwarfs are consistently below those seen for sources at the same distance in the other samples.

Figure 4.3 clearly indicates that there is a general increase in column density with distance, but that there is considerable scatter in the data, with the observed column density for a particular 10 pc distance bin varying by up to an order of magnitude. This scatter indicates that there is either; a significant variation in the density of cool absorbing gas along the line of sight or significant variation in density with sky direction. To investigate how significant the scatter is and how alternative models might explain it, we now consider a statistical analysis of the data.

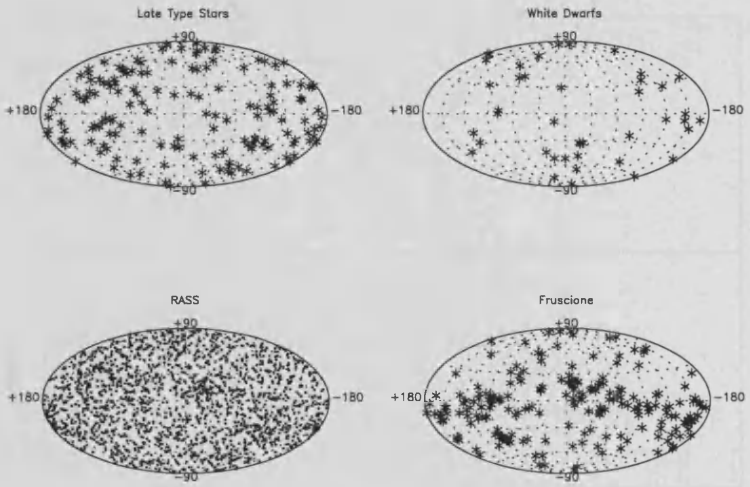

Figure 4.1: The sky coverage of the four data-sets.

4.3.1 Statistical analysis

Usually, a χ^2 fit is used to describe how well a model matches the data. However, as discussed in Chapter 3, we were not able to determine the most probable value of N_H for the sources in Samples 1 and 2, which the χ^2 approach requires. Instead, we define a statistic, **dev**, based on the upper and lower limits we have obtained for N_H (see Hutchinson, Warwick and Willingale 1998).

A measure of the ability of a model to fit such data can be defined as:

$$\begin{array}{lllll} & dev & = \log_{10}(N_{HLow}) - \log_{10}(N_{HPred}) & \text{for} & N_{HLow} > N_{HPred}, \\ & dev & = \log_{10}(N_{HPred}) - \log_{10}(N_{HUp}) & \text{for} & N_{HUp} < N_{HPred} \\ \text{and} & dev & = 0 & \text{otherwise} & \end{array}$$

where N_{HLow} is the lower limit of N_H, N_{HUp} is the upper limit of N_H and N_{HPred} is the N_H predicted by a given model for the distribution of HI in the ISM. The upper and lower limits of N_H for the sources in Samples 3 and 4 have been determined from the errors quoted in the literature.

Using these definitions we can construct a statistic, D, by summing the modulus of the deviations (*dev*) and normalising to the total number of sources in the sample. This normalisation includes those sources which do not contribute to dev so that the statistic decreases as the fit to the model improves:

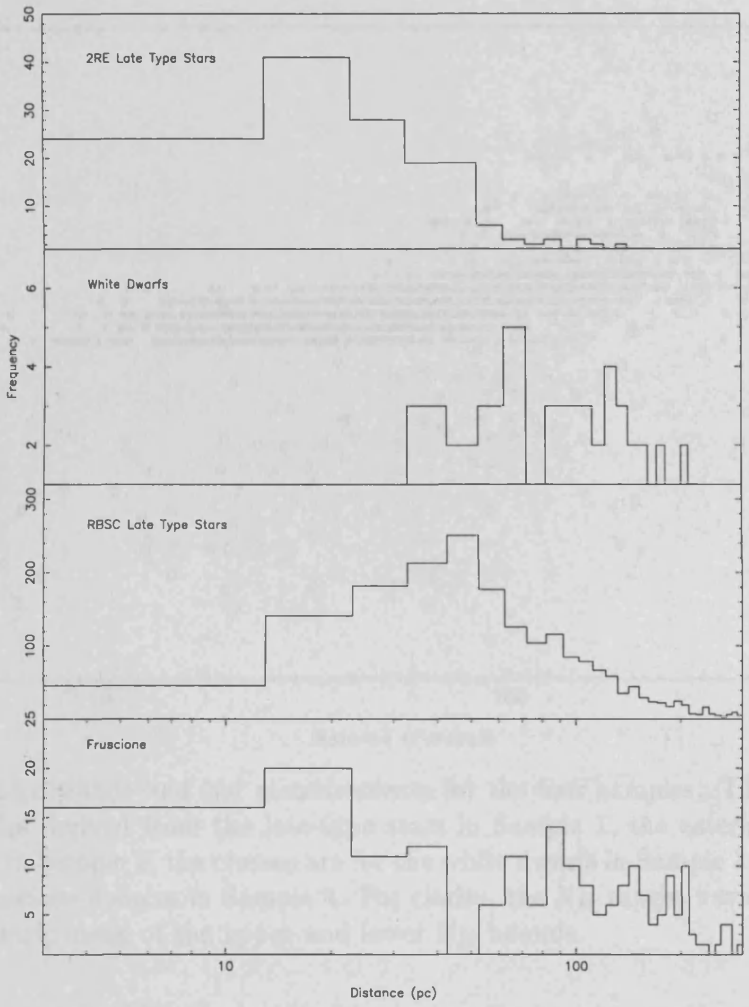

Figure 4.2: The distance distributions of the four samples which shows the different regions of the ISM that they are sensitive to.

$$D = \frac{\sum(|dev|)}{n_s}$$

where n_s is the total number of sources in the data set.

It should be noted that since *dev* is equal to zero for all sources whose predicted HI column density lies within the N_H error range, the statistic is purely driven by the sources which do not initially fit the model. To interpret the value of the statistic it is necessary to determine the probability distribution of the D function. If it is assumed that the upper and lower N_H limits of the N_H error range are drawn from a normal distribution with rms width σ, we can determine the expectation value and standard deviation of *dev*. These quantities vary with the confidence range of the error bars and this dependence can be

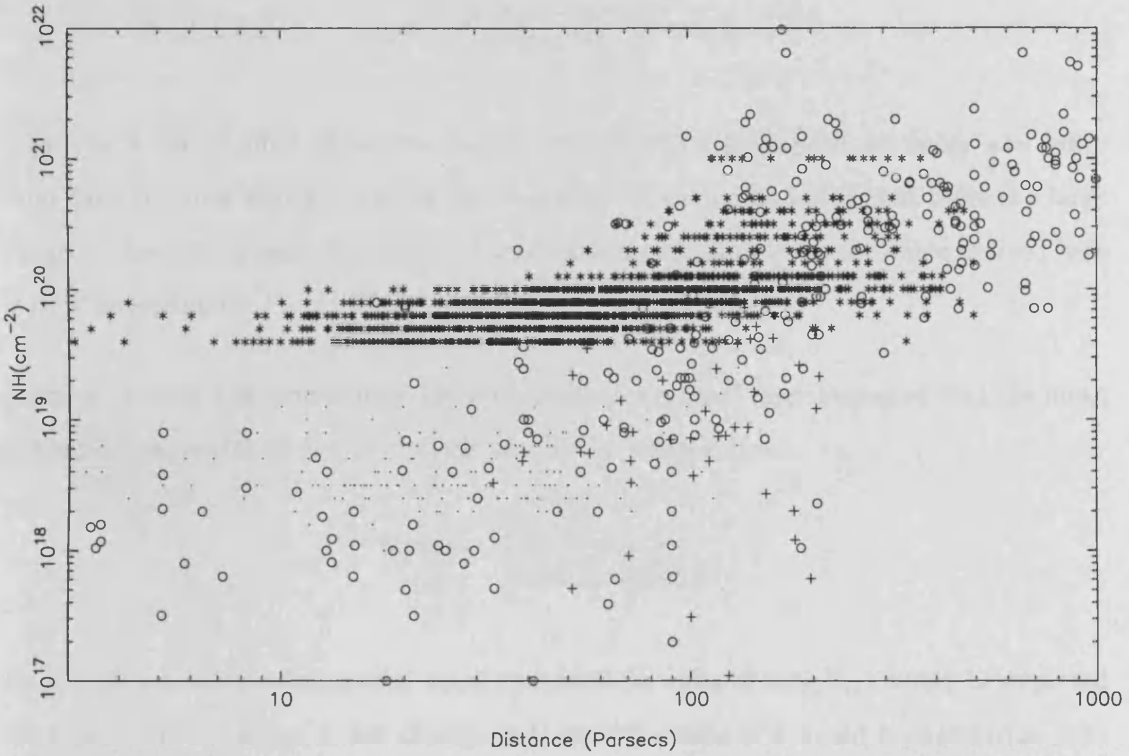

Figure 4.3: The distance and N_H measurements for the four samples. The dots are the column densities derived from the late-type stars in Sample 1, the asterisks are for the late-type stars in Sample 2, the crosses are for the white dwarfs in Sample 3 and the circles are for the Fruscione sources in Sample 4. For clarity, the N_H ranges have been replaced with the geometric mean of the upper and lower N_H bounds.

determined by numerical integration to give:

$$\begin{aligned} < dev > &= \sigma\times\ (0.553\mathrm{f}^2{+}0.359\mathrm{f}) \\ (< dev^2 > - < dev >^2)^{1/2} &= \sigma\times\ (0.360\mathrm{f}{+}0.427\mathrm{f}^{1/2}) \end{aligned}$$

where f is the fraction of sources which have a non-zero deviation and is equal to 1-C_l, where C_l is the confidence region covered by the error bar.

These relationships were calculated to an accuracy of ~0.3% and have been confirmed by Monte Carlo simulation to an accuracy of ~2% (Willingale 1998; priv. communication). An estimate for σ (representative of all four samples) can be obtained from the typical size of those error bars in the dataset which are not constrained by the bounds that were imposed on the N_H limits (i.e. not including those sources with upper or lower N_H values at the extremes of the dataset). Since the confidence limits for these data are approximately 90% (see Chapter 3) then,

$$\sigma = \frac{\sum(logN_{Hhi} - logN_{Hlo})}{(n_l \times 2 \times 1.645)} = 0.2$$

where n_l is the number of sources in this sample which have both an upper and lower limit (and includes sources from all four samples). It should be noted that there is a large range in the sizes of error bars between and within each sample, so the value derived here is only approximate.

Since n_s is large, the central limit theorem predicts a normal distribution so that the mean value and rms width of the D statistic can be determined from:

$$\begin{aligned} \text{mean} &= < dev > \\ \text{rms} &= (\frac{<dev^2> - <dev>^2}{n_s})^{1/2} \end{aligned}$$

Hence, for a σ of 0.2, a value of D equal to 0.0083 (in units of $\log_{10}N_H$) would be expected for a good fit, and a significant change in D at 90% confidence would be 0.0011 (in units of $\log_{10}N_H$). These "figures of merit" are now used to quantify the quality of fit provided by the various models.

4.4 Models for the distribution of cool gas in the local ISM

Here, we discuss three different models for the distribution of cool absorbing gas in the local ISM. Firstly, we consider a uniform density model.

4.4.1 Uniform density model

The constant density model has the form:

$$N_{Hpred} = n_1 d \tag{4.1}$$

where N_{Hpred} is the predicted column density, n_1 is the gas density and d is the distance in parsecs to the source.

To determine the best fit value for n_1 we searched for a minimum in the D statistic as n_1 was varied over the range 0.0 to 0.5 cm^{-3}. A minimum D value of 0.0957 was obtained

for n_1 equal to 0.18 cm^{-3} with a 90% confidence range of 0.15-0.21 cm^{-3} (see Figure 4.4 (a)). The upper horizontal line represents a D value of (0.0957+0.0011) and thus defines the 90% confidence range for the best fit to n_1. The lower horizontal line is at a D value of 0.0083 which was the value determined to be a good fit in the previous section. The sources which contribute to *dev* for a uniform density model with the best fit value of n_1 are shown in Figure 4.4 (b). The solid line represents the predicted value of N_H. There are clearly a large number of residuals from this model. In particular, it appears that at distances beyond ~40 pc the N_H prediction is significantly below the value observed for many of the sources. To account for this, we now consider models in which the density can vary with distance.

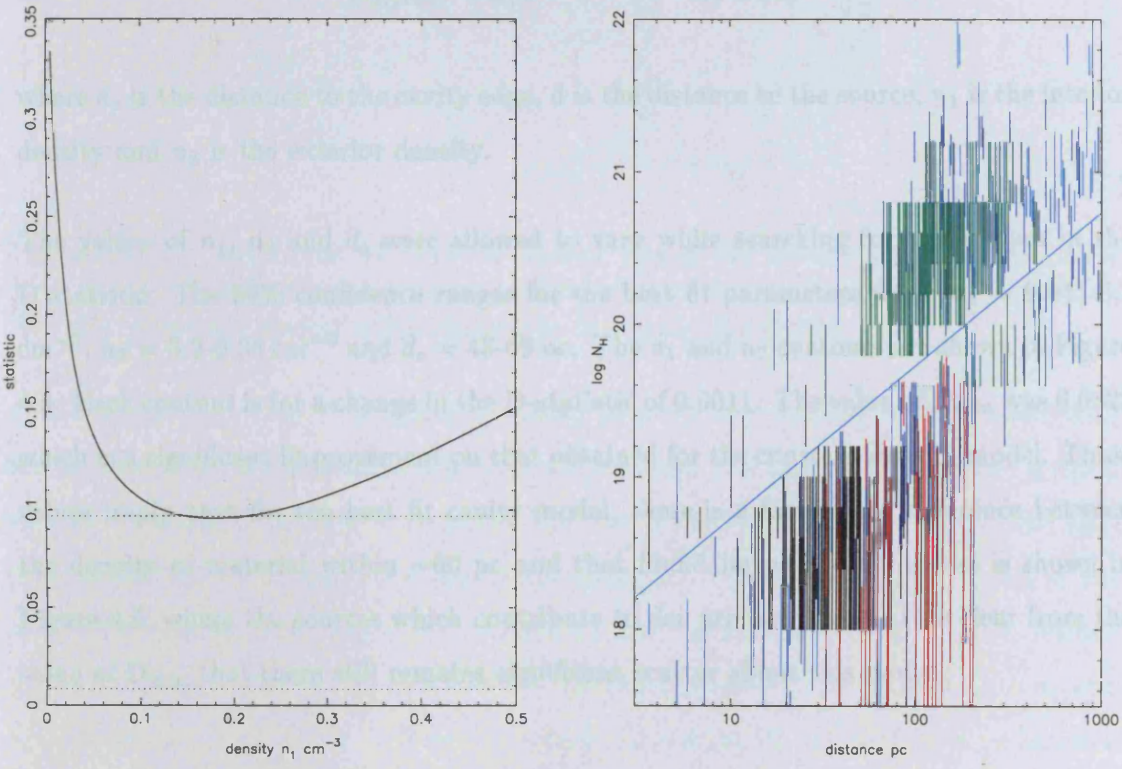

Figure 4.4: The plot on the left shows the value of the D statistic obtained for various values of n_1. The upper horizontal lines represents a value of the D statistic 0.001 above the minimum obtained and so defines the 90% confidence range of n_1. The lower horizontal line represents the value of the D statistic which defines a statistically *good* fit. The plot on the right shows the sources in each sample which are contributing to the statistic. The black lines represent Sample 1, the green lines represent Sample 2, the red lines represent Sample 3 and the blue lines represent Sample 4.

4.4.2 Spherical cavity model

As described in Section 4.1, a number of studies have indicated that the Solar System resides in a cavity of low density material. Thus, we now consider a two density model in which there is an abrupt increase in density at some radius, i.e. a cavity with internal density n_1 which resides in a medium with density n_2. In this model it is assumed that the increase in density occurs at the same radius for all sky directions. Hence the predicted column density has the form:

$$\begin{array}{lll} N_{Hpred} & = n_1 d + n_2 (d - d_c) & \text{for } d > d_c \\ N_{Hpred} & = n_1 d & \text{for } d < d_c \end{array}$$

where d_c is the distance to the cavity edge, d is the distance to the source, n_1 is the interior density and n_2 is the exterior density.

The values of n_1, n_2 and d_c were allowed to vary while searching for a minimum in the D statistic. The 90% confidence ranges for the best fit parameters were: n_1 = 0.045-0.1 cm^{-3}, n_2 = 0.2-0.38 cm^{-3} and d_c = 43-69 pc. The n_1 and n_2 contours are shown in Figure 4.5. Each contour is for a change in the D-statistic of 0.0011. The value of D_{min} was 0.0822 which is a significant improvement on that obtained for the constant density model. These values imply that for the best fit cavity model, there is a factor four difference between the density of material within ~60 pc and that found beyond. This model is shown in Figure 4.5, where the sources which contribute to *dev* are also shown. It is clear from the value of D_{min} that there still remains significant scatter about this model.

4.4.3 A non-spherical cavity model

As mentioned in the previous section, the plot of N_H versus distance for the spherical cavity model still reveals significant residuals about the best fit model. To investigate if these demonstrate any correlation with sky direction, we smoothed the distribution of dev across the sky using spherical harmonics. By including only the harmonic functions up to order l=4 in the reconstructed image, we obtained a resolution of ~45 degrees with approximately 150 sources in the smallest area of the sky represented by the harmonics.

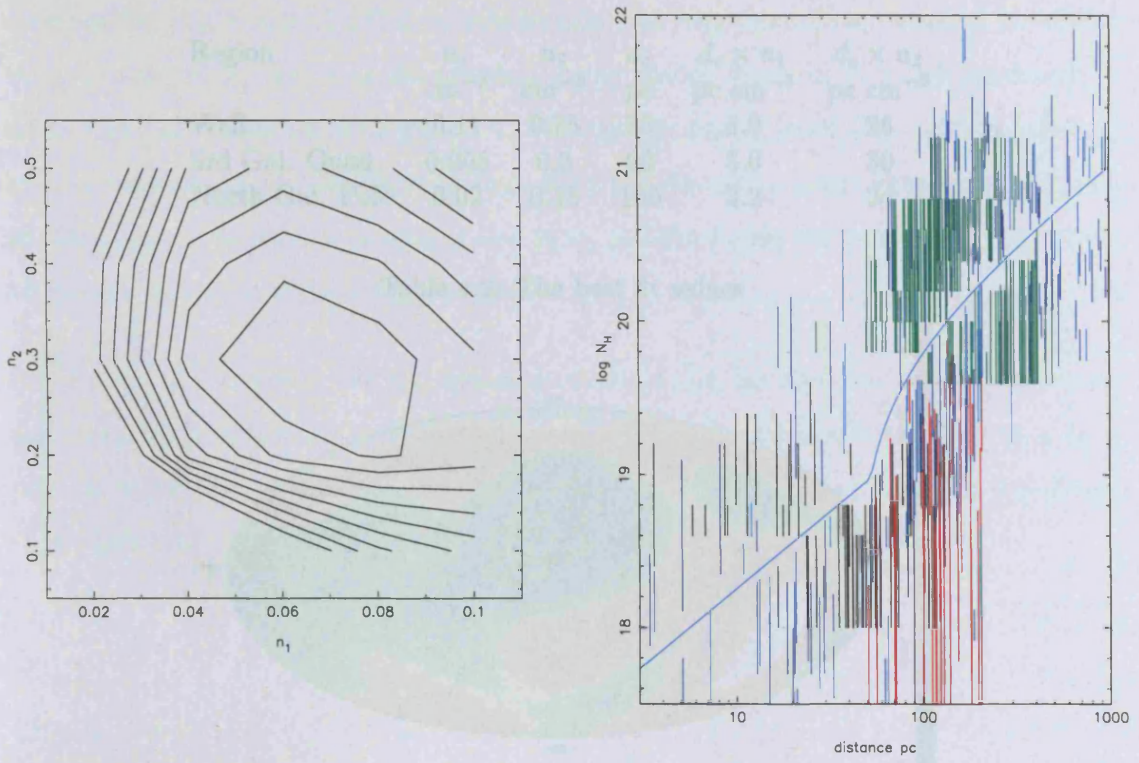

Figure 4.5: The plot to the left shows a contour map of the D-statistic for various values of n_1 and n_2. Each contour represents a change in the D-statistic of 0.0011. The plot to the right shows the sources which contribute to *dev* for this model.

A plot of the smoothed D statistic projected onto the sky (see Figure 4.6) shows that the deviations do demonstrate some coherent structure and that there are three distinct regions; (i) towards the North Galactic Pole, (ii) towards the Galactic centre and (iii), towards the Southern region of Galactic Quadrant III. Using the smoothed value of the D-statistic to define these areas, we performed fits to the data from the individual regions of the sky. The results appear in Table 4.2. Evidently, there is a decrease in both n_1 and n_2 towards the North Galactic Pole and Galactic Quadrant III, while there is an increase in both densities towards the Galactic centre region. It is also apparent that the distance to the cavity edge increases towards the North Galactic pole and Galactic Quadrant III and decreases towards the Galactic centre. In fact, the products; $d_c \times n_1$ and $d_c \times n_2$ remain remarkably constant with sky direction.

Clearly, there is evidence that the cavity radius varies with sky direction and so in our final model we consider the case of a non-spherical cavity. We use the relationship between n_2 and d_c outlined above to reduce the model to effectively two free parameters; n_1 and

Region	n_1 cm^{-3}	n_2 cm^{-3}	d_c pc	$d_c \times n_1$ pc cm^{-3}	$d_c \times n_2$ pc cm^{-3}
Wall	0.11	0.75	35	3.8	26
3rd Gal. Quad.	0.055	0.3	90	5.0	30
North Gal. Pole	0.02	0.15	160	3.2	24

Table 4.2: The best fit values

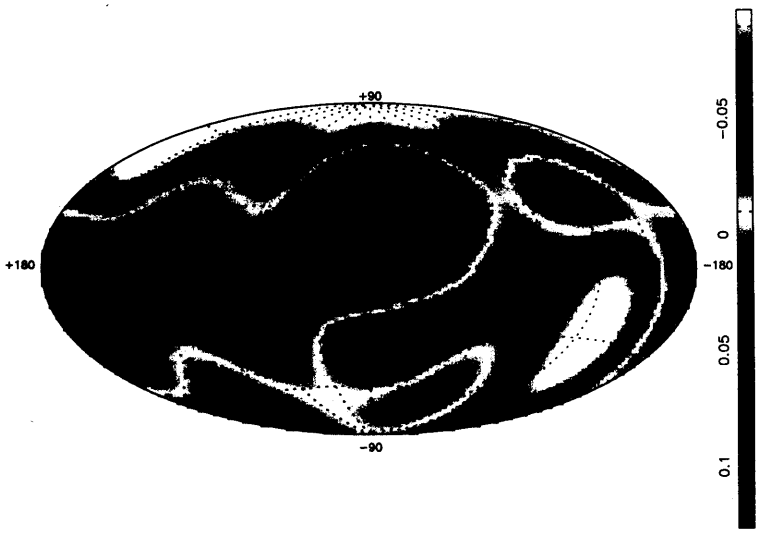

Figure 4.6: An aitoff projected plot of the D-statistic smoothed across the sky using spherical harmonics up to l=4

d_c, with n_2 constrained by the relationship:

$$n_2 \times d_c = 8.4 \times 10^{19} cm^{-2} \tag{4.2}$$

The fact that $n_2 \times$ d_c is constant with sky direction is consistent with the displacement model used to explain the distribution of hot diffuse gas which is thought to produce the soft X-ray background.

We found that the best fits for this model could be obtained with n_1 constant with sky direction and d_c allowed to vary according to a set of spherical harmonic functions up to l_{max}=4. The 90% confidence range obtained for n_1 was 0.045-0.08 cm^{-3}. The best fit values for d_c (and hence also n_2) are shown in Figure 4.7 (a). The 90% confidence range of the maximum cavity distance across the sky was 260-280 pc while the minimum cavity distance range was 29-33 pc. These values translate to a maximum n_2 in the range 0.97-0.85 cm^{-3} and a minimum n_2 in the range 0.11-0.1 cm^{-3}. The value of D_{min}

obtained for this model (0.0713) is significantly less than the values obtained for either the constant density model or the spherical cavity model. However, it is still considerably more than that expected for a good fit. The best fit model (solid line) and the sources which contribute to *dev* are shown in Figure 4.7 (b). Since the cavity distance varies with sky direction, both axes have been scaled by d_c and the y-axis has been offset by the N_H within the cavity for a given sky direction.

In a further refinement to the non-spherical cavity model, we also considered cases where the change in density from n_1 to n_2 was described by a smooth function rather than by a step. However, the improvements in D_{min} obtained for these models were not significant at the 90% level.

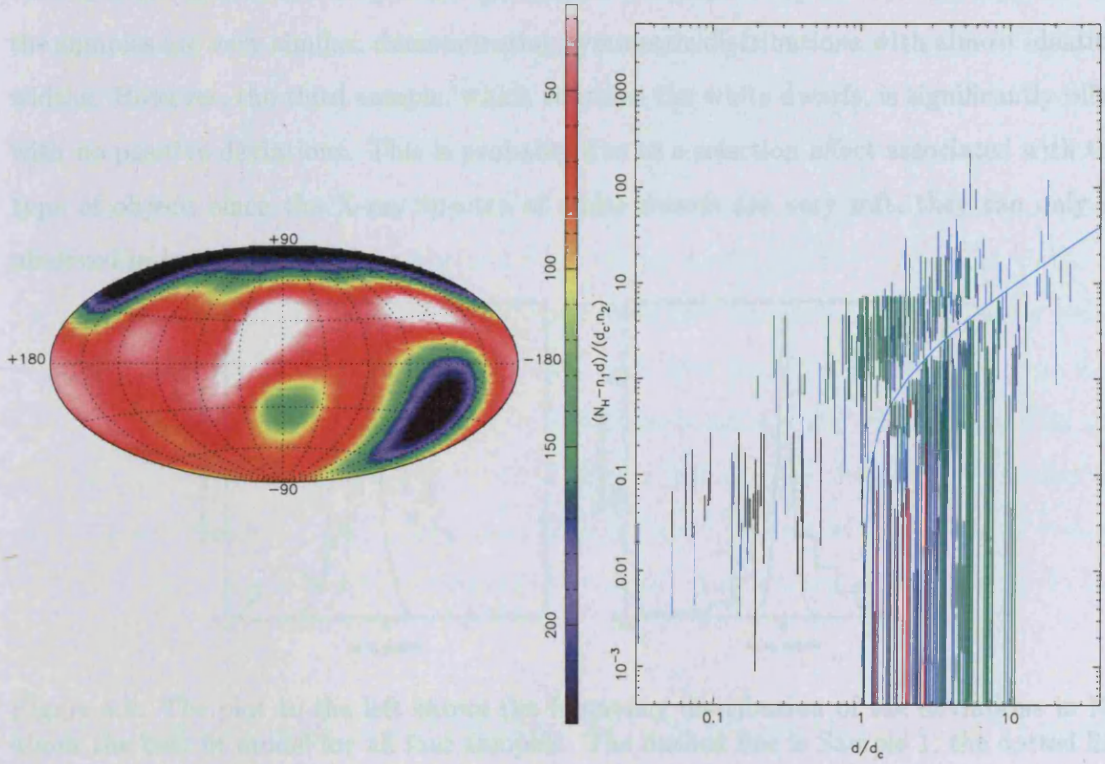

Figure 4.7: The plot to the left is an aitoff projection of the distance to the cavity edge. The values were smoothed using spherical harmonic up to order l=4. The plot to the right shows the sources which contribute to dev for this non-spherical cavity model.

4.5 Discussion and Implications

The best fit parameters for each of the models are summarised in Table 4.3. There is clearly a significant decrease in the D-statistic as the spherical and non-spherical cavity models are considered. However, even for the best fit model, the D_{min} value is substantially more than 0.0083, the value predicted for a **good** fit (see Section 4.3). In fact, the mean residual deviations from the best fit model (i.e. for a non-spherical cavity with l_{max}=4) are very small ($\log N_H \sim 3\times10^{-3}$) and the excess in D_{min} arises from large deviations in $\log_{10}N_H$ over smaller scale sizes than those considered here. The distribution of these deviations about the best fit variable cavity model are shown in Figure 4.8 (a). The contributions from each sample are normalised and shown separately. Clearly, three of the samples are very similar, demonstrating symmetric distributions with almost identical widths. However, the third sample, which contains the white dwarfs, is significantly offset with no positive deviations. This is probably due to a selection effect associated with this type of object; since the X-ray spectra of white dwarfs are very soft, they can only be observed in low density regions.

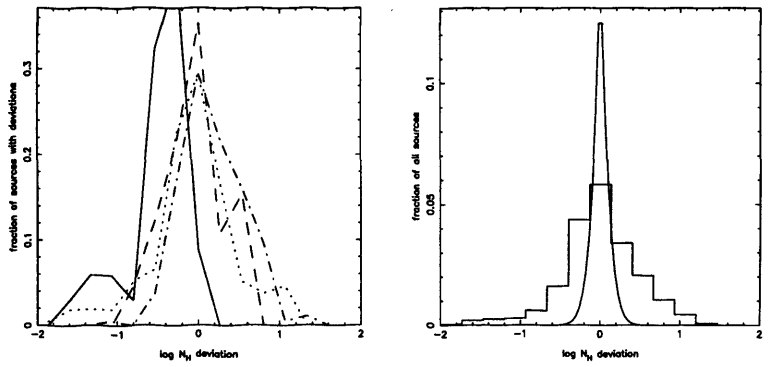

Figure 4.8: The plot to the left shows the frequency distribution of the deviations in N_H about the best fit model for all four samples. The dashed line is Sample 1, the dotted line is Sample 2, the solid line is Sample3 and the dot-dashed line is Sample 4. The plot to the right shows the combined deviations of the four samples compared to the deviations expected for a *good* fit.

Figure 4.8 (b), shows the deviations for the combination of all four samples in comparison to those predicted for a good fit (for 90% confidence ranges and σ =0.2). The spread of deviations about our best fit model is clearly much larger than that predicted for a good fit, while the fraction of sources with deviations (0.198) is also significantly more

than expected (0.1; see Section 4.3). Consequently, the map of the variation in d_c (and hence n_2) must only be considered as an average cavity radius for angular scales >45°. At smaller scale sizes, deviations up to $\log_{10}N_H \sim 1$ will be observed.

Model	n_1 cm^{-3}	n_2 cm^{-3}	d_c pc	D_{min}
Uniform Density	0.15-0.21	-	-	0.0957
Spherical Cavity	0.045-0.10	0.2-0.38	43-69	0.0822
Variable Cavity	0.045-0.08	0.10-0.85	29-280	0.0713

Table 4.3: The best fit values and the minimum in the D-statistic for each of the three models.

With the caveat that our model only describes the mean cavity radius for scale sizes $>45^0$, we now compare the map derived here with those obtained in other studies. Figure 4.9 shows the distance to a column density of 10^{19} atoms cm^{-2} according to our best fit model. The direction of β CMa is marked as an aitoff projected circle at l^{II}=225 and b^{II} =-15 and the region of the Galactic centre, noted to be a region of high HI density in most studies, is marked as a circle. The solid black line marks Gould's belt. The similarity between the distribution of high density material and this belt has been noted before (see Frisch & York 1983). However, attempts to fit this type of disk model to these data do not improve on the value obtained for the D-statistic (see Hutchinson, Warwick and Willingale (1998)). From an inspection of Figure 4.9 it can be seen that the distribution of high density material differs most significantly from Goulds belt in the region towards βCMa, which suggests that the low density "tunnel" in this direction hinders the fit to a disk distribution.

Figure 4.10 shows contour plots of the distance to HI column densities of 10^{19} and 10^{20} atoms cm^{-2}. The first contour is for material within the Galactic plane while the other three are for slices through the North and South Galactic Pole at 60° intervals (0°, 60° and 120°).

From Figures 4.9 & 4.10 it can be seen that the typical cavity radius is $\sim$ 60 pc and that in some regions there is no evidence for an increase in density at all. As discussed in the previous section, there are three main regions on the sky where the model differs significantly from a spherical cavity. Firstly, towards the North Galactic Pole it appears

that the cavity edge is as distant as 250 pc. Secondly, towards the Galactic Centre the cavity approaches as close as 30 pc and finally towards the β CMa region there is no evidence for an increase in density at all.

4.5.1 Comparison with other absorption studies

In general, there is a good degree of agreement between the Galactic plane contour in Figure 4.10 and the contours in the plot by D95 (see Figure 4.11 which includes results from the studies by P84, FR83 and W94).

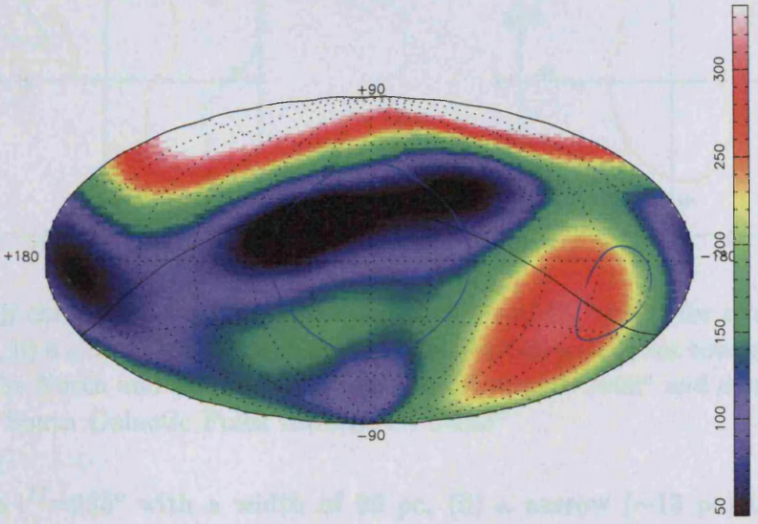

Figure 4.9: An aitoff projected plot of the predicted distance to a column density of 10^{19} atoms cm^{-2}. The region outlined in Galactic quadrant III is βCMa and the solid line is Gould's belt.

A recent re-analysis of the study by W94 (Welsh, Crifo & Lallement 1998) used Hipparcos parallaxes to obtain improved distance estimates for 290 of the stars in the original sample. The new data indicate that the cavity radius is >70 pc in most directions and that the low-density tunnel towards β CMa is a factor of two greater in diameter than previously suspected. The mid-plane distribution of NaI column density for stars with Galactic latitude between -35^o < b^{II} < +35^o is shown in Figure 4.12. The dashed line is the contour for $\log_{10}$N(NaI)$_{TOT}$ < 11.0 cm^{-2}. A comparison of the 10^{19}cm^{-2} contour in Figure 4.10 with the contour for a $\log_{10}$(NaI) column density of 11 (and hence a HI column density of $\sim 10^{19}$ atoms cm^{-2}) in Figure 4.12 demonstrates remarkable agreement.

Welsh, Crifo & Lallement (1998) identify three features in their contour, (i) an interstellar

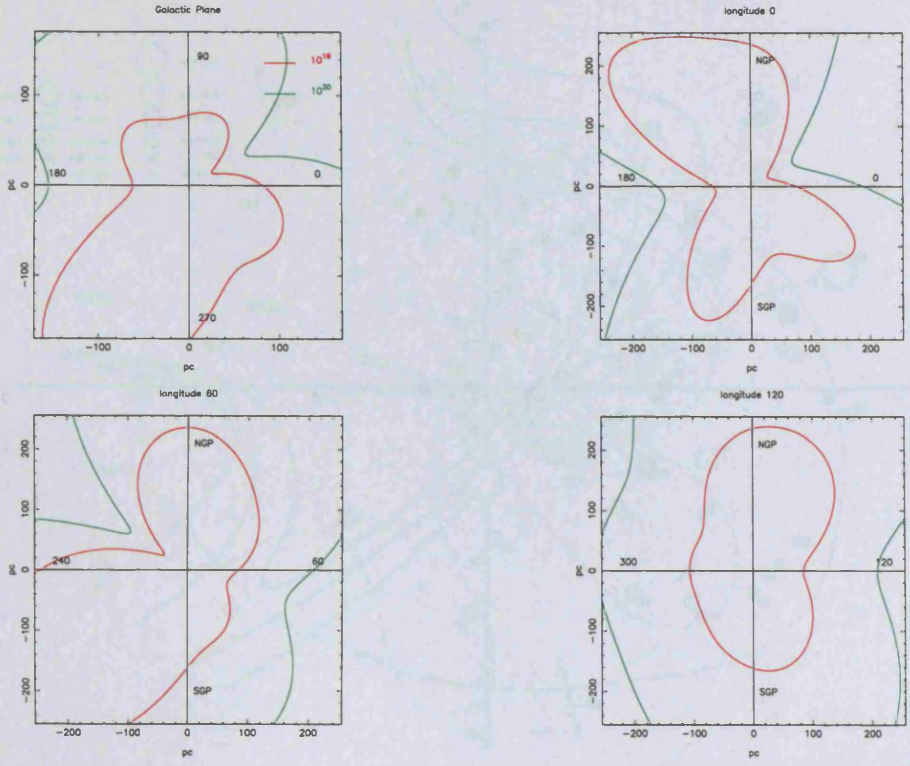

Figure 4.10: N_H contours for column densities of 10^{19} and 10^{20} cm^{-2} for a) material in the Galactic plane, b) a slice through the North and South Galactic Poles towards l^{II} =0°, c)a slice through the North and South Galactic Poles towards l^{II} =60° and d) a slice through the North and South Galactic Poles towards l^{II} =120°

tunnel towards l^{II}=235° with a width of 90 pc, (ii) a narrow (~15 pc) tunnel towards l^{II}=330° and (iii) a lack of dense gas towards l^{II}=135°. Each of these features is also clearly evident in Figure 4.10 although the low density region towards l^{II}=330° does not appear to extend quite as far.

4.5.2 Comparison with the X-ray view of the LISM

In a recent analysis of the ROSAT all-sky survey data, Snowden *et al.* (1998) used IRAS 100μm emission to disentangle (as far as possible) the foreground and background components of the 0.25 keV X-ray background and thus derived a map of the emission originating from within the local cavity. As noted previously, if the displacement model is assumed to be the mechanism by which the soft X-ray background is generated, then the variation in X-ray emission with Galactic latitude/longitude provides an indirect method for determining the dimensions of the local cavity. Contour plots of the cavity radius inferred

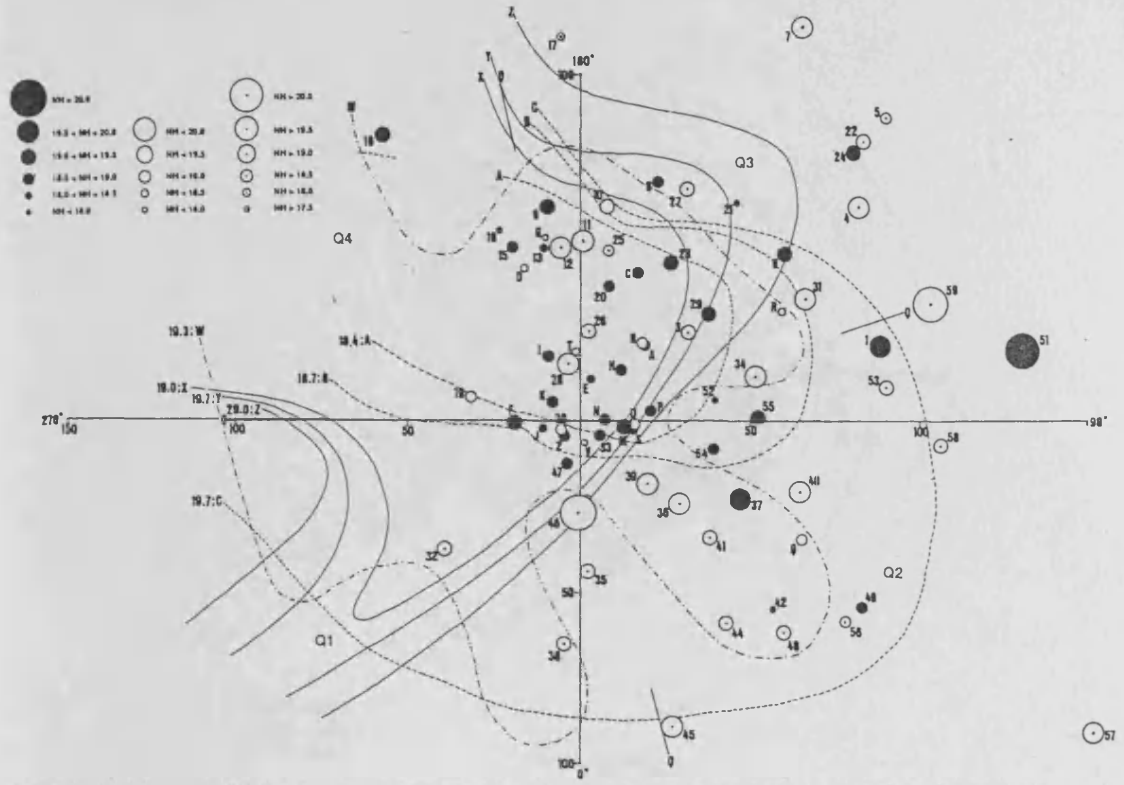

Figure 4.11: The N_H data from D95 projected into the Galactic plane and N_H contours from the P84 (solid lines) and FY83 (dashed lines) studies. The LISM boundary determined by W94 is shown as a dot-dashed line. The symbol indicate the nature of the data (solid=value, open=upper limit and dotted circle=lower limit), (taken from Diamond, Jewell & Ponman 1995).

from the relationship between X-ray intensity and emission measure are shown in Figure 4.13. Each plot is for the great-circle which cuts through the Galactic poles at the given Galactic longitude. Regions on these contours associated with discrete features in the soft X-ray background (and which are hence possibly contaminated) are shown as dashed lines. These plots should be compared with the 10^{20} cm^{-2} contours in Figure 4.10 since one optical depth is achieved for this column density in the 0.25 keV band.

A comparison of the contours for the direction towards l^{II}=0 demonstrates that there is a general agreement between the two views of the cavity regarding its shape, however there is considerable disagreement in terms of the extent of the cavity (assuming the extent is defined as the distance to a column density of 10^{20} atoms cm^{-2}). Both studies reveal a similar shape whose extent is restricted in the Galactic plane compared to higher Galactic latitudes. In both cases the cavity extends further north than south. The only major region of disagreement between the plots is towards b^{II}~-45°, l^{II}~180° where the

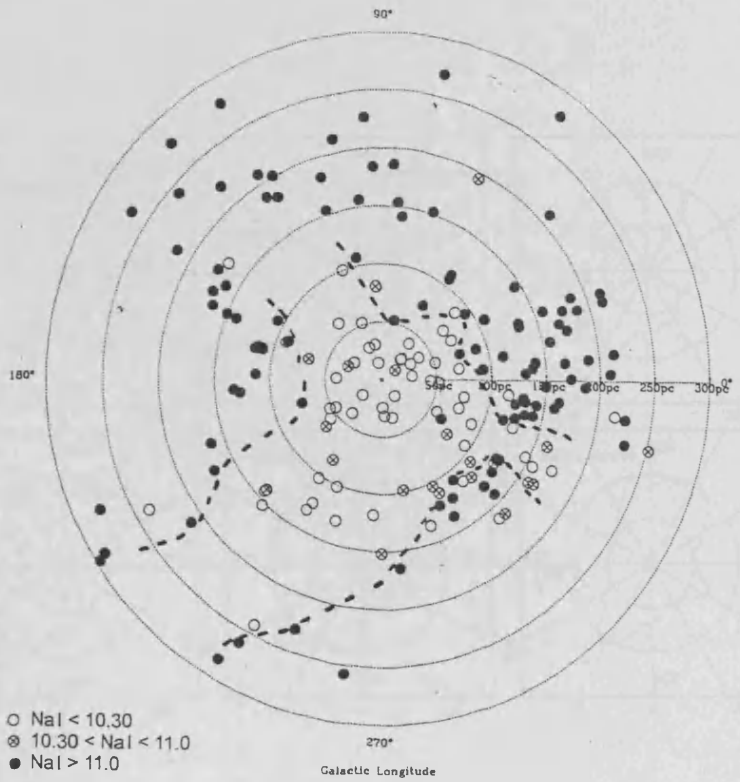

Figure 4.12: A projection of the NaI column densities towards a sample of stars with galactic latitude between -35° and +35° (taken from Welsh et al. 1998). The dashed line delineates a possible cavity.

absorption contour extends much further out than the X-ray contour.

The contours through l^{II}=60° also demonstrate good agreement, with both exhibiting shapes similar to those through l^{II}=0° but with a much restricted extent towards the bottom right of the plot. Again, the major difference between the plots is in the direction of b^{II}~-45°. However, the contours for l^{II}=120° are considerably different with the absorption view indicating a significant extension towards the bottom right of the plot which is clearly not the case for the X-ray view.

4.5.3 General features of the LISM

In agreement with almost all other studies of the LISM, the work presented here demonstrates evidence for a cavity in the local distribution of HI (radius $\sim$ 60 pc). However, perhaps the most interesting result is that there appears to be large scale fluctuations in N_H throughout the cavity. Such variations in the local distribution of HI have been re-

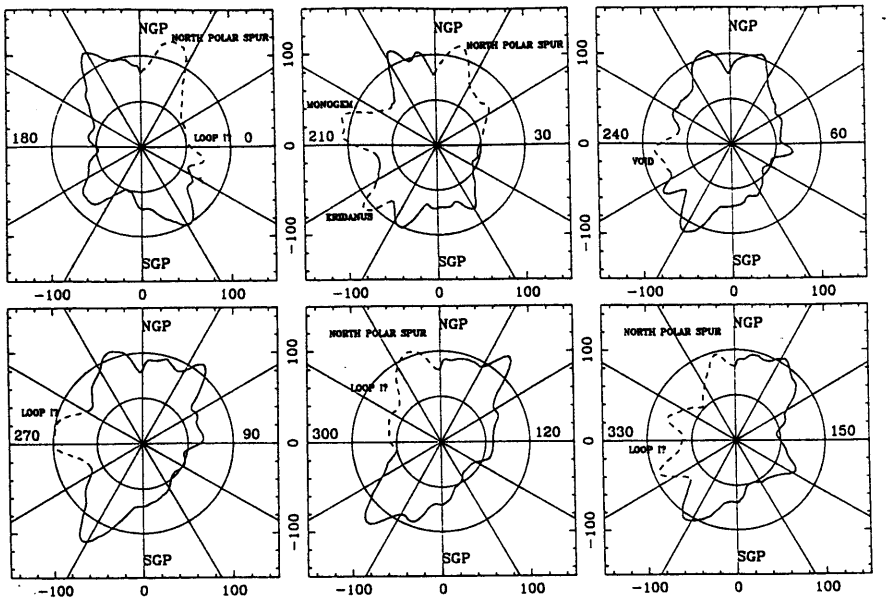

Figure 4.13: Plots of the cavity radius derived from the 0.25 keV background intensity (taken from Snowden 1997). The scale circles represent 50 pc and 100 pc. The regions which are contaminated by discrete features are dashed.

ported before, but only for localised regions on the sky. Apart from these small scale-size variations, there is also evidence in our data for three large scale features in the local cavity. Firstly, it is clear that the cavity edge approaches the Solar System much more closely in the direction of the Galactic Centre than elsewhere. It has been suggested (see Egger 1997) that this increase in column density is due to material in the Loop I Bubble, which because of its close proximity, probably interacts with the local cavity. Consequently, the view of the LISM presented here places constraints on the size and shape of this interaction region.

The second large scale feature identified in this study is the region of the cavity in the direction of the star β CMa. As discussed in Section 4.1, this direction is associated with very low column densities by almost all studies of the LISM. The column density contours of FY83 and P84 indicate that the tunnel extends across the region $200^o < l^{II} < 260^o$ out to beyond 200 pc. However, as mentioned in the last section, there is no evidence for enhancements in the soft X-ray background in this direction. This can be explained

by a drop in plasma temperature from 10^6K to $\sim 10^5$K which would result in a very low 0.25 keV flux. Interestingly, a recent study by Welsh, Crifo & Lallement (1998) has shown that there are no EUVE source detections in this direction which questions the apparent lack of absorbing material. One explanation for this result is that a significant amount of the material in this direction is highly ionised so that there are large concentrations of HeII, which, with a similar absorption cross-section to HI/HeI at EUV energies would significantly absorb EUV emission although it would not be apparent in the maps of neutral material. This view is supported by the work of (Gry, York & Vidal-Madjar 1985) who have reported the detection of substantial amounts of HII in this direction.

Finally, the third major feature of the cavity, is the region of low density material towards northern Galactic latitudes. Again, this has been reported in previous absorption studies (see Section 4.1), but generally only for regions in the second Galactic quadrant. Studies of the soft X-ray background demonstrate that the sky is brightest in this quadrant but indicate that the whole of the Galactic North pole is bright, which, according to the displacement model, suggests the cavity edge should be distant for all Northern directions (as indicated here).

4.6 Conclusion

In this chapter, we have investigated the distribution of cool material in the local ISM using HI column densities and distances from four separate samples of stellar sources. The combination of these datasets provides a high resolution picture of the material in the local ISM. By deriving a statistic which can handle the N_H bounds in our data and using spherical harmonics for smoothing, we have demonstrated that a non-spherical cavity model provides the best fit. In this model we find that n_1 is typically between 0.045 and 0.08 cm^{-2} which is in good agreement with previously published values. However, in contrast to other studies, we find that both n_2 and d_c vary with sky direction, with typical values for n_2 between 0.1 and 0.97 cm^{-3} and typical values for d_c between 29 and 280 pc. The n_2 values span a much broader range than those previously published, but the all-sky average compares very well. The non-spherical nature of the best fit model arises from essentially three separate areas of the sky; extended regions of low density gas towards

the North Galactic pole and βCMa and a region of low density gas slightly North of the Galactic centre. The general properties of these features agree well with work by W94, D95, P84 & FY83, although the high spatial resolution afforded by the large number of stellar sources in this sample provides tighter constraints on the extent of these regions. Perhaps the most significant results from this work are; (i) in some directions there is no evidence for absorbing material at all, suggesting that the low density gas extends into the halo and (ii) the detection of large scale variations in HI density over very small scale lengths. The presence of such density variations across the whole sky has profound implications for models of the local ISM particularly in terms of the scale size of gas clumps.

Chapter 5

Tracing Small-scale Fluctuations in the Soft X-ray Background

Overview

This chapter presents a study of the 10% spatial fluctuations in the 0.25 keV X-ray background intensity (scale size $\sim 20'$) which have been previously observed by the ROSAT PSPC in the direction of the Lockman Hole. The analysis is based around nine deep observations of the Lockman Hole region which samples a global minimum in the line-of-sight hydrogen column density. The non-cosmic contamination and discrete source components are subtracted and the general anti-correlation caused by variations in hydrogen column density corrected for. The properties of the residual deviations are then considered (spatial and spectral) in an attempt to identify their origin.

5.1 Introduction

Detailed studies of the X-ray background made with data from the ROSAT mission have led to rapid progress in the understanding of its true nature. This is particularly true in the 0.25 keV band. Originally, the observed anti-correlation of HI column density with 0.25 keV emission was interpreted as the effect of absorption which placed the emitting medium in the halo or outside the galaxy (see Bowyer, Field & Mack 1968; Marshall & Clark 1984). More detailed studies indicated the depth of correlation was not consistent with absorption cross sections (e.g., Burrows *et al.* 1984; McCammon *et al.* 1983) and led to the displacement model (e.g., Sanders *et al.* 1977; Snowden *et al.* 1990). In this scenario the vast majority of 0.25 keV emission was thought to originate from a local "bubble" (Cox & Reynolds 1987) of hot (10^6K) gas which had an average radius of 100 pc. The anti-correlation with N_H was interpreted as the variation in emission measure related to changes in the bubble radius and the bubble itself was thought to be formed by a local supernova remnant (See Cox & Anderson 1982). The contribution of emission originating beyond the local absorption was thought to be very small. However, the high spatial resolution data available from the ROSAT PSPC enabled shadowing experiments to be performed. These proved that significant 0.25 keV X-ray emission originates from distances beyond 300 pc and were able to place limits on the distance to various components of the emitting material (Burrows & Mendenhall 1991; Snowden *et al.* 1994a; Barber, Roberts & Warwick 1996). Consequently, the 0.25 keV background is now thought to arise from three separate components; the thermal emission from a 10^6 K plasma which fills the putative local bubble, the thermal emission from a similar temperature component associated with the Galactic halo and an extragalactic component resulting from a combination of discrete source populations.

An analysis of the ROSAT PSPC all-sky survey data with absorption columns calculated from the DIRBE corrected IRAS $100\mu m$ intensities (Schlegel, Finkbeiner & Davis 1997) have been used to obtain a global fit to this model (see Snowden *et al.* 1998).

The model has the form:

$$I_T = I_{LHB} + I_H \times exp[-\sigma(N_H, T) \times N_H] + I_{EG} \times exp[-\sigma(N_H, \alpha) \times N_H)] \qquad (5.1)$$

where I_{LHB} represents the local hot bubble component, I_H represents the isotropic halo component and I_{EG} represents the extra-galactic component. The best fit normalisations indicate that the local hot bubble component is somewhat more limited in extent than that proposed in previous models. The 0.25 keV intensity is seen to vary between 250 and $\sim$820$\times$ 10^{-6} counts s^{-1} arcmin^{-2}. The emission temperature for the material peaks at $\sim 10^6$K (assuming collisional ionization equilibrium). The combined halo and extragalactic intensity varies from $\sim$ 400$\times$ 10^{-6} counts s^{-1} arcmin^{-2} to greater than 3000 $\times$ 10^{-6} counts s^{-1} arcmin^{-2}. Using an extragalactic intensity of 400$\times$ 10^{-6} counts s^{-1} arcmin^{-2} as derived by (Barber, Roberts & Warwick 1996), this gives an un-absorbed intensity of $\sim$0-2600$\times$ 10^{-6} counts s^{-1} arcmin^{-2} for the halo component. The temperature of this material is found to peak at a value of $\sim 10^6$ K.

To study the 0.25 keV background in detail it is vital to choose a region of the sky with a high count-rate to ensure good statistics. The strong absorption of HI at these energies requires that the sky direction chosen is one with a low line of sight column density. A particularly good field for this type of study then, is the primary Lockman Hole region where the Galactic column density falls to a global minimum value of 4.5$\times$ 10^{19} atoms cm^{-2}. A preliminary study of the X-ray emission in this region (see Snowden *et al.* 1994a) used all-sky survey data to determine the foreground and background X-ray intensities in one of the first successful X-ray shadowing experiments. The results indicate a clear anti-correlation with N_H but also reveal considerable scatter about this correlation. A further study of this region (see Barber, Warwick & Snowden 1996), which used pointed observation data to provide much improved statistics, verified the existence of such scatter in the general anti-correlation between X-ray intensity and HI column density. In fact, the latter study showed that the X-ray images of this region exhibit fluctuations in X-ray intensity at the 15% level with a scale size varying from several arcminutes to half a degree. Barber, Warwick & Snowden (1996) attributed these variations to intensity enhancements caused by either; activity at the edge of an expanding supernova remnant in our immediate neighbourhood or to bubbles of hot gas within the observations line-of-sight.

This study furthers the work previously conducted on the ROSAT PSPC pointed observations of the Lockman Hole by Barber, Warwick & Snowden (1996) with the use of improved background rejection techniques, an improved treatment of source confusion (which is re-

Field	RA 2000	DEC 2000	Exposure ks	N_H 10^{19} cm^{-2}	Observation Date
1	$10^h10^m13^s$	$50^o45'00''$	15.91	9.0	12/11-13/11/91
2	$10^h10^m14^s$	$51^o45'00''$	23.99	7.5	16/4-20/11/92
3	$10^h10^m15^s$	$52^o45'00''$	14.62	6.4	14/4-10/5/92
4	$10^h10^m16^s$	$53^o45'00''$	17.33	8.4	13-14/4/92
5	$10^h10^m17^s$	$54^o45'00''$	16.81	7.4	10-12/11/92
6	$10^h10^m19^s$	$55^o45'00''$	18.99	6.8	11-15/5/92
7	$10^h01^m58^s$	$55^o40'47''$	18.84	6.7	14/11/91
8	$10^h19^m17^s$	$52^o45'00''$	13.28	7.6	25/4-1/5/93
9	$10^h27^m13^s$	$53^o29'24''$	16.08	12.8	24/4-3/5/93

Table 5.1: The directions and ROSAT observation details of the 9 pointings.

quired in order to quantify the true extent of the fluctuations) and spectral analysis of the high and low count-rate regions. The field considered covers an area of over 300 degree^2 and is centered on (l^{II}=147^o, b^{II}=54^o).

5.2 The Data

5.2.1 X-ray PSPC Data

The Lockman Hole region of the sky was observed by the ROSAT PSPC during both the all-sky survey and the pointed observation phase. To obtain the large number of counts required for this study, we use data from the pointed phase which were collected as part of the UK's Medium Deep Survey (UKMS) of the Lockman Hole region. The survey was originally proposed to study extragalactic source populations because of the low line of sight column density in this direction. The data are available in the form of a set of nine overlapping ROSAT PSPC observations in the south west corner of the primary Lockman Hole. A map of the positions of the X-ray fields is given in Figure 5.1 which also shows the distribution of HI in the region (see Section 5.2.2 for a discussion of this data). The PSPC observation details are presented in Table 5.1. The N_H value quoted is for the centre of each field of view.

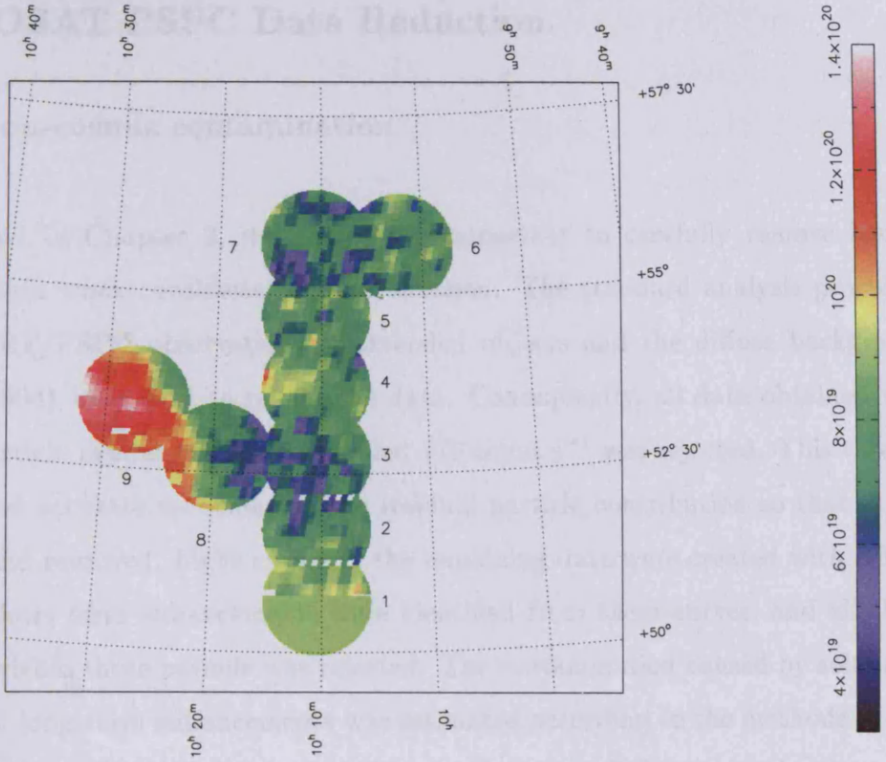

Figure 5.1: The positions of the X-ray fields and the Lockman N_H measurements (the units are atoms cm^{-2})

5.2.2 N_H Data

Due to the large amount of work completed on this area of the sky, there exists a large database of Hydrogen column density measurements (Stark *et al.* 1992; Lockman, Jahoda & McCammon 1986; Jahoda, Lockman & McCammon 1990). The N_H data used in this study were available with a resolution $> 21'$, covering the region from 10^h to 12^h18^m right ascension and 51^o to 67^o declination. The N_H in the area is relatively uniform at $(6 - 10 \times 10^{19}\ cm^{-2})$; see Figure 5.1, apart from the region around Fields 8 and 9 where it increases to $(\sim 1.2 \times 10^{20}\ cm^{-2})$.

5.3 ROSAT PSPC Data Reduction

5.3.1 Non-cosmic contamination

As discussed in Chapter 2, it is extremely important to carefully remove background contamination when considering diffuse emission. The standard analysis procedures for ROSAT XRT/PSPC observations of extended objects and the diffuse background (see Snowden 1994) were used to reduce the data. Consequently, all data obtained while the charged particle master-veto rate exceeded 170 count s^{-1} was rejected. This thresholding then allowed accurate modelling of the residual particle contribution so that it could be modelled and removed. Light curves of the remaining data were created with a 30 second interval. Short term enhancements were identified from these curves, and all the events occurring within those periods was rejected. The contamination caused by solar scattered X-rays, and long-term enhancements was estimated according to the methods of Snowden (see Snowden *et al.* 1994b for a summary paper). Maps of this contamination were then projected with the relevant spatial distribution (according to the satellite attitude data) and were subtracted from the raw data. Final images of the data were created in the seven bands (R1L through R7, see Table 5.3) described by Snowden *et al.* (1994b), which take full advantage of the spectral resolution provided by the ROSAT PSPC. Each image was also flat fielded and exposure corrected to remove the effects of vignetting and shadowing caused by the detector structure. The baseline count-rate of each map was further corrected to minimise any field-to-field variations before they were mosaiced together. This process corrects for the component of the long-term enhancement (see Chapter 2) which does not vary within the period of an individual observation. An examination of the observation light curves for each band show them to be very stable indicating that each source of contamination has been effectively identified and the majority of it removed.

5.4 The diffuse signal

In order to study the diffuse emission seen in this region of the sky, a 0.25 keV map was created which combined both the R1L and R2 band data with a pixel size of 1′x1′. The resulting image reveals point sources superimposed on the background X-ray intensity. The

area of the image associated with the sources increases rapidly with off axis angle because of the point spread function of the XRT. The removal of these sources is considered in the following section. It should be noted that we have only included data from a central circle with radius 50′ for each pointing. This restriction avoids the inaccuracies associated with the motion of the field-of-view caused by the spacecraft wobble.

5.4.1 Point source removal

To examine the diffuse emission in detail, it is necessary to remove the point sources from the data. This was achieved using the technique described below.

The raw data were convolved with a circular top hat function of radius 4′ to make the effective point spread function (PSF) of the XRT/PSPC across the ROSAT fields equal to the value observed for 50′ off axis at 0.25 keV (see Figure 5.2). This process ensures the PSF across the field-of-view isoplanatic. Bright pixels were flagged using a simple thresholding technique, where a cut-off value was selected based on a study of the count-rate distribution of the image (see Figure 5.3). That is, the threshold was chosen such that as much of the high count-rate tail was subtracted as possible. In this case, a value of 1400×10^{-6} counts s^{-1} arcmin^{-2} was used. The flagged pixels were then convolved with a 4′ top-hat to produce a first pass source mask. After the application of this source mask, the residual image was further smoothed with a 15′ diameter top-hat filter to produce a map of the diffuse emission. This diffuse image was then used as a background map for a second pass source removal in which the background was subtracted from the raw data and the above procedure repeated. The filtering was normalised to take into account the reduced number of pixels in the beam when it passed over flagged regions. This was necessary to prevent edge brightening. To prevent biasing of the data around these regions, those areas where the coverage was less than 50% were flagged as bad.

The second pass residual data formed the initial 0.25 keV background map while the convolution of a 4 arcmin top-hat filter with the flagged pixels from the second pass formed the final source mask (see Figure 5.4).

The count-rate cut off, which is the excision threshold multiplied by the source mask area

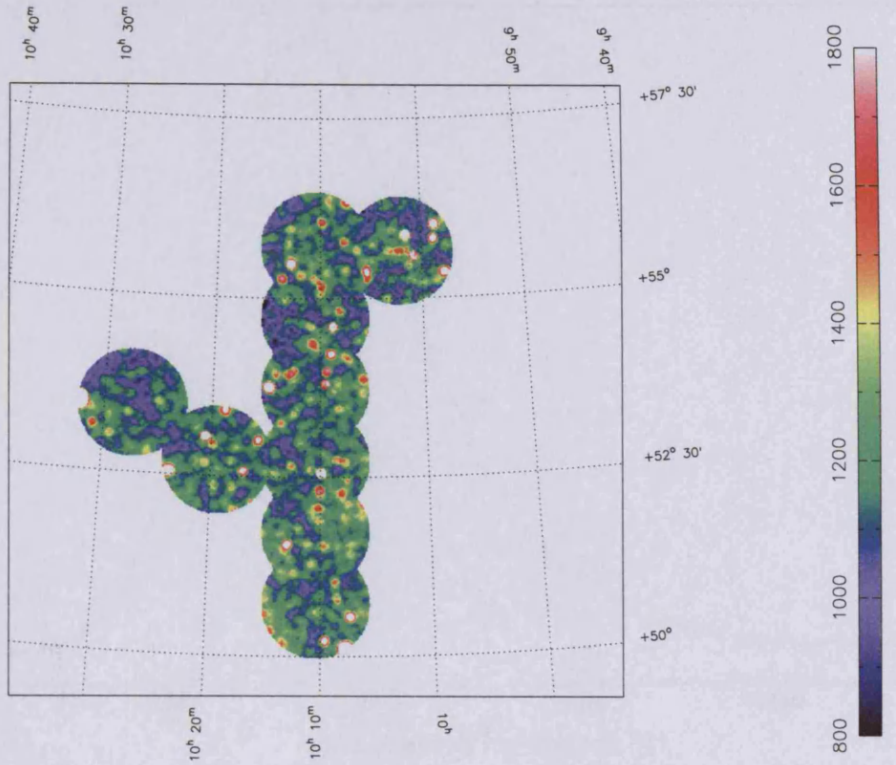

Figure 5.2: The 0.25 keV X-ray emission smoothed with a filter of radius 4′. The units are 10^{-6} count s^{-1} $arcmin^{-2}$.

is 10^{-2} counts s^{-1}. This translates to a source flux limit of 8.5×10^{-14} erg s^{-1} cm^{-2} using a source spectrum with power law index, α =1.7 and absorbing column, N_H=1×10^{20} cm^{-2}.

After the application of the source mask to the raw data, a 15′ diameter filter was used to produce a final image of the background (see Figure 5.5). There are clearly fluctuations in the 0.25 keV intensity (with a scale size of 10-30′) across most of the image. These fluctuations are continuous across the individual (and overlapping) fields which indicates that they are real and not due to artifacts of a particular observation or to background subtraction techniques. The magnitude of the fluctuations can be seen in the count-rate distribution of this image (see Figure 5.6) which reveals a distribution with an rms width of 67.5×10^{-6} counts s^{-1} $arcmin^{-2}$.

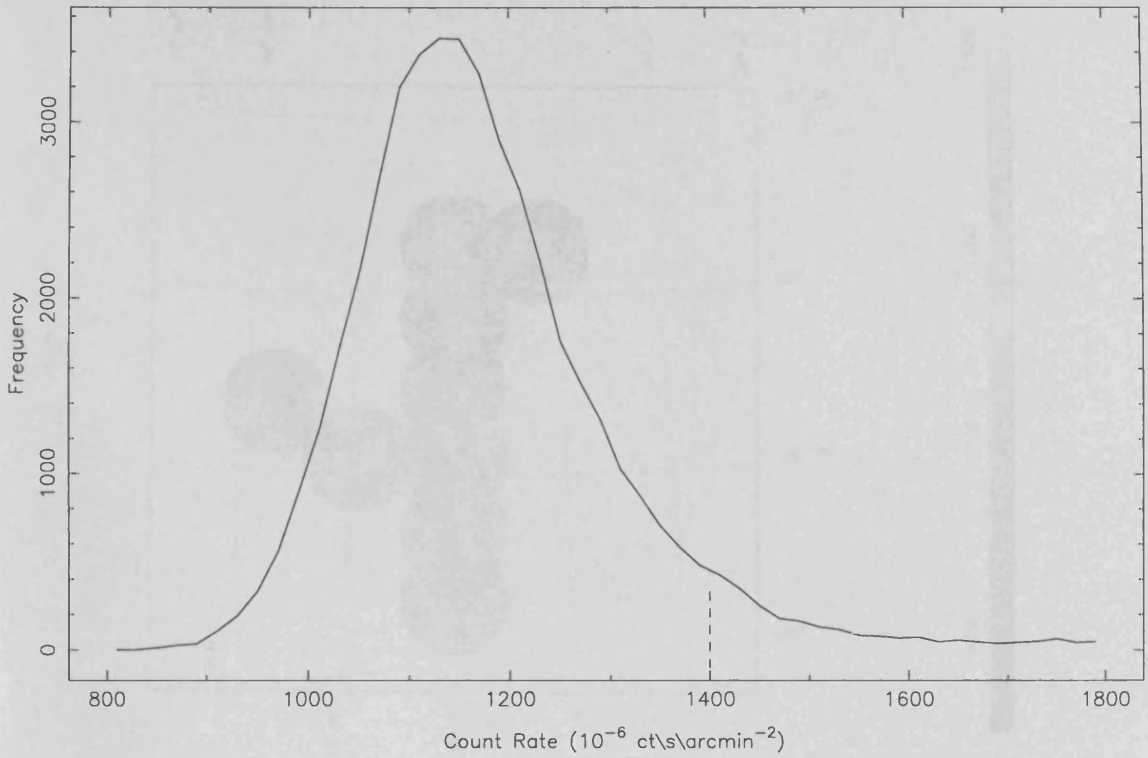

Figure 5.3: Count-rate distribution of the 0.25 keV emission

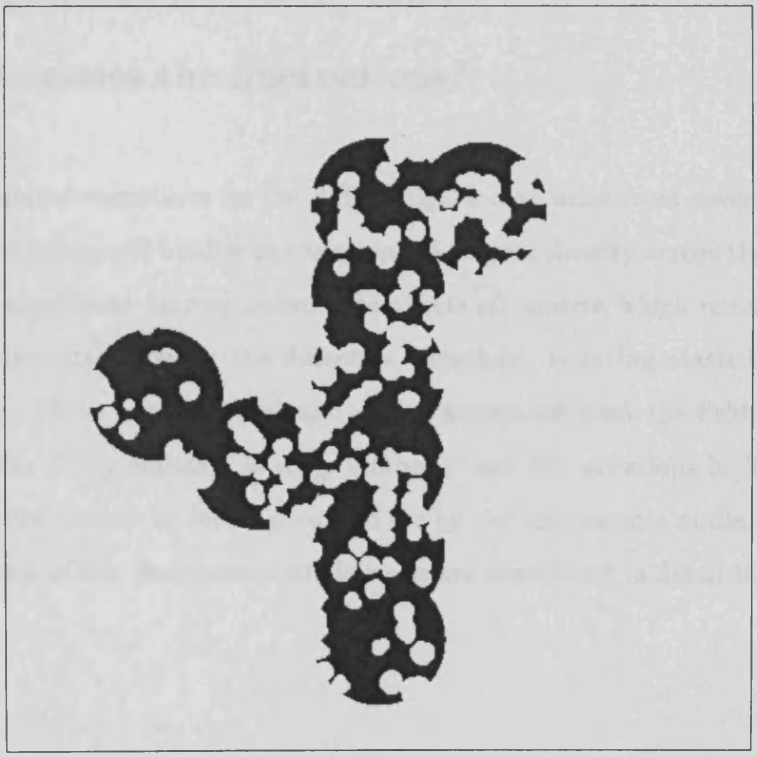

Figure 5.4: The 0.25 keV source mask

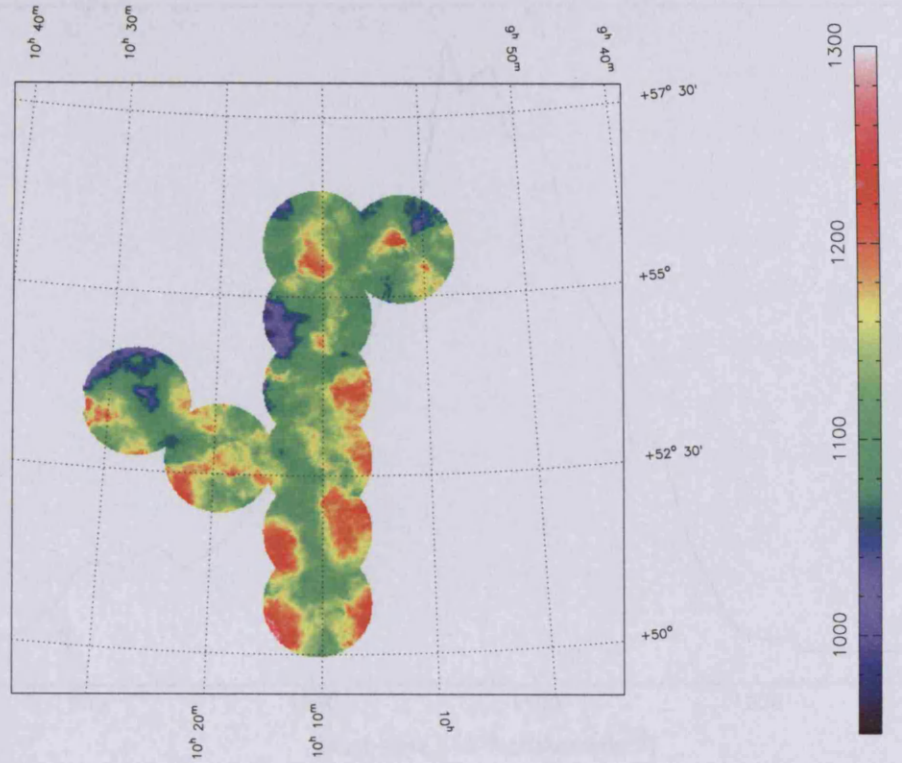

Figure 5.5: The 0.25 keV emission after source subtraction and smoothing with a filter of diameter 15′. The units are 10^{-6} count s^{-1} $arcmin^{-2}$.

5.5 What causes the fluctuations?

The observed spatial variations in the diffuse signal may arise from several effects. An important contribution will be due to variations in column density across the field of view. However, other significant factors include the effects of; sources which remain undetected because their intensity is below the detection threshold, counting statistics (which can contribute up to 2% in each sample) and errors associated with the field to field offset corrections. If the X-ray emission is truly uniform, then the variations in X-ray intensity which are observed should be fully accounted for by the components outlined above. The actual magnitudes of the dominant contributions are considered in detail in the following sections.

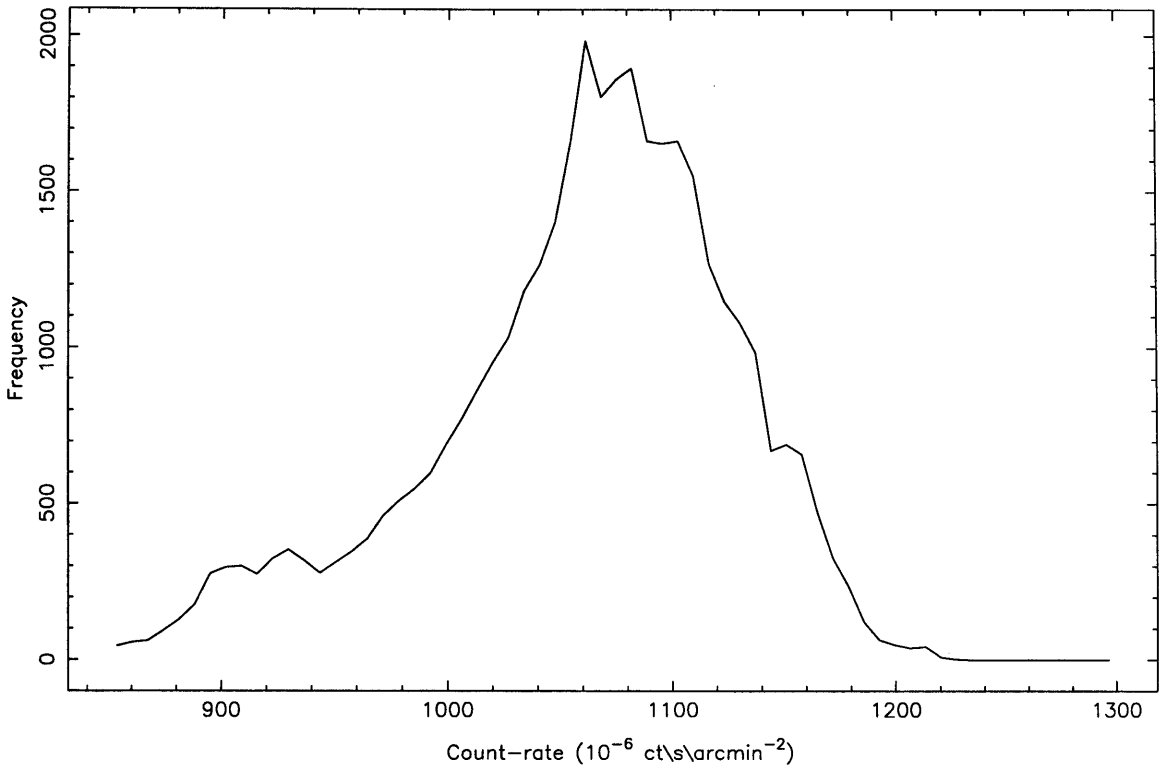

Figure 5.6: The 0.25 keV count-rate distribution of the background subtracted and smoothed image. The units are 10^{-6} count s^{-1} arcmin^{-2}.

5.6 The X-ray intensity-hydrogen column relationship

A plot of the X-ray intensity versus N_H shows the background image exhibits a fairly tight inverse correlation with the Lockman N_H map (see Figure 5.7). A fit to this data was performed with an absorption model of the form;

$$(I = I_F + I_B e^{-\sigma N_H}) \tag{5.2}$$

where, I=X-ray intensity,

I_F=Foreground intensity,

I_B=Background intensity,

and σ is the 0.25 keV band-averaged cross section derived by folding a $10^6 K$ thermal emission spectrum (Raymond and Smith 1977; Raymond 1988, 1991) through the Morrison and McCammon (1983) ISM absorption model and the PSPC effective area and spectral response.

The best fit to this model yielded a distant component of 657±148 × 10^{-6} counts s^{-1} $arcmin^{-2}$ and a foreground component of 731±68 × 10^{-6} counts s^{-1} $arcmin^{-2}$ with a $\chi^2_v \sim 1.6$ (see solid line in Figure 5.7). These values are in good agreement with the results obtained from the all-sky survey data in this region (see Snowden *et al.* 1994a) where values of 510 ±60 × 10^{-6} counts s^{-1} $arcmin^{-2}$ and 794 ±28 × 10^{-6} counts s^{-1} $arcmin^{-2}$ were obtained for the background and foreground intensities respectively (this model is plotted as a dashed line in Figure 5.7). However it should be noted that the data used here offers much better statistics than those used in the all-sky survey and demonstrate a much tighter correlation. Even so, there is still a significant scatter about the best fit model which amounts to $\sim 52 \times 10^{-6}$ $counts^{-1}$ $arcmin^{-2}$.

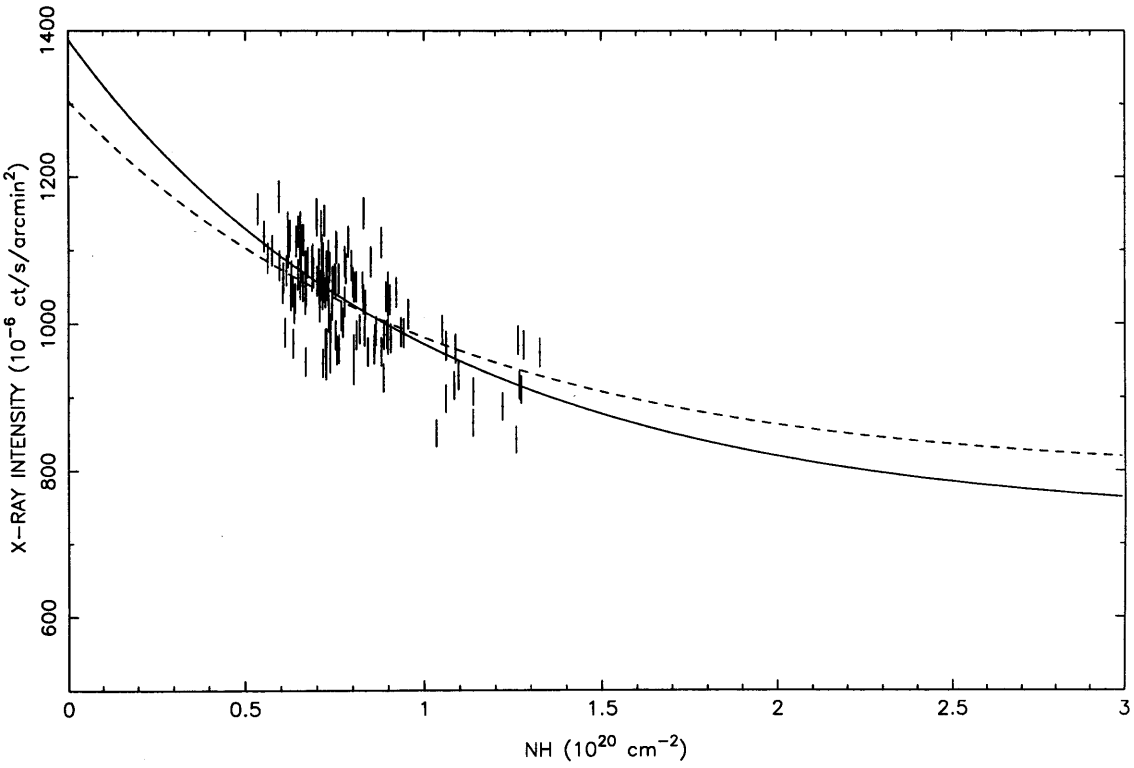

Figure 5.7: The 0.25 keV X-ray emission and N_H correlation with the best fit model. The solid line represents the best fit to the data using the model described in the text. The dashed line represents the fit obtained by Snowden *et al.* (1994a).

To correct the images for this absorption effect, the correlation was used to add back a smoothed signal derived from the first order X-ray intensity/N_H relationship:

$$CR = (N_H - 0.5 \times 10^{20}\mathrm{cm}^{-2}) \times 259 \times 10^{-6}\mathrm{counts\ s}^{-1}\mathrm{arcmin}^{-2}. \quad (5.3)$$

The absorption corrected image with 4′ smoothing is shown in Figure 5.8. The same source

detection procedure as outlined in Section 5.5.1 was then repeated on the "corrected" data with an intensity threshold of 1400×10^{-6} counts s^{-1} arcmin^{-2}. The residual background data was then convolved with a 15′ top-hat filter to identify any remaining count-rate fluctuations. The resulting image (see Figure 5.9) clearly demonstrates these remain in the data.

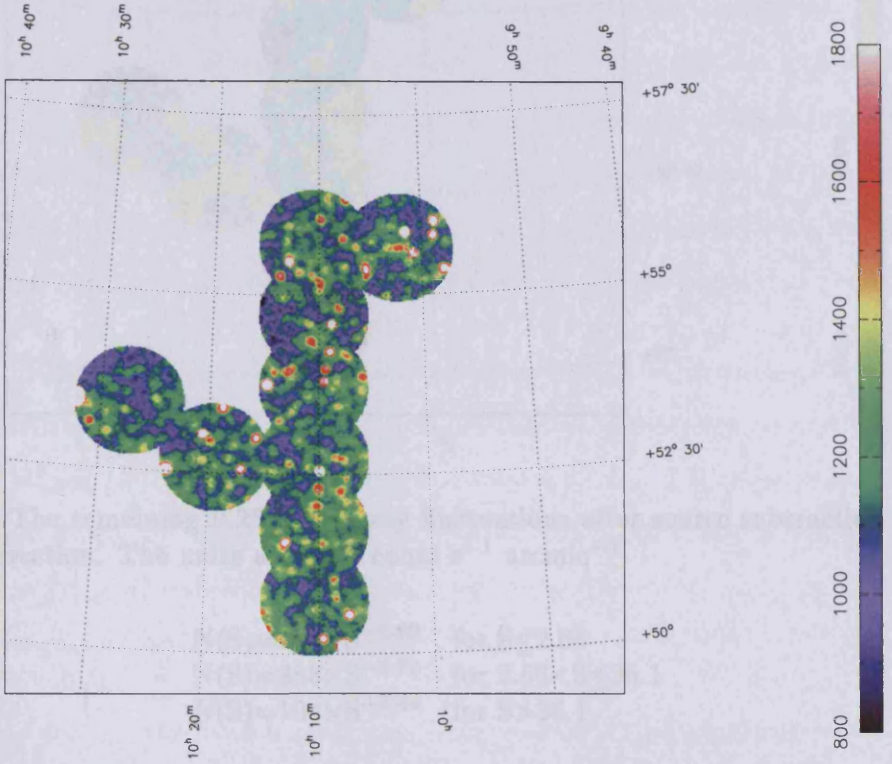

Figure 5.8: The 0.25 keV X-ray emission corrected for absorption. The units are 10^{-6} count s^{-1} arcmin^{-2}.

5.7 Simulating the effects of source confusion

To obtain an accurate estimate for the contribution of source confusion to the scatter observed in the 0.25 keV intensity, we have used a Monte-Carlo approach to simulate a typical observation. We have adopted the 0.5-2 keV logN-logS relationship derived from ROSAT observations of the Lockman Hole (Hasinger *et al.* 1993) to determine the number and strength of sources that should be observed by the PSPC/XRT system. The best estimate for the logN-logS has the following form:

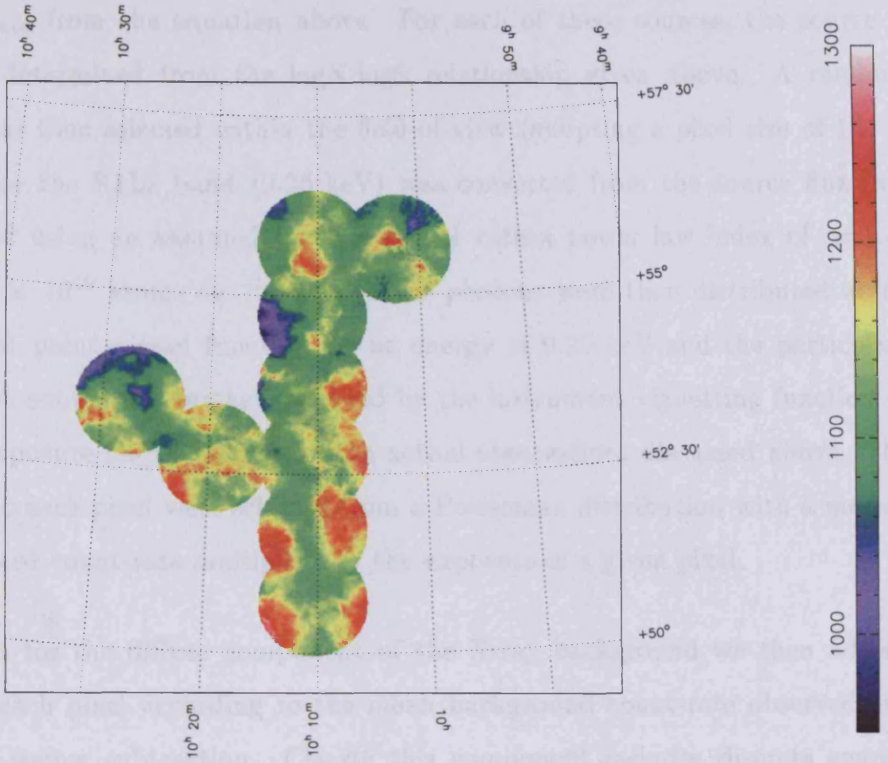

Figure 5.9: The remaining 0.25 keV X-ray fluctuations after source subtraction and absorption correction. The units are 10^{-6} count s^{-1} arcmin^{-2}.

$$N(S)=116\times S^{-1.80} \quad \text{for } S\leq 2.66$$
$$N(S)=283\times S^{-2.72} \quad \text{for } 2.66<S\leq 36.1$$
$$N(S)=104\times S^{-2.44} \quad \text{for } S>36.1$$

where N(S) is the differential source counts (i.e. dN/dS) and is equal to the number of sources per square degree observed with a flux, S (in units of 10^{-14} erg cm^{-2} s^{-1} for the 0.5-2.0 keV band), in the range S to S+dS.

Hence the total number of sources per square degree with a flux greater than S_{min} that will be observed by the PSPC can be determined by integrating the above equations to give:

$$N > S_{min}=145\times(S_{min}^{-0.80} - 2.66^{-0.80})+30.5+0.4 \quad \text{for } S_{min} \leq 2.66$$
$$N > S_{min}=165\times(S_{min}^{-1.72} - 36.1^{1.72})+0.4 \quad \text{for } 2.66<S_{min} \leq 36.1$$
$$N > S_{min}=72\times S_{min}^{-1.44} \quad \text{for } S_{min} > 36.1$$

For a given simulation, the total number of sources within the field-of-view was randomly selected from a Poissonian distribution with a mean equal to the number estimated for

a given S_{min} from the equation above. For each of these sources, the source flux was randomly determined from the logN-logS relationship given above. A random source position was then selected within the field-of-view (adopting a pixel size of 1′). The flux observed for the R1L2 band (0.25 keV) was converted from the source flux in the 0.5-2 keV band using an assumed spectral model with a power law index of α=1.4 and an N_H of 8.9×10^{19} atoms cm^{-2}. The source photons were then distributed according to the relevant point-spread function for an energy of 0.25 keV and the particular off-axis angle. Each source was further weighted by the instrument vignetting function using the detector exposure map obtained for the actual observations discussed above. The counts allocated to each pixel were selected from a Poissonian distribution with a mean equal to the estimated count-rate multiplied by the exposure of a given pixel.

To account for the diffuse component of the X-ray background we then added further counts to each pixel according to the mean background count-rate observed in the real data after source subtraction. Clearly this component includes discrete sources below the detection threshold. Again, counts were allocated to particular pixels by drawing a random value from a Poissonian distribution with a mean equal to the diffuse background count-rate multiplied by the pixel exposure.

The limiting flux in the source simulation was selected using an iterative procedure in which the value was chosen so that the total count-rate observed after subtracting sources (to the same threshold as used above) agreed with the background count-rate observed in the actual data.

A comparison of the count-rate distribution obtained from the simulation with the actual 0.25 keV image shows them to be almost identical (compare Figure 5.10, which shows the simulated count-rate distribution (including point sources) with Fig 5.3 which shows the actual count-rate distribution (including point sources)). The same source detection analysis as described in Section 5.5.1 was then completed to remove sources to the same threshold level as achieved in the real data. The source subtracted data was then smoothed with a 15′ diameter top hat filter so that the scatter associated with the sources below the detection threshold could be determined. The results from a series of such simulations are presented in the next section.

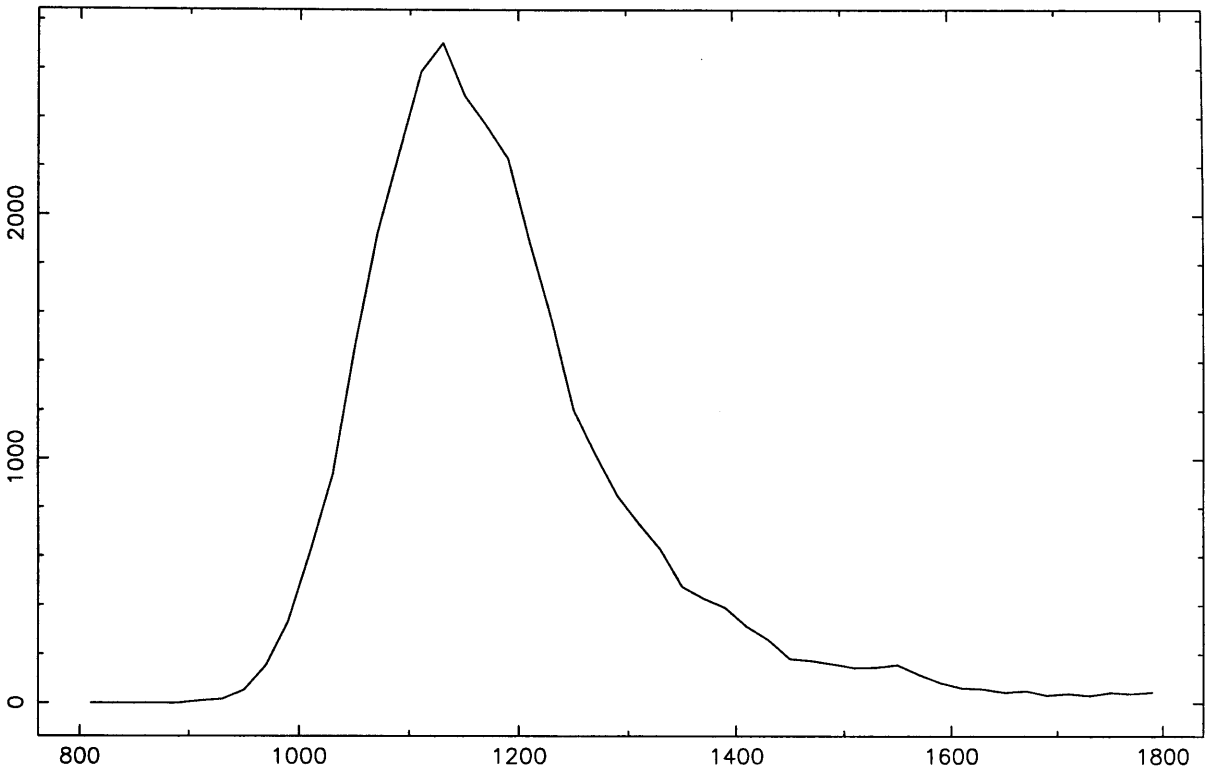

Figure 5.10: The 0.25 keV count-rate distribution for the simulated image. The units are 10^{-6} count s^{-1} arcmin^{-2}

5.8 Scatter due to errors in the field to field offsets

In order to remove the component of the long term enhancement which does not vary during an observation, the difference in intensity between overlapping fields was minimised during the data reduction process. This procedure introduces a further source of scatter because there is a counting error associated with each overlap region. This error is propagated through the other fields when reducing them to a baseline level. To determine the magnitude of this effect we have simulated the procedure by determining the number of counts in the overlap regions and drawing values from the associated Poisson distribution. These were then propagated through the remaining fields such that this error was minimised. This was achieved by initially taking Field 4 as the field to which all observations were corrected to, so reducing the number of fields through which the errors were propagated. This procedure was repeated a number of times resulting in a mean value for this effect of $15\times$ 10^{-6} counts s^{-1} arcmin^{-2}. This component was added to the spread predicted by the undetected source simulation for comparison with the fluctuation

count-rate distribution.

5.8.1 Simulation Results

The results from a series of simulations predict an average rms scatter of 37×10^{-6} counts s^{-1} arcmin^{-2} with a variance of $\sim 4\times 10^{-6}$ counts s^{-1} arcmin^{-2}. This compares to a mean scatter of $\sim 50\times 10^{-6}$ counts s^{-1} arcmin^{-2} observed in the absorption corrected data (see Figure 5.11 which shows the count-rate distributions of the simulated (red) and actual (black) data. The simulated distribution is the average obtained over many simulations). It is clear then, that for all but one of the observations, the scatter is considerably more than that expected from counting statistics and undetected sources (at least 3σ).

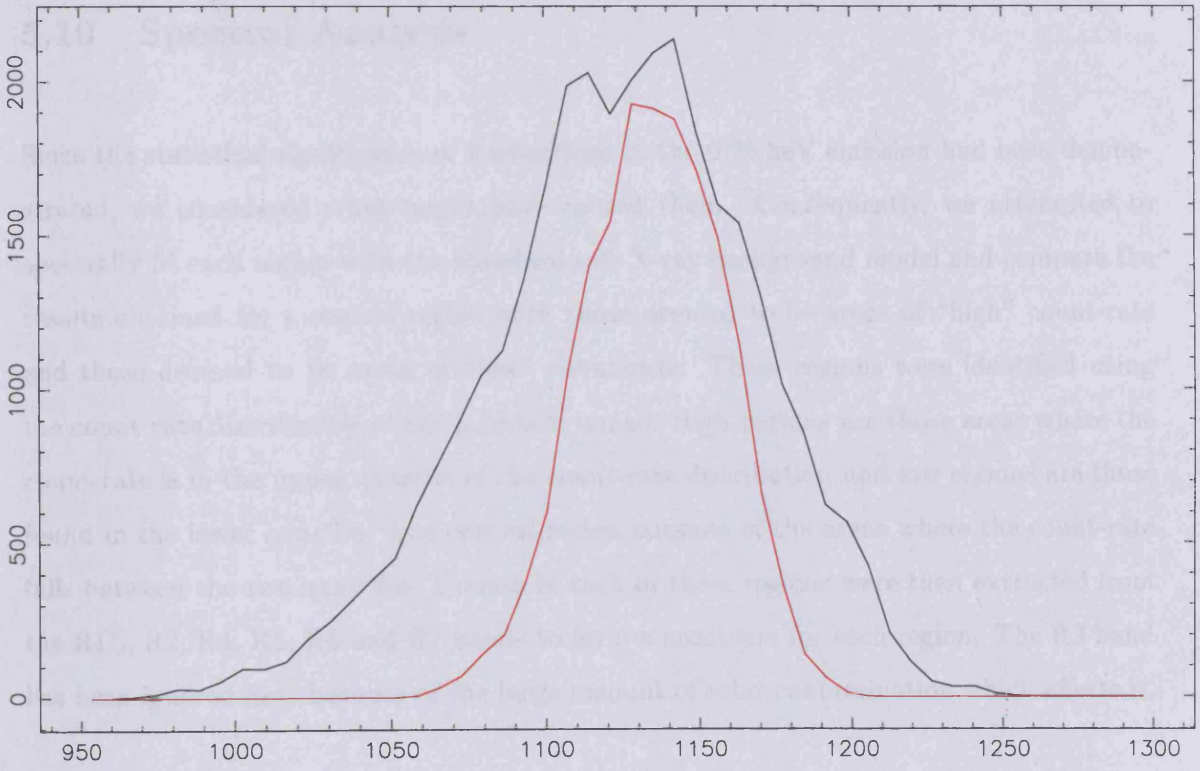

Figure 5.11: The 0.25 keV count-rate distribution of the fluctuations and the simulated count-rate distribution (in red). The simulated distribution includes undetected sources and errors in the offset procedure.

5.9 The diffuse signal at 1.5 keV

To investigate if the fluctuations are observed at higher energies we have also considered the emission from the 1.5 keV band. The above procedure was repeated for the 1.5 keV band (the R4-R7 bands) and in each case the fluctuations were observed to be at the same level as expected purely from discrete sources below the detection threshold. In addition, the fluctuations which were observed in these bands did not coincide with those seen in the 0.25 keV band, so unless there is a source population whose spectra diminish rapidly at 0.25 keV, then the fluctuations observed in the 0.25 keV band cannot be associated with sources beneath the detection threshold.

5.10 Spectral Analysis

Since the statistical significance of fluctuations in the 0.25 keV emission had been demonstrated, we considered what might have caused them. Consequently, we attempted to spectrally fit each region with the standard soft X-ray background model and compare the results obtained for a control region with those deemed to be areas of "high" count-rate and those deemed to be areas of "low" count-rate. These regions were identified using the count-rate distribution of the 0.25 keV image. High regions are those areas where the count-rate is in the upper quartile of the count-rate distribution and low regions are those found in the lower quartile. The control region consists of the areas where the count-rate falls between the two quartiles. Counts in each of these regions were then extracted from the R1L, R2, R4, R5, R6 and R7 bands to form a spectrum for each region. The R3 band has been ignored here because of the large amount of solar contamination which affects it.

5.11 Spectral Fitting

The data were fit with a spectral model which included components for the extragalactic flux, the Galactic halo and the Local Bubble emission. For the halo emission we used a two temperature plasma model (as suggested by Snowden *et al.* 1998) instead of the more typical single temperature approach which requires a relatively high ($10^{6.3}$ K) temperature

to fit both the 0.25 keV and 0.75 keV thermal emission simultaneously. The argument for two temperature components in the halo is backed up by a study of the structure of halo emission seen in the different bands of the all-sky survey which indicate clumping at different scale sizes for the 0.25 keV and 0.75 keV emission. We adopted the Raymond-Smith model in the XSPEC spectral fitting package to determine the emission for this component. The foreground component is modelled with a 10^6 K Raymond-Smith plasma model Raymond & Smith (1977). The extragalactic component was modelled with a power law slope of $\alpha = 1.4$. The N_H was frozen at a value of $8.9\times\ 10^{19}$ atoms cm^{-2} and the local thermal component was modelled using a gas of temperature $10^6 K$.

Initially, fits were performed on data from the control region of the 0.25 keV image. The temperatures of the halo components and the local components were frozen as was the power law index (see Table 5.2). A χ^2 fit was then performed on the four remaining parameters. The six spectral bins provided two degrees of freedom. The best fit results appear in Table 5.2.

Adopting the best fit model we then considered the spectra from the high and low fluctuation regions of the image. For the fits to these regions we used the same spectral model and initially froze the normalisations to half those obtained for the control region and included a systematic error of 1.5%. We investigated the fit obtained by allowing various parameters to float. The best χ^2 values obtained were for variations in N_H and variations in the normalisation of the lower temperature halo component. The results are shown in Table 5.4. Clearly, for the low fluctuation region there is evidence that spectral variation from the control region is a result of differential absorption across the field of view. However for the high count-rate region, the best fit is obtained for a model in which the normalisation of the halo component varies across the field of view.

5.12 Discussion

The preliminary results suggest that the bright fluctuations are probably the result of variations in the emission measure of the Galactic halo component compared to the field average. However, there is also evidence that to some degree, the variation may be caused

Parameter	Value	90% error range	Units
T1	0.22		keV
N1	8.4	8.2-8.7	
T2	0.09		keV
N2	19.9	18.5-21.6	
T3	0.09		keV
N3	8.4	7.8-9.0	
α	1.4		
N4	10.3		$keV\ cm^{-2}\ s^{-1}\ sr^{-1}\ keV^{-1}$
N_H	8.9		10^{19} atoms cm^{-2}
χ^2	1.6		

Table 5.2: The spectral fitting results obtained for the control region of the 0.25 keV image.

Region	Normalisation	Confidence Interval 90%	χ^2
Low	8.6	7.9-9.3	1.8
High	11.5	10.8-12.3	1.2

Region	N_H 10^{19}atoms cm^{-2}	Confidence Interval 90%	χ^2
Low	10.2	9.5-11.0	1.6
High	7.7	7.1-8.3	1.5

Table 5.3: The best fits obtained for the low and high count-rate regions with the normalisation (top) and N_H (bottom) allowed to vary.

by differential absorption across the field of view. In either case, 10% variations in 0.25 keV intensity (with a scale size of $\sim 20'$) are apparent and need to be explained. Further analysis of these fluctuations is deferred to the next chapter where these results are combined with observations made in other sky directions.

Chapter 6

Further analysis of small scale spatial fluctuations in the 0.25keV X-ray background

Overview

This chapter presents a further study of the spatial fluctuations seen in some ROSAT PSPC images of the 0.25keV X-ray background. The work follows on from the study presented in the previous chapter with the inclusion of an extra six fields from the ROSAT pointed observation survey. The fields selected each have an exposure of over 20000 seconds to ensure reasonable statistics and were chosen to sample a range of HI column densities and sky directions. In a similar analysis to that described in Chapter 5, the non-cosmic background is removed and the spatial distributions of the residual deviations are investigated.

6.1 Introduction

The study presented in Chapter 5 considered the fluctuations seen in one region of the sky and a spectral analysis of the data indicated that they were possibly caused by variations in the emission measure of halo gas or differential absorption across the field-of-view. In this chapter we consider fields from various other sky directions to investigate whether the fluctuations are observed globally, and if so, to what extent they are due to variations in emission from within the local interstellar medium, variations in the halo emission or absorption along the line-of-sight.

6.2 The Fields

The details of the fields selected for this study are presented in Table 6.1. The N_H value is that quoted by Stark *et al.* (1992) for each sky direction. However, it should be noted that these data have a resolution of about 1 degree^2 and the values quoted in the table represent an interpolated value, not a field averaged value. The characteristics of each field are discussed in detail below.

Field	Name	RA (2000)	DEC (2000)	l^{II}	b^{II}	ROR	N_H 10^{20} *atoms* cm^{-2}
1	Plane	$19^h30^m28^s$	$18°52'12''$	54	0	500042	93.5
2	Q0000	$00^h03^m23^s$	$-26°03'36''$	36	-79	700467	1.83
3	GSGP4	$00^h57^m28^s$	$-27°38'24''$	234	-89	701223	1.95
4	NEP	$17^h57^m55^s$	$66°22'47''$	96	30	170075	5.10
5	WFCNEP	$17^h59^m59^s$	$66°33'35''$	96	30	100378	5.23
6	QSF3	$03^h42^m11^s$	$-44°07'48''$	251	-52	900632	1.70

Table 6.1: The observation details of the six fields.

Field1

This region was chosen because it is towards the plane of the Galaxy and consequently samples a very large HI column density. The presence of fluctuations in this image would give an upper limit to the fluctuation component originating from the local bubble as there will be very few counts originating beyond the N_H. However, the high absorption

Field	Year	Day	Exposure Ksecs	Detector	Gain
Plane	1991	101	20	PSPCB	High
Q0000	1991	330	37	PSPCB	Low
GSGP4	1992	185	49	PSPCB	Low
NEP	1991	214	41	PSPCB	High
WFCNEP	1990	173	51	PSPCC	High
QSF3	1993	216	52	PSPCB	Low

Table 6.2: The date and PSPC operating mode for the six observations.

also means there are very few counts (both from the diminished external component and reduced local bubble extent).

Field2

Field 2 is named the Q0000 field and is an observation of a quasar field. It samples a region of reasonably low HI column density at a very high Galactic latitude. Consequently the data from this region of the sky should contain a significant contribution from the halo and extragalactic components of the X-ray background.

Field3

Field 3 is known as the GSGP Field as it is in the direction of the Galactic pole. Well away from the plane it samples a low HI column density and should contain a large extragalactic component. However, because it is in the direction of the Galactic pole, the contribution from the halo will be reduced because of the relatively small path length.

Field4

The NEP Field is a region which is adjacent to the WFC-NEP field and consequently samples approximately the same HI column density. The close proximity of the two fields provides an opportunity to check for consistency in the magnitude of the fluctuations with sky direction. This should also indicate to what degree background subtraction techniques contribute to any spatial fluctuations.

Field5

This is the WFCNEP field and samples an area of the sky near the North Ecliptic Pole. At a low Galactic latitude, this field samples a relatively high HI column density and consequently the counts should be dominated by the local bubble contribution. Any fluctuations seen in this image would indicate that they originate almost entirely from within the Local Hot Bubble.

Field6

Field 6 is known as the QSF3 field and is in the direction of the Galactic anti-centre. Again it is at a relatively high latitude and samples a reasonably low HI column density. The emission in this field should also contain substantial counts from the halo.

The position of these fields in Galactic coordinates are indicated in Figure 6.1.

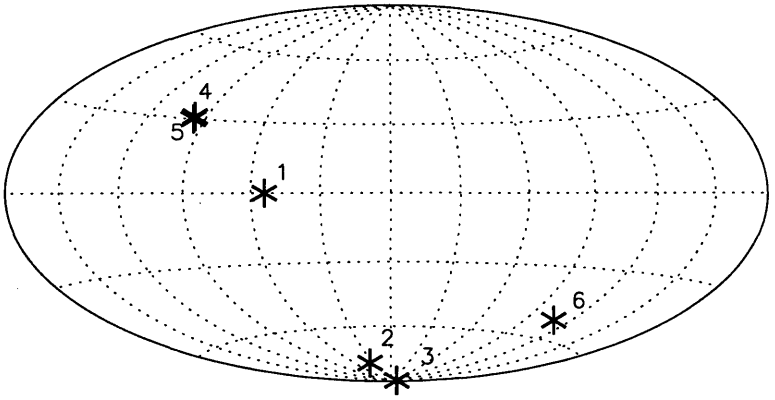

Figure 6.1: The location of the six fields in Galactic coordinates. The plot is 0 centered with Galactic longitude increasing to the left.

6.3 Background Subtraction

The exposures and ROSAT PSPC operation modes are given in Table 6.2 for each of the observations. An almost identical data reduction procedure to that described in the previous chapter was carried out on each of the fields. The data were binned into the same seven spectral bins and each count map was flat fielded. Periods of data were rejected if either the master-veto count-rate was above 170 counts per second or there was an obvious

Field	LTE	Solar	After-Pulse	Particle	Total
Plane	14333	37577	0.0	2777	180537
Q0000	28198	908	3127	3529	296390
GSGP4	11503	3661	6834	5369	289186
NEP	31725	124383	1986	5528	476225
WFCNEP	62399	19444	0.0	7644	341763
QSF3	94065	12209	5229	5370	432765

Table 6.3: The total counts attributed to each background component in the six fields.

short-term enhancement(STE) evident in the light curve. The solar contamination was calculated and removed along with the particle, long-term enhancement and after-pulse components. The counts associated with each of these contributions are listed in Table 6.3.

Again, it is particularly important to note that the value derived for the long-term enhancement does not take into account the non-time varying component. Consequently, the value derived for the cosmic intensity may be in some error. This will not affect a comparison of areas across an image but may hinder (and reduce the quality of) fits to X-ray background models. In addition, the determination of the higher order components of the LTE polynomial are significantly affected by noise in the data. This means that in some cases it is impossible to determine if a high order term is significant to the fit. An incorrect choice can result in the inclusion (or exclusion) of an LTE component containing up to 5% of the counts in an image. Since different polynomials are used to model different bands, this can seriously affect spectral fitting. The majority of this affect can be accounted for by adding suitable systematic errors to the data.

In general, the datasets were relatively clean with few time periods rejected. However, the QSF3 field and the WFCNEP field, which were both significantly contaminated by solar scattered X-rays, were not particularly well modelled and it is expected that there still remains significant contamination in the lower three bands (R1/R1L, R2 and R4). However, this contamination is distributed evenly across the field (apart from a slight gradient in the solar component) so will not affect a spatial/count-rate study of the fluctuations.

However, a spectral analysis for all areas of the image will be affected.

6.4 The 0.25 keV Count-rate Images

The 0.25 keV count-rate images were created for each of the observations by combining the R1 (or R1L if the PSPC was operated in the low gain mode during the observation) and R2 background subtracted count maps and dividing by the flat-fielded exposure maps (see Figure 6.2).

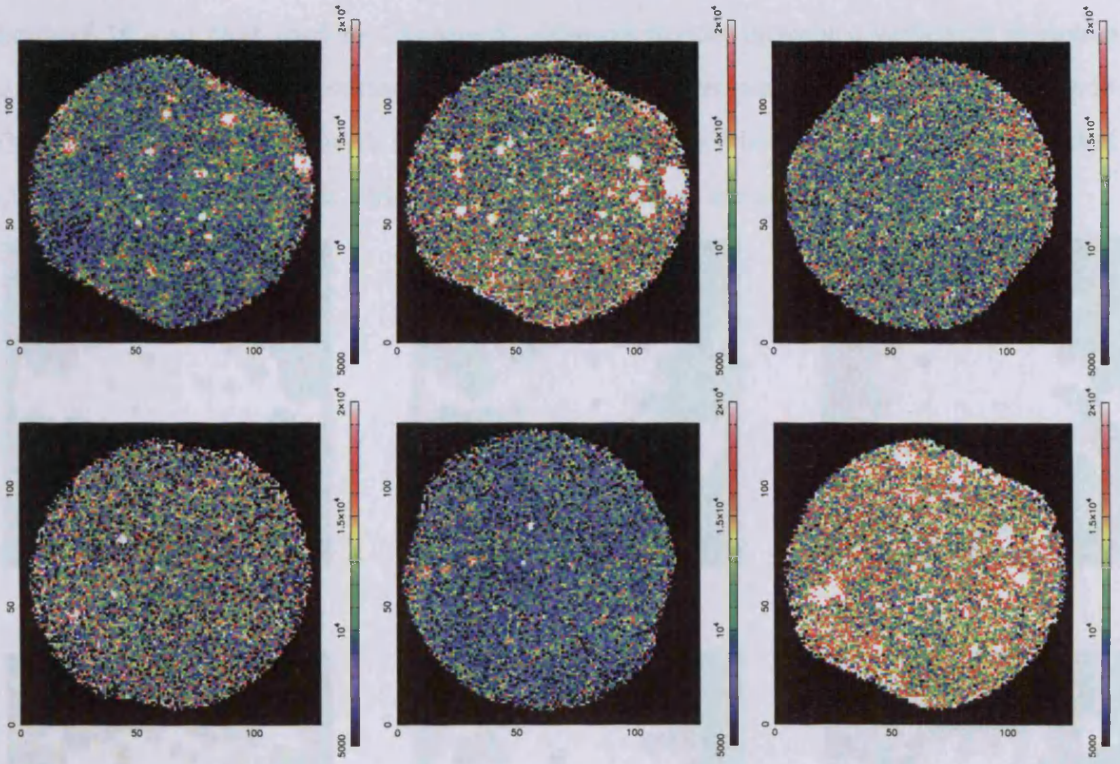

Figure 6.2: The background subtracted 0.25keV count-rate images obtained for the six fields. The units are 10^{-6} counts s^{-1} arcmin^{-2}. From left to right and top to bottom the fields are in the order 1-6.

6.5 Removing the Discrete Sources

For this analysis, in which the observations have a relatively small field of view, it is essential that no more counts (or image area) than absolutely necessary are lost due to source subtraction. Consequently, we have adopted an adaptive source removal technique

in which only the area corresponding to the 90% point spread function (PSF) at a particular energy and off-axis angle is removed. To achieve this we used the Detect algorithm provided with the standard diffuse analysis package (see Snowden *et al.* 1994b). This procedure adopts a sliding box technique to scan the image for sources. The algorithm selects the 90% point spread function for a particular band energy and off-axis angle and integrates the counts within the region. A simple thresholding technique was applied to determine whether or not the count-rate constituted a source detection and if so, a circular region with a radius equal to that of the 90% point-spread function was flagged as bad. This method reduces the number of pixels lost for sources detected in the inner ring by a factor of 16 over that used in Chapter 5, although it does introduce variations in source sensitivity across the observation field of view. The source mask for each field is shown in Figure 6.3. A comparison with the corresponding 0.25keV image (Figure 6.2) shows that all the discrete components which are visually apparent are successfully flagged.

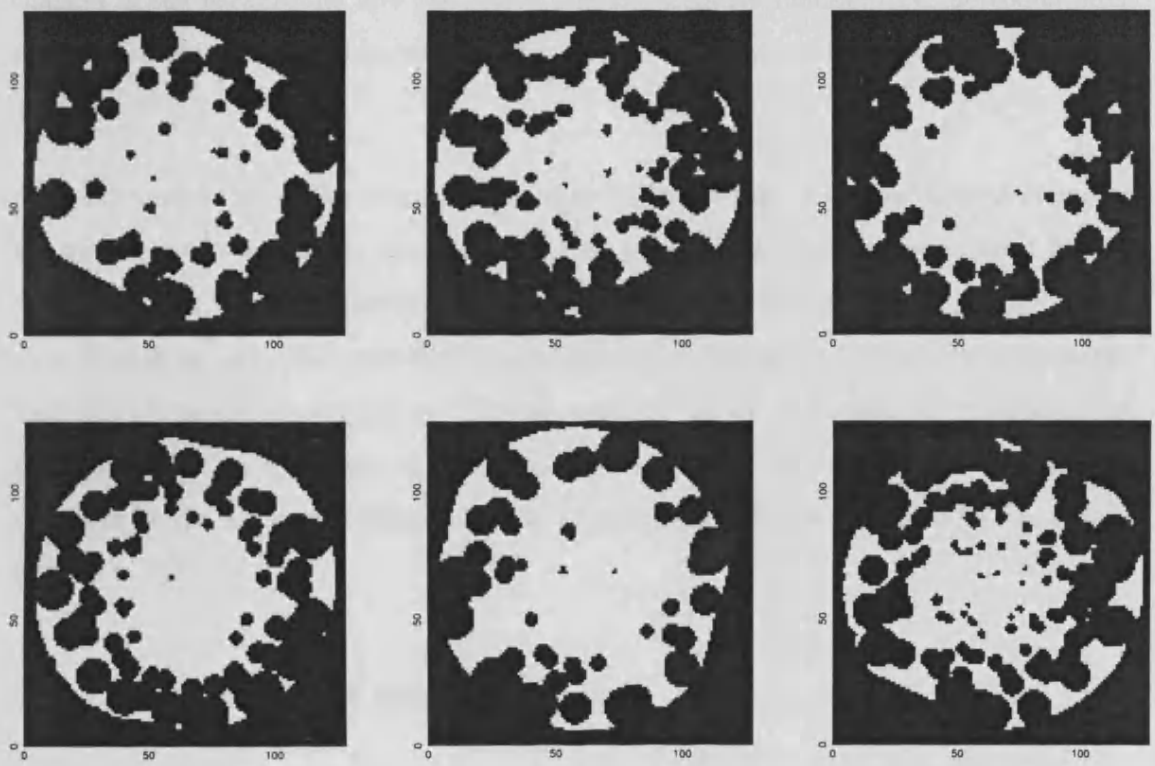

Figure 6.3: The source masks determined for each field. From left to right and top to bottom the fields are in the order 1-6.

The count-rate cut-off and its equivalent source flux is shown along with the source significance in Table 6.4. The background counts are taken from an annulus formed between 1.5 and 2.5 times the 90% point-spread function radius. The flux threshold is that for an

Field	Name	Count-rate Cut $count\,s^{-1}$	Flux Threshold $erg\ s^{-1}\ cm^{-2}$	Significance On-axis	Significance Edge of fov
1	Plane	3×10^{-3}	2.1×10^{-13}	8	6
2	Q0000	3×10^{-3}	4.1×10^{-14}	8	6
3	GSGP4	3×10^{-3}	4.1×10^{-14}	9	5
4	NEP	3×10^{-3}	4.2×10^{-13}	10	5
5	WFCNEP	3×10^{-3}	1.8×10^{-14}	8	6
6	QSF3	3×10^{-3}	3.9×10^{-14}	9	4

Table 6.4: The source detection threshold and corresponding significance for the six fields.

unabsorbed source which is determined using a power law with photon index 2.0 and the HI column density given in Table 6.1. The significance varies across the image because of changes in the background and the size of the point spread function (i.e. detection box) so values are quoted for an average background both on-axis and at the edge of the field of view.

After the application of this source mask to the 0.25keV image, a circular filter of diameter 15′ was used to smooth the data. During this process the filter was normalised by the number of "live" pixels it passed over. Regions where the filter had 50% coverage or less were flagged as bad. The resulting images appear in Figure 6.4. Clearly, it is apparent that there is significant scatter in 0.25 keV intensity across each image with evidence for fluctuations with a scale size of ∼20′. The magnitude of the scatter in these images is indicated by the count-rate distribution of the data which is shown for each field in Figure 6.5.

6.6 The effects of absorption

6.6.1 The IRAS Data

It is to be expected that a fraction of the scatter seen in the 0.25keV band images arises from the variation in HI column density across the observation field of view. Unfortunately, high resolution N_H data of the type used for the analysis of the Lockman Hole (see Chapter

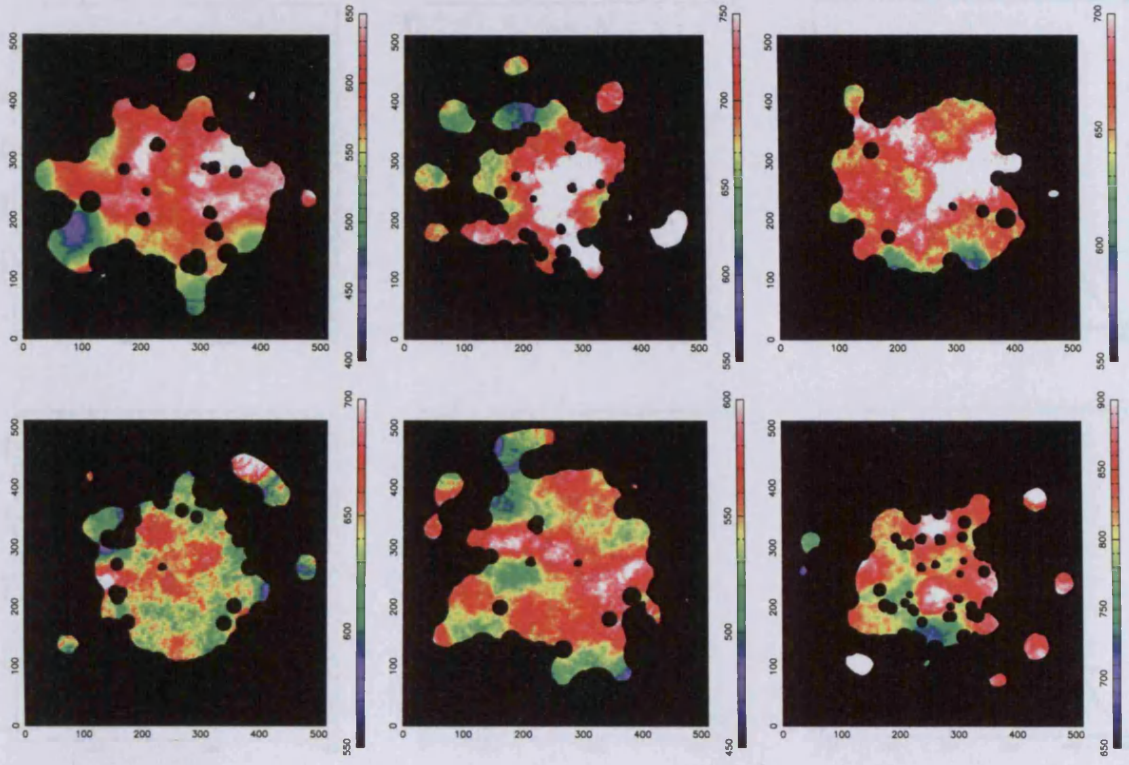

Figure 6.4: The 0.25keV count-rate maps with sources removed and after smoothing with a circular filter of diameter 15′. The units are 10^{-6} counts s^{-1} $arcmin^{-2}$.

5) are not available for these individual fields. However IRAS $100\mu m$ maps do exist for the sky directions of the six fields at a spatial resolution of 1.5′ and can be used as a tracer for N_H. The relationship between 100μ intensity and N_H is well studied (see Boulanger & Perault 1988) and in general, a 100μ intensity of 1 $MJysr^{-1}$ is equivalent to 1.4×10^{20} atoms cm^{-2}. However, this relationship is not precise because the IRAS data suffer from uncertain gain at low spatial frequencies and poorly determined zero points. In addition, the conversion can be affected by variations in dust temperature. These affects have been corrected for in some studies (i.e. Snowden *et al.* 1998) by using the well calibrated DIRBE data (Schlegel, Finkbeiner & Davis 1997) to replace the low frequency components and using the DIRBE 100 μm, 140 μm, 240 μm data to determine temperature variations and to correct the 100 μm map to a constant reference temperature. However, these data were not available at the time of this study so we have ignored these effects. IRAS maps for the six fields in this study appear in Figure 6.6. We have performed a source search on each of the IRAS fields using the 100 μm count-rate distribution to determine a source threshold. All pixels within a circle of radius 4′ centered on a pixel above threshold are flagged as bad. Both the X-ray and the IRAS images are compressed to a pixel size of 1′.

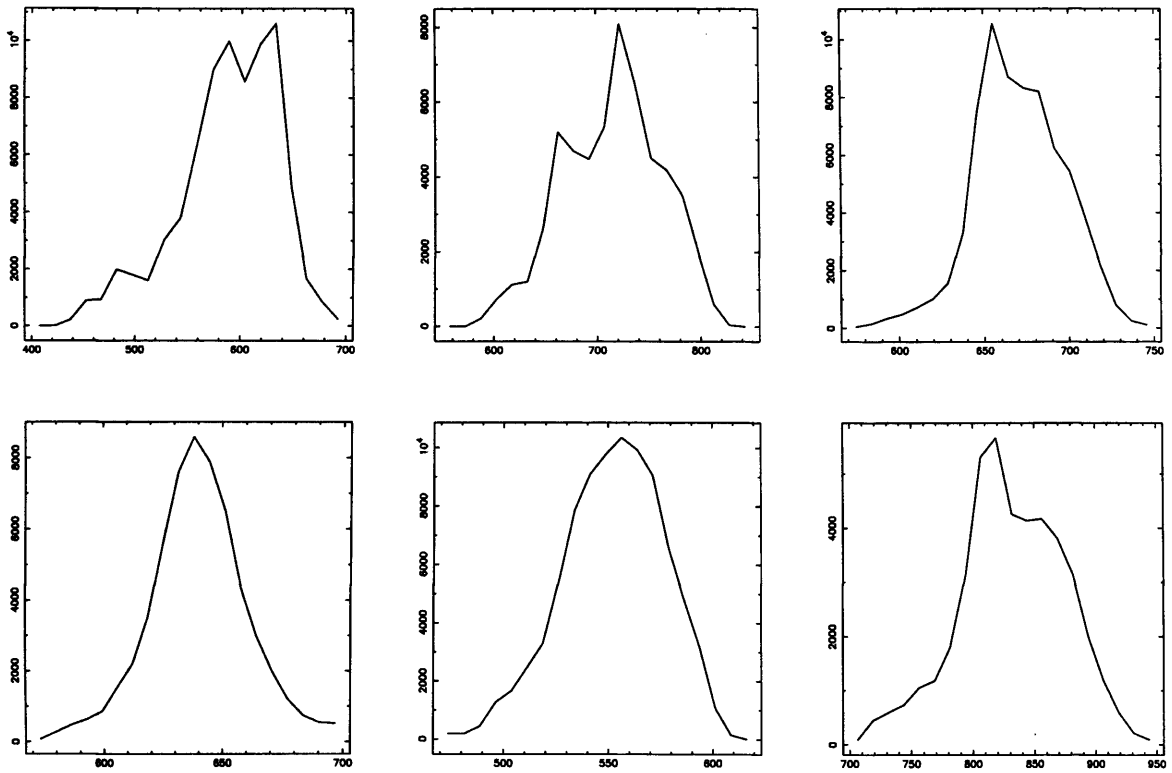

Figure 6.5: The 0.25keV count-rate distributions for the six fields after source subtraction. From top to bottom and left to right, the fields are: GSGP,Q0000,NEP,PLANE,WFCNEP & QSF3. The units are 10^{-6} counts s^{-1} arcmin^{-2}.

The resulting correlation between the 0.25keV intensity and the IRAS intensity are given for each of the fields in Figures 6.7-6.11. The plot to the left in each figure shows the 0.25keV intensity and the N_H value for 4′ pixels. The plot to the right shows the correlation obtained with the data sorted into 20 bins according to the IRAS intensity. The curve represents the best fit to the equation:

$$(I = I_F + I_B e^{-\sigma N_H}) \tag{6.1}$$

where, I=X-ray intensity,

I_F=Foreground intensity,

I_B=Background intensity,

and σ is the 0.25 keV band-averaged cross section derived by folding a $10^6 K$ thermal emission spectrum (Raymond & Smith 1977; Raymond 1988, 1991) through the Morrison

& McCammon (1983) ISM absorption model and the PSPC effective area and spectral response.

Using these fits, it is possible to correct for the effects of absorption across the image. A linear fit to the variation in X-ray intensity as a function of the IRAS 100μ intensity was used to "add" back the X-ray intensity lost due to absorption. The reduced spread seen in the corrected 0.25keV images are listed in Table 6.5.

For all of the fields there is clearly a strong correlation between 0.25keV X-ray intensity and the IRAS intensity. However in all of the fields there is still a degree of spread around this correlation indicating that the fluctuations seen in the images of the 0.25 keV background arise from more than the effects of absorption.

6.7 Simulating the effects of source confusion

As discussed in Chapter five, a further component which contributes to the scatter seen in the data is that due to source confusion. This occurs where sources below the source detection threshold are not identified as discrete sources. The actual contribution of this component is dependent on the source detection threshold (and consequently N_H) and so varies from image to image. To determine the contribution of this component to the total scatter seen in Figure 6.5 as accurately as possible, we have adopted the same source simulation technique as described in Chapter 5. This process uses the Log-N-Log-S source count distribution from Hasinger *et al.* (1993) to simulate an image for the particular background intensity and N_H of each field. Again, the flux predicted from the logN-logS for a given source is converted to a 0.25 keV flux using a spectral model with a power law index of 1.7 and the N_H of the given field. The simulated images are then source searched using the same detection algorithm as described above. The resulting count-rate distribution obtained after the removal of the sources represents the spread to be expected from source confusion. This process was repeated for a large number of samples (1000) and the results are given in Table 6.5 along with the count-rate spread observed in the actual field and the spread remaining after correction for absorption. In Table 6.5 the fifth column gives the average scatter observed for all the simulations, while the sixth column

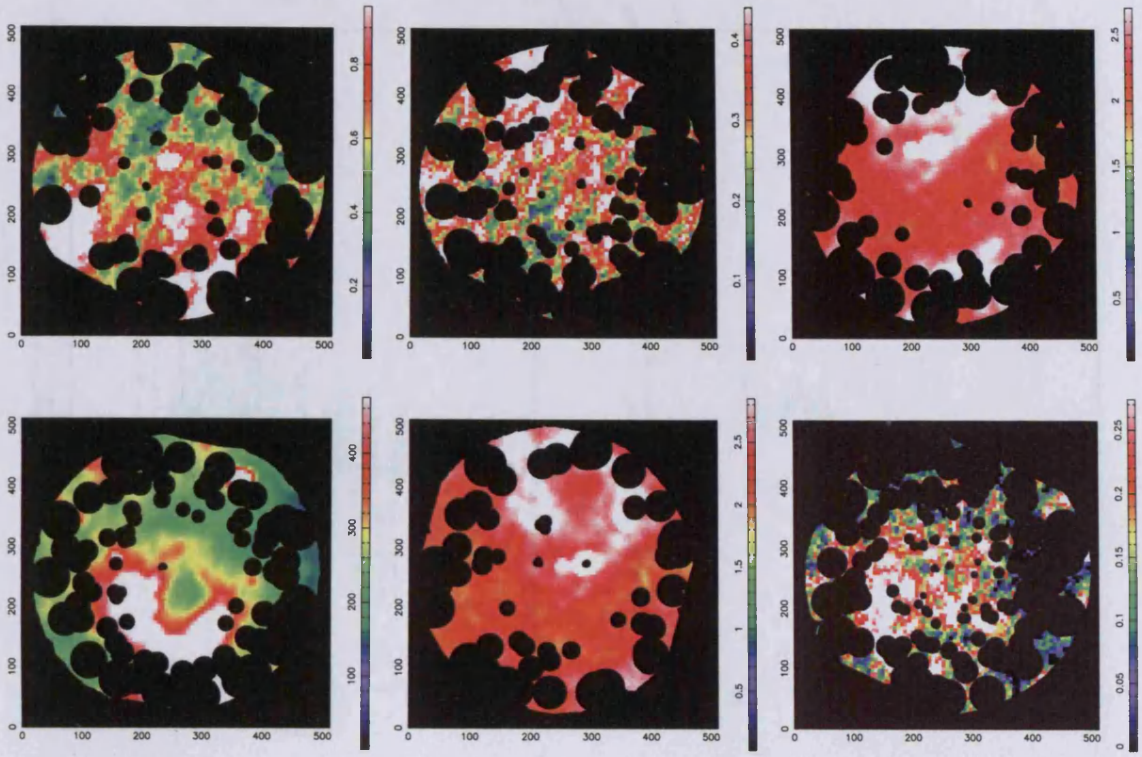

Figure 6.6: The IRAS maps for the six fields. The intensity is in units of MJy sr^{-1}.

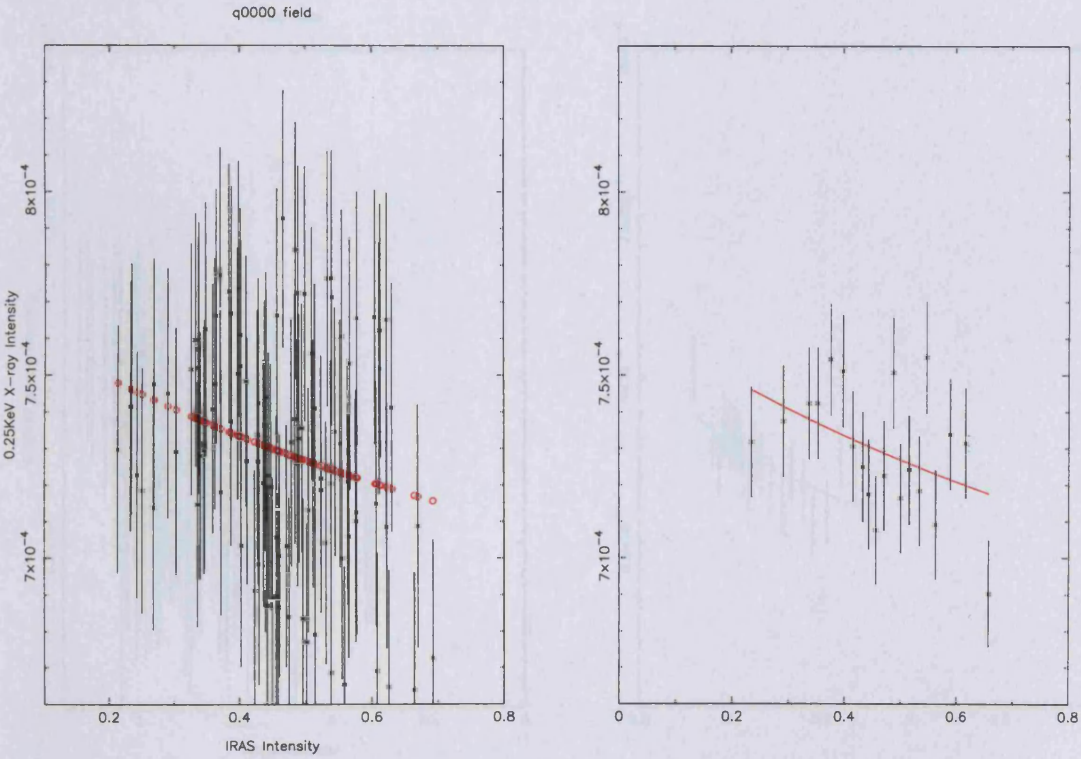

Figure 6.7: The correlation between 0.25 kev X-ray intensity (units are 10^{-6} counts s^{-1} $arcmin^{-2}$) and IRAS intensity (units are MJy sr^{-1}) for the Q0000 field.

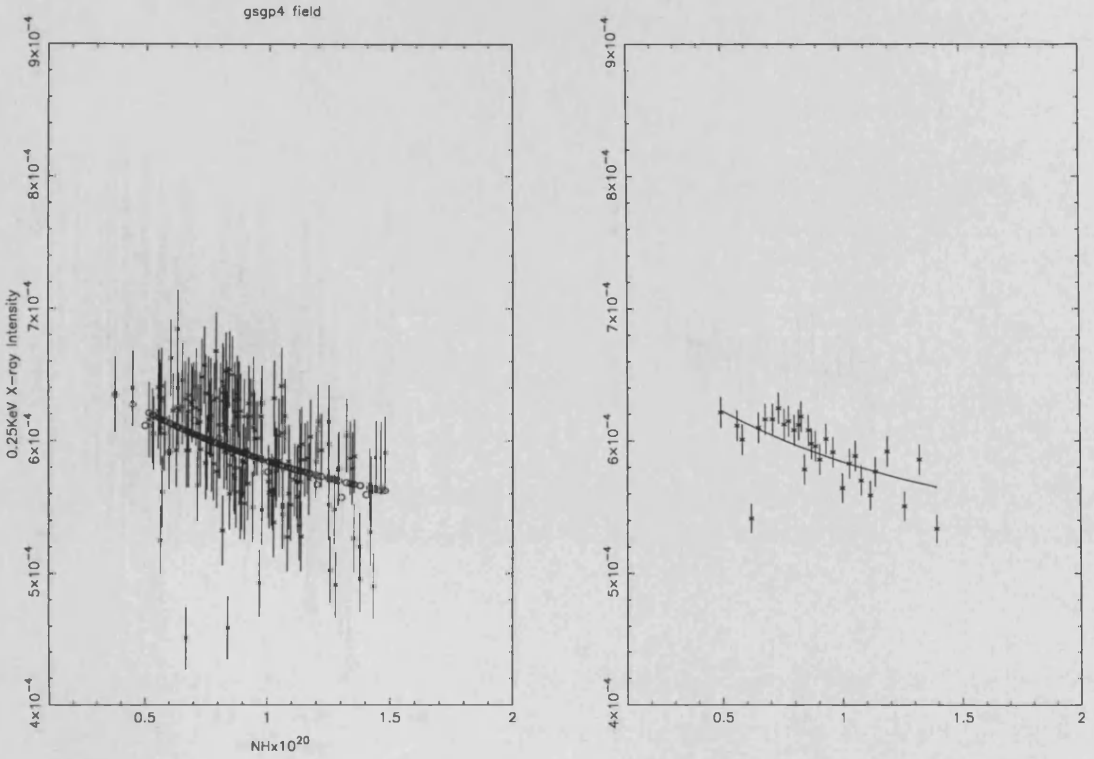

Figure 6.8: The correlation between 0.25 kev X-ray intensity (units are 10^{-6} counts s^{-1} $arcmin^{-2}$) and IRAS intensity (units are MJy sr^{-1}) for the GSGP field.

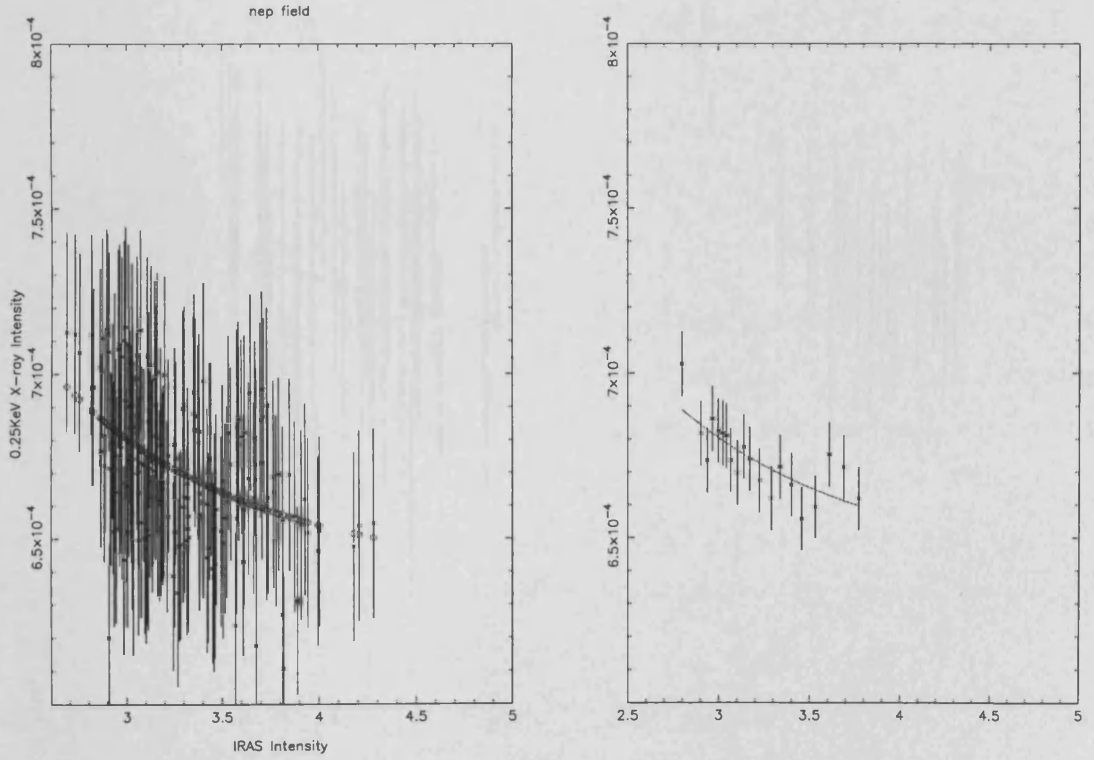

Figure 6.9: The correlation between 0.25 kev X-ray intensity (units are 10^{-6} counts s^{-1} $arcmin^{-2}$) and IRAS intensity (units are MJy sr^{-1}) for the NEP field.

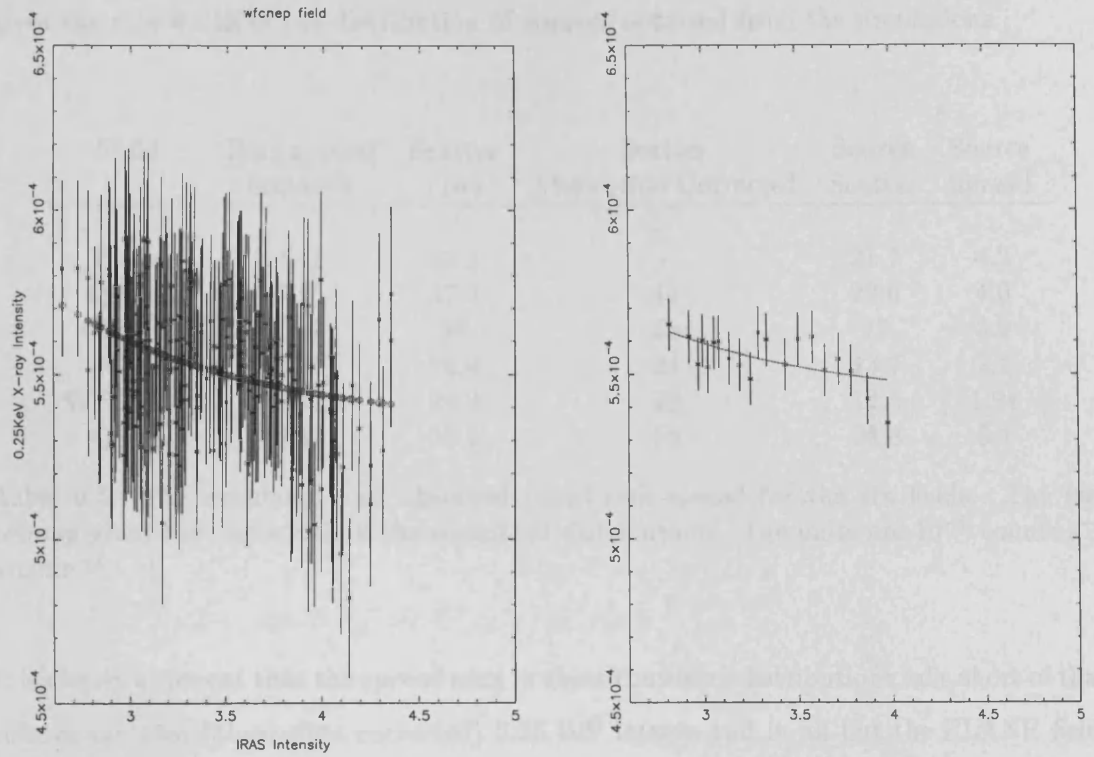

Figure 6.10: The correlation between 0.25 kev X-ray intensity (units are 10^{-6} counts s^{-1} $arcmin^{-2}$) and IRAS intensity (units are MJy sr^{-1}) for the WFCNEP field.

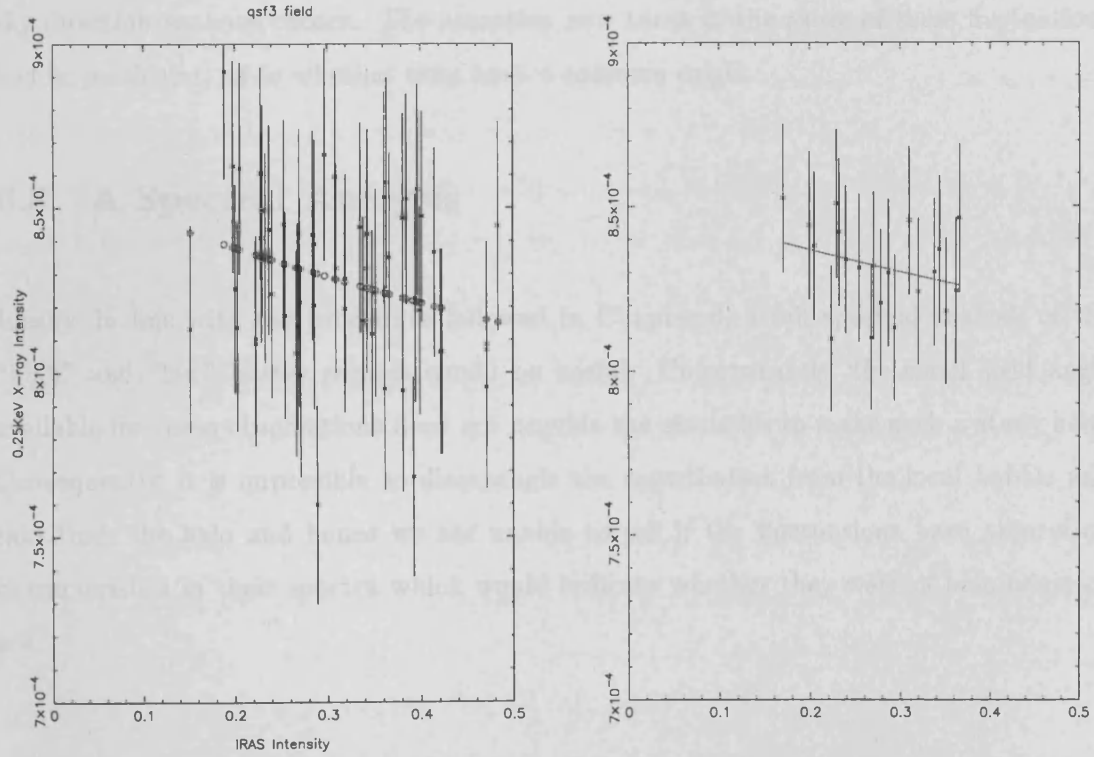

Figure 6.11: The correlation between 0.25 kev X-ray intensity (units are 10^{-6} counts s^{-1} $arcmin^{-2}$) and IRAS intensity (units are MJy sr^{-1}) for the QSF3 field.

gives the rms width of the distribution of spreads obtained from the simulations.

Field	Background intensity	Scatter (1σ)	Scatter Absorption Corrected	Source Scatter	Source Spread
Plane	641	22.5	-	21.7	4.2
Q0000	715	47.3	45	22.6	4.0
GSGP4	587	48	36	19	3.0
NEP	671	26.4	24	13.7	2.2
WFCNEP	552	24.2	22	12.5	1.94
QSF3	837	56.2	56	28.8	6.4

Table 6.5: The simulated and observed count-rate spread for the six fields. The last column gives the rms width of the simulated distributions. The units are 10^{-6} counts s^{-1} $arcmin^{-2}$.

It is clearly apparent that the spread seen in these confusion distributions falls short of that seen in the true (absorption corrected) 0.25 keV images and in all but the PLANE field, represent a fluctuation $>3\sigma$ above the maximum confusion contribution. Consequently, the fluctuations appear to be significant and can be seen (to a varying extent) in every sky direction we have chosen. The attention now turns to the cause of these fluctuations and in particular, as to whether they have a common origin.

6.8 A Spectral Analysis

Ideally, in line with the procedure followed in Chapter 6, a full spectral analysis of the "high" and "low" blister regions would be useful. Unfortunately, the small solid angle available for these observations does not provide the statistics to make such a study here. Consequently, it is impossible to disentangle the contribution from the local bubble and that from the halo and hence we are unable to tell if the fluctuations have absorption characteristics in their spectra which would indicate whether they were of halo origin or not.

Field	Mean 0.25keV Intensity $\times 10^{-6}$ counts s^{-1} $arcmin^{-2}$	All-sky 0.25keV Intensity $\times 10^{-6}$ counts s^{-1} $arcmin^{-2}$	0.25keV Intensity Range $\times 10^{-6}$ counts s^{-1} $arcmin^{-2}$
Plane	641	386	350-408
Q0000	715	731	643-801
GSGP4	587	675	567-718
NEP	671	563	519-605
WFCNEP	552	565	519-605
QSF3	837	1085	1007-1302

Table 6.6: The mean 0.25keV background X-ray intensities for each of the fields and the range of values obtained for the same sky direction in the ROSAT all-sky survey.

6.9 The extent of the fluctuations

To determine the true extent of the fluctuations it is important to ensure the full extent of the LTE component has been subtracted. For the 0.25keV band, it is possible to reduce the contamination from the LTE component by comparing the count-rate to that observed for the same region of sky in the ROSAT all-sky survey. Since, in the all-sky survey, the overlap of adjacent fields allows a minimisation of the LTE component across the whole sky. The all-sky survey data were available in pixels of $40' \times 40'$ and an array of 3×3 pixels were obtained for the pointing direction of each of the fields. The range of 0.25keV count-rates seen in each set of nine pixels, and their average are compared to the average background count-rate seen in the six fields in Table 6.6.

Clearly, in two of the fields (Plane and NEP), the 0.25keV intensity observed in the background subtracted observations is considerably greater than that observed in the all-sky survey and a significant offset needs to be subtracted. However, in all but one of the other fields the background count-rate falls within the range observed for the 9 all-sky survey pixels and no change is required. In the remaining field, (QSF3), the all-sky survey background intensity is far greater than in the background subtracted pointed observation. This could be because, either the total LTE component was smaller during the pointed observation period than throughout the all-sky survey, or that the background subtraction has been too rigorous. On inspection of Table 6.4 it can be seen that far more

LTE intensity is subtracted from the QSF3 field than any other.

To correct the fields to the level of the 0.25keV all-sky survey, we have subtracted a value equal to the difference between the mean pointed observation intensity and the all-sky survey intensity for the NEP and PLANE fields when considering the fractional intensity of the fluctuations.

The presence of fluctuations to a FWHM level of $\sim$ 10% (1σ=4%) has been demonstrated for all six fields considered in this chapter (and the Lockman field considered in the previous chapter). A summary of the extent of the fluctuations is given in Table 6.7. It can be seen that the fractional intensity of the fluctuations is remarkably constant across the sky, with an average 1σ magnitude of 5%. In all but the Plane field, the fluctuations are clearly above the spread expected from source confusion. It should be noted that throughout this analysis the various scatter contributions that have been determined provide an upper limit estimate to the predicted scatter, so that even in the Plane field, the fluctuations observed are probably significant. It is also interesting to note that the absoloute magnitude of the fluctuations appears to increase with path length through the halo. Inspection of Table 6.7 shows that Fields 1, 4 and 5 all exhibit relatively small fluctuations, while those away from the plane (2, 3 and 6) exhibit much larger ones. In addition, the fluctuation seen in Field 6 is much larger than those seen in Fields 2 and 3 (which are in the direction of the south galactic pole and consequently sample less of the halo). However, the errors associated with the fluctuation measurements and the small number of data points does not allow us rule out a more local source for the fluctuations.

Consequently, there remains two mechanisms which could explain such fluctuations and these are considered separately below.

(i) Variations in absorption column density across the field of view

Although this effect should have been corrected for by the correlation with the IRAS data, there remains the possibility of absorption by species other than HI. However, the spectral fitting performed on the UKMS data indicated that the fluctuations in that field (certainly those from the high intensity regions) could not be explained by variations in column density. It would also be interesting to compare the scale size and magnitude

Field	l^{II}	b^{II}	N_H 10^{20} atoms cm^{-2}	Count-rate 10^{-6}	Fluctuation 10^{-6}	Ratio	Error
Plane	54	0	93.5	641	23	0.06	0.06
Q0000	36	-79	1.83	715	47	0.07	0.03
GSGP4	234	-89	1.95	587	36	0.06	0.03
NEP	96	30	5.10	671	24	0.04	0.02
WFCNEP	96	30	5.23	552	22	0.04	0.02
QSF3	251	-52	1.70	837	56	0.05	0.03

Table 6.7: A summary of the six fields and the fluctuations observed.

of the fluctuations seen here with the small scale HI variations discussed in Chapter 4. However, even at best, the sky coverage obtained for the sources considered in Chapter 4 falls far short of the scale size of the x-ray intensity fluctuations so it is not possible to compare them.

(ii) Variations in emission

Two processes can explain the presence of fluctuations in thermal emission. The first would be variations in the temperature of the emitting gas and the second would be variations in emission measure. As pointed out by Barber (see Barber 1994), it is very unlikely that the required variation in temperature ($\Delta T \sim 7 \times 10^5 K$) could be supported (at the scale size of the PSPC field of view). Instead, the most likely scenario is one where the variations are caused by changes in emission measure, in which case the fluctuations could be "bubbles" of hot gas. The question arises as to whether these bubbles are located locally (i.e. within, or at the edge of the local cavity) or from within the Galactic halo.

(a) from within the halo

The existence of clumping of gas in the halo at the scale size of several degrees has already been suggested (see Snowden *et al.* 1998) to explain the two temperature fits required to fit this component in the all-sky survey data. Therefore it would not seem unreasonable to suggest that there is also clumping at smaller scale sizes. The presence of such clumping may be explained in terms of the fountain effect in which gas which is heated in the plane of

the Galaxy rises with its increased buoyancy into the halo where it cools and re-circulates maintaining a dynamic equilibrium (e.g. Kahn 1997).

The count-rate of the fluctuations which are observed can be converted to an emission measure by assuming a spectral model. Assuming an average fluctuation range ($4 \times \sigma$) of 140×10^{-6} counts s^{-1} $arcmin^{-2}$, a thermal temperature of 10^6 K and that the absorbing material is entirely in front of the emission, then the emission measure of a typical fluctuation is $\sim$ 0.0028 $cm^{-6}pc$. An emission measure increase caused by such bubbles would imply an increase in density and hence thermal pressure. The magnitude of this increase depends on the angular size and distance to the bubble. The electron density within a bubble is related to the emission measure of the material through the equation;

$$EM = \int (n_e^2 dx) \tag{6.2}$$

where, n_e is the electron density and dx is the path length through the material. Here, the bubbles are assumed to be spherical and hence dx is the diameter of the bubble (D). The value of D is dependent on the angular size of the fluctuation and the distance to the bubble. Consequently for a bubble with an emission measure of 0.0030 $cm^{-6}pc$ and a scale size of 20′, the density of the bubble, n_e can be written:

$$n_e = \frac{0.5}{\sqrt{L}}$$

where L is the distance to the bubble.

The electron density is related to thermal pressure through the equation;

$$P = 2.1 \times n_e kT \tag{6.3}$$

so that the pressure in the bubble can be defined as:

$$\frac{P}{k} = \sqrt{\frac{0.0030}{L}} \times T \tag{6.4}$$

where T is the thermal temperature of the plasma in the bubble.

Consequently, for a typical halo distance of 5 kpc, the scale size of the bubble would be $\sim$ 30 pc and the pressure and density would be $2.1\times\ 10^4$ cm^{-3}K and 0.01 cm^{-3} respectively. Assuming that the lifetime of such a bubble depends on the sound crossing time, then the bubbles should exist for approximately 10^6 years (assuming that they are at a temperature of 10^6 K).

(b)

If the bubbles exist solely within the cavity, then the variation in count-rate observed amounts to a delta emission measure of $\sim$ $14\times\ 10^{-4}$ cm^{-6}pc (assuming thermal emission from a 10^6 K plasma and no absorption). The work in Chapter 4 indicated an average cavity radius of approximately 60 pc so if the fluctuations were located at the edge of the cavity, their pressure and density would be $1.3\times\ 10^5$ cm^{-3}K and 0.06 cm^{-3} respectively. Clearly, this pressure is a factor 10 above the hot phase of the ISM and would imply that they were created by a high energy event (such as the expansion of the local cavity).

The existence of such density variations for the material within the local bubble is not unlikely, if the bubbles are situated within the cavity itself then their scale size and density place constraints on the models for the X-ray background and suggest that an intermixed model is most likely. Alternatively, if they are situated at the edge of the cavity then they are more likely to be caused by the expansion of the local cavity and this places limits on the age and size of the supernova remnant thought to have produced it.

If the bubbles originate at the edge of the cavity then they may be of a dynamic nature and could possibly be associated with the current expansion of the local cavity. In which case, their nature should reveal information on the distance to the cavity edge and the nature of the ISM beyond the cavity edge.

6.10 Conclusion

The fluctuations which are seen in each of the six fields, have been shown to be in excess of that expected from absorption effects and source confusion alone. It is most likely that the fluctuations are caused by variations in emission measure but the location along the line of sight is unknown. However, since they are seen in the Plane field, there is probably a contribution from within the plane of the galaxy. The true nature and cause of such density enhancements awaits progress in the non-equilibrium ionisation emission codes and shock front physics. Advancements in these fields should result from spectroscopic studies to be performed by the AXAF and XMM observatories in the near future.

Chapter 7

The X-ray Calibration of the CUBIC CCD's

Overview

This chapter describes the calibration of the CUBIC CCD's. It includes a discussion of the theoretical response of the detectors as well as an outline of the results obtained from laboratory and synchrotron calibrations. Unfortunately, the launch of SAC-B, the satellite which contained CUBIC, failed due to problems with the third stage of the Pegasus Launch Vehicle. Proposals for the launch of CUBIC II are currently under consideration.

7.1 The CUBIC CCD's

CUBIC is a spectroscopic instrument and consequently, a precise understanding of its energy resolution and efficiency is essential if the maximum science is to be obtained from its data. However, a very large number of measurements would be required to calibrate the detector across its bandpass because the response can vary very rapidly with energy. For that reason we have chosen to combine detailed device modelling, that simulates the detector performance, with laboratory calibrations to obtain a detailed response matrix, in which the overall response is interpolated from a few laboratory measurements. This chapter starts with a description of the physical processes that determine the quantum efficiency (QE) and energy resolution of the instrument and then proceeds to describe the model used to simulate its performance. This is followed by a description of the laboratory techniques employed to calibrate the resolution and QE of the device at individual energies. These measurements were carried out at a local laboratory and at the synchrotron in Wisconsin.

7.2 Device performance

The two factors which are of primary importance to the observations of astrophysical plasmas are the effective area and energy resolution of the detector, particularly their variation with energy. A good understanding of the effective area of the device enables better determination of absorption columns and power law indices, while a good calibration of the energy resolution allows a better determination of the temperature, density or ionisation state associated with the width, relative intensity or energy of a spectral line. The physics and device characteristics which determine these two factors are now considered in detail.

7.2.1 Quantum Efficiency

The total quantum efficiency of an instrument is described in terms of its ability to detect photons. This is dependent on the detection system as a whole, including the effects of filters and the CCD structure. Consequently, the total quantum efficiency of the device

can be written:

$$QE(E) = T_{filter}(E) \times T_{deadlayer}(E) \times (1 - T_{depletion}(E)) \tag{7.1}$$

Where,

E	=	photon energy
$T_{filter}(E)$	=	the transmission of the filter
$T_{deadlayer}(E)$	=	the transmission of the electrode dead layers
$(1 - T_{depletion}(E))$	=	the depletion depth absorption probability

This function is highly dependent on energy, with the efficiency varying by a few orders of magnitude between 0.1 and 10 keV.

The first two terms in the equation describe the probability that a photon will be absorbed before it reaches the active region of the detector (the depletion or field free region of the device), and limits the performance at low energies. This region, deemed to be the dead layer of the device includes the electrodes and inter electrode insulating oxides. Consequently, this term is highly dependent on the geometry of the electrode structure, depending on both the thickness of the layers and their pixel coverage. The third term in the equation describes the probability of an interaction within the detector volume which depends on the photo-electric absorption cross section of the detector and reduces the QE at high energies.

7.2.2 Energy Resolution

A CCD can only be used for X-ray spectroscopy while operated in photon counting mode. This requires that only one photon is collected in a pixel during a single integration. The energy resolution that can be achieved is limited by the noise of the system. Noise modifies the size of the charge associated with an X-ray event which alters the final energy determination. The two major types of noise which contribute to this system are:

(i) Noise due to charge generation and trapping

Charge generation noise includes shot noise and dark current noise. Shot noise is the

statistical variation in the number of charge carriers produced by the interaction of a photon in the device. The restriction on the energy of an electron making the transition from valence to conduction band results in a modification to the variance predicted by Poissonian statistics. This modification is approximately constant with energy for a given material and is known as the Fano factor (Fano 1947). Consequently, for an incident X-ray beam, the variance in the number of carriers generated is expressed as:

$$\sigma^2 = fE/\omega \tag{7.2}$$

where f is the Fano factor of the material, E is the Energy of the photon (eV) and ω is the energy required to liberate one electron hole pair, which for silicon is approximately 3.68 eV (Bertolini & Coche 1968) although this value does vary slightly with energy. The Fano factor is approximately 0.12 although there is debate about its exact value (see, for example, Owens 1996). For a 5 keV photon, the total charge generated is about 1400 electrons resulting in a shot noise of $\sim$12 electrons.

Dark current results from the promotion of electrons in to the conduction band by phonons. The magnitude of this component is described by three separate components (see Grove 1967). The first is associated with the depletion region of the CCD, the second with the un-depleted epitaxial silicon and the third with the layer and surface states between the Si and SiO_2 interface. Each term is temperature dependent with the typical rms noise varying from 170 electrons at room temperature to below 1 electron at -90°C. Since the device described here is operated at liquid nitrogen temperatures the effects of dark current are ignored.

Charge transfer noise results from the trapping and hence loss of charge from a charge packet as it is transferred from the original point of the photon interaction to the output node. The charge transfer efficiency of this device is approximately 0.999995 per transfer so its typical magnitude is less than three electrons at $\sim$5 keV. Again, this component is ignored in this analysis.

(ii) Readout noise

Readout noise is comprised of the Johnson and flicker noise associated with the output transistor and reset noise which results from fluctuations in the reset potential of the

output capacitor.

Johnson noise is due to random thermal motion and has a white noise distribution while flicker noise, thought to be due to fluctuations in electron mobility within the transistor channel, has a spectrum with an approximately $\frac{1}{f}$ form resulting in higher noise at lower frequencies. Typical noise values for the Johnson and Flicker components in the *output* transistor are about 3-4 electrons rms. However the variations in reset potential caused by Johnson noise in the channel of the *reset* transistor can have a magnitude of ~570 electrons. Consequently, correlated double sampling techniques are used to reduce this component. For this type of system the typical noise ranges from 3-10 electrons. The total readout noise associated with an event increases with the number of pixels that it occupies so that the best energy resolution is obtained for single pixel events;

$$n_{tot} = \sqrt{N \times \sigma_r^2} \tag{7.3}$$

where, n_{tot} is the total readout noise, N is the number of pixels associated with the event and σ_r is readout noise for each pixel. The number of pixels associated with an event depends on the initial size of the charge cloud and spreading due to thermal diffusion. The total extent of the spreading depends on the depth of interaction and the structure of the CCD and is considered in detail below.

7.3 The CUBIC CCD's and device modelling

The CUBIC CCD's are three-phase front illuminated devices with a pixel size of 27x27μm^2. They have a gate structure similar to the CCD's developed for the JET-X instrument on the Spectrum-RG mission (Wells *et al.* 1990) which have been described in detail by Owens *et al.* (1996). These types of CCD have three electrodes per pixel element which are made from polysilicon. Each electrode is insulated from the others using a silicon oxide and the entire device is covered with a further oxide layer to prevent shorting of the electrodes at the surface. The CUBIC devices differ from the standard CCD format because one of the electrodes is thinned to reduce absorption in the dead layers and hence enhance

performance at low energies.

The overall performance of this device is to be modelled using a "Monte Carlo" simulation which includes the effects of the electrode structure on the energy dependence of the quantum efficiency and the effects of noise on the resolution. The models used for these terms are considered separately below.

7.3.1 Device QE

As mentioned above, the device QE depends on the filter, the electrode structure (dead-layer) and the depletion depth of the CCD. The filter is composed of ~850$\AA$ of aluminium and ~450$\AA$ of titanium. The dead-layer consists of the electrodes, the electrode oxides, a silicon oxide passivation layer and a silicon nitride dielectric layer. In this device, two of the electrodes (P1 & P2) are 0.6 μm thick while the third (P3) is thinned to 1750 $\AA$. The oxides covering the P1 & P2 electrodes are 1.2μm thick while the oxide covering the P3 oxide is thinned to a nominal 10 $\AA$. The passivation and dielectric layers are both 0.085 μm thick.

The thinned electrode covers a third of the pixel area and the depletion layer is approximately 35μm thick resulting in a quantum efficiency of the form:

$$QE(E) = QE_{filt}(E) \times QE_{dead}(E) \times QE_{depln}(E) \tag{7.4}$$

where,

$$QE_{filt}(E) = \left(e^{\frac{-0.085}{\lambda_{Al}} + \frac{-0.045}{\lambda_{Ti}}}\right)$$

$$QE_{dead}(E) = \left(\frac{2}{3} \times e^{\frac{-0.085}{\lambda_{SiO_2}} + \frac{-0.085}{\lambda_{Si_3N_4}} + \frac{-0.6}{\lambda_{Si}} + \frac{-1.2}{\lambda_{SiO_2}}} + \frac{1}{3} \times e^{\frac{-0.085}{\lambda_{SiO_2}} + \frac{-0.085}{\lambda_{Si_3N_4}} + \frac{-0.2}{\lambda_{Si}} + \frac{-0.001}{\lambda_{SiO_2}}}\right)$$

and $QE_{depl}(E) = \left(1 - e^{\frac{-35}{\lambda_{Si}}}\right)$

where, λ is the attenuation length in the material indicated (μm).

7.3.2 Charge Spreading

For the purposes of modelling charge spreading, the structure of a CCD can be represented by simple planar geometry consisting of the dead layers described above, a depletion region, a field-free region and a p^+ substrate.

The charge cloud created when an X-ray is photo-electrically absorbed in the depletion layer is generally collected in the pixel in which it interacts. This charge is accelerated by electric fields to the buried channel region where it is stored before readout. However, a charge cloud generated by an X-ray absorbed in the weaker fields near the depletion edge or in the field free region below the depletion layer may only be partially collected in a single pixel. In this case, the charge cloud takes longer to be collected and some of the charge can be lost to neighbouring pixels by radial spreading. To maintain good QE, the majority of the charge can be accounted for by summing adjacent pixels. However, as mentioned previously, this process reduces the spectral resolution because the event has to be read out from several pixels, each of which contributes a read-noise component.

To determine the extent of this loss in resolution and its variation with energy the various mechanisms that contribute to charge spreading are now considered.

Fitting, Glaefeke & Wild (1977) have shown that the charge cloud generated by the photoelectric absorption of an X-ray in silicon has a Gaussian profile with a 1 σ radius of:

$$r_i = 0.257\ R_e \tag{7.5}$$

where R_e is the range of the primary electron. The range of the primary electron can in turn be calculated from the Everhart and Hoff equation for silicon which is given by:

$$R_e = 0.0171\ E_e^{1.75} \tag{7.6}$$

where E_e is the electron energy in keV (Everhart & Hoff (1971)).

The width of this charge cloud increases through diffusion as it drifts towards the storage region. An estimate of this increase can be obtained from the Einstein relation with the assumption that the diffusion occurs over a time period equal to that taken to drift from the point of interaction to the storage depth. The drift period can be obtained by solving Poissons equation within the depletion region to determine the electric field distribution and hence the average drift velocity.

The resulting 1σ radius of the charge cloud is given by:

$$r_d \sim \sqrt{\frac{2kT\epsilon_s}{e^2 N_a} ln\left(\frac{x_d}{x_d - x}\right)} \tag{7.7}$$

where, N_a is the acceptor dopant concentration, T is the temperature, ϵ_s is the permittivity of silicon, x_d is the depth of the depletion region and x is the depth of the interaction.

There is additional spreading for charge clouds generated in the field free region of the device. This process has been studied by Janesick *et al.* (1985) who show that the additional 1σ radius for a charge cloud generated in the field free region is given by:

$$r_f = \frac{x_{ff}}{2}\sqrt{1 - \left(\frac{x}{x_f}\right)^2} \tag{7.8}$$

A further complication arises for interactions which occur within the field free region of a device because some charge is lost due to recombination as the charge cloud diffuses. The magnitude of this charge loss has been investigated by Hopkinson (1987) who show that for a CCD fabricated on p-epi/p^+ substrate the total amount of charge reaching the depletion layer is given by:

$$q_{total} = q_0 \left[\frac{exp\left(\frac{x_{ff}-x}{L}\right) + exp\left(-\frac{x_{ff}-x}{L}\right)}{exp\left(\frac{x_{ff}}{L}\right) + exp\left(-\frac{x_{ff}}{L}\right)}\right] \tag{7.9}$$

where q_0 is the size of the initial charge cloud, x_{ff} is the depth of the field free layer, L is the diffusion length (typically 75 μm) and x is the depth of interaction.

Finally, Holland (1990) indicates that for charge generated in the device substrate, the 1σ charge cloud radius is given by:

$$r_s \sim \frac{L}{2.2}\sqrt{1-\left(\frac{x}{L}\right)^2} \tag{7.10}$$

and that the total charge reaching the field free layer is given by:

$$q_{total} = q_0 exp\frac{x}{L} \tag{7.11}$$

7.3.3 Photon interactions and the silicon escape peak

At energies above the Si-K energy level, photoelectric absorption results in the ejection of an electron with energy $E_e = E_\gamma - E_b$, where $E_b = 1.84$ keV is the electron binding energy (if the X-ray energy is below E_b, an L-shell electron is ejected). Once a silicon atom has been ionised it can de-excite by emitting Auger electrons and/or fluorescent photons. The primary and Auger electrons are absorbed very close to the point of interaction resulting in a charge cloud proportional to the energy of the incoming photon. However,in silicon, the fluorescent photons have a mean free path of about 12.3 μm so that there is a possibility they will escape from the pixel. If this happens, then the energy associated with the event will be reduced by the energy of the photon forming an escape peak in the pulse height distribution of the detector. The fraction of events which contribute to this peak depends on the K-shell fluorescent yield (~4.5%), the depth of interaction and the size of the pixels.

7.3.4 Other Considerations

For a complete model of the CCD performance, the effects of EXAFS (X-ray Absorption Fine Structure) and the variation of ω with energy should also be considered. However these effects are only significant at the 5% level (Keay 1997) so they are ignored in this analysis.

7.4 The Simulation

The simulation considers a number of input energies over the 0.1 to 10.0 keV range. A total of 1000 photons are simulated for each input energy. The quantum efficiency of the electrode structure and filter are calculated for each input energy and then the depth of interaction is drawn from a random exponential distribution with a mean equivalent to $1/\lambda_{si}$. If the energy is above 1.84 keV, the escape probability is determined by considering both the depth of interaction and the available solid angle for escape and the QE is modified. Depending on the depth of interaction, the appropriate amount of spreading/charge loss is applied according to the equations given in Section 7.3. The noise components are drawn from Gaussian distributions and incorporated into the output signal. Finally, noise thresholding (equivalent to that used in the laboratory) is applied and the resulting output channel is determined using the measured gain of the CCD (see below).

7.5 Calibration

7.5.1 Laboratory Calibration

For the calibration of the noise and gain of the CUBIC CCD's we used a Kevex source to produce X-rays. This incorporated an emission cathode which released electrons on heating that were accelerated by a large (variable) electric field. These high energy electrons were directed at various sources (Al, Si, Ti, & V) to obtain X-rays from the relaxation of excited Kα states. The energies associated with these emission lines are given in Table 7.1.

Source	Energy keV
Al	1.45
Si	1.74
Ti	4.51
V	4.95

Table 7.1: The energies of the Kα fluorescence line for each of the elements used.

The CCD was mounted in a vacuum cryostat and pumped down to a pressure of $\sim 1\times 10^{-3}$ Torr using a rotary pump. This was required to avoid the condensation of contaminants on to the CCD surface during cooling. A temperature of 180 K was maintained using a copper cold finger connected to a liquid nitrogen dewar. The X-ray producing sources were mounted on a rotating turn-table at the front of the cryostat.

The biases and clock signals required to drive the CCD were produced by an electronic sequencer situated in a CAMAC. The output CCD signals were passed through a low noise amplifier (pre-amp) to an analogue signal processor which performed correlated double sampling to reduce reset noise. This was achieved using a dual slope integrator circuit which operated as follows. Firstly, the reset signal was integrated for a period of 10 μs, then, when the output signal was clocked on to the output node, the signal was integrated again. The difference between these two levels formed the corrected signal. Clearly, the gain and noise of the system depend on the integration period selected. The final signal was digitised to 12 bits (providing 4096 channels) and passed to an Archimedes 440 micro-computer for collection and on-line analysis. To reduce the amount of data, on-line software was used to analyse the noise peak (i.e the Gaussian peak formed due to the read-noise of the system when the zero level signal is sampled). Only pixels which have a signal >5 times the standard deviation of this peak are stored.

Plots of the spectra obtained from these sources appear in Figure 7.1. The stability of the CCD gain with energy is indicated in Figure 7.2 (a), where the peak channel is plotted as a function of the emission line energy. Linear interpolation was used to determine the average gain which was 1.67$\pm$ 0.01 eV/channel. The residuals of the data points from this best fit line are plotted as a function of energy in Figure 7.2 (b) where it is clear that the gain is very stable across the energy band although the residuals do increase slightly with energy. The best-fit line does not pass exactly through the origin because of inaccuracies in the thresholding technique described above.

The resolution of the spectral lines was determined by fitting a Gaussian function to the spectra. The best fit parameters are given in Table 7.2.

Since the typical read-noise of the system has the form:

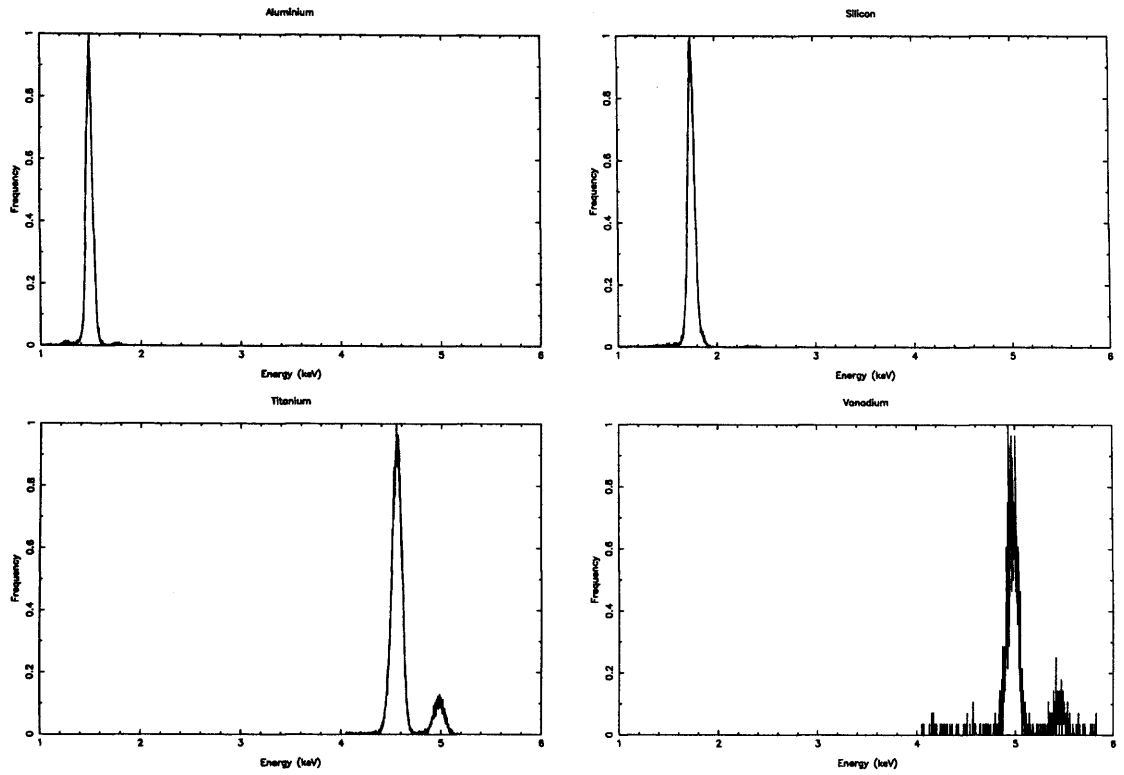

Figure 7.1: The spectra obtained for the four X-ray sources. Each plot has been normalised to its peak value.

Source	Peak Channels	σ Channels
Al	915	20.4
Si	1072	21.2
Ti	2791	30.3
V	3065	31.5

Table 7.2: The best fit parameters

$$\sigma = \sqrt{\left(\frac{fE}{\omega} + \sigma_r^2\right)}$$

a plot of σ^2 versus energy should result in a straight line with a gradient equal to $\frac{f}{\omega}$ and a y-axis intercept of the (read-noise)^2. Inspection of Figure 7.3 shows this to be the case and linear interpolation determines the gradient to be 0.0321±0.002 which is in excellent agreement with the value obtained from published values for f and ω (0.0318). The intercept of the best fit line is 31.4 electrons^2 which is equivalent to a read-noise of 5.6 electrons. This is in good agreement with the value determined in the on-line analysis

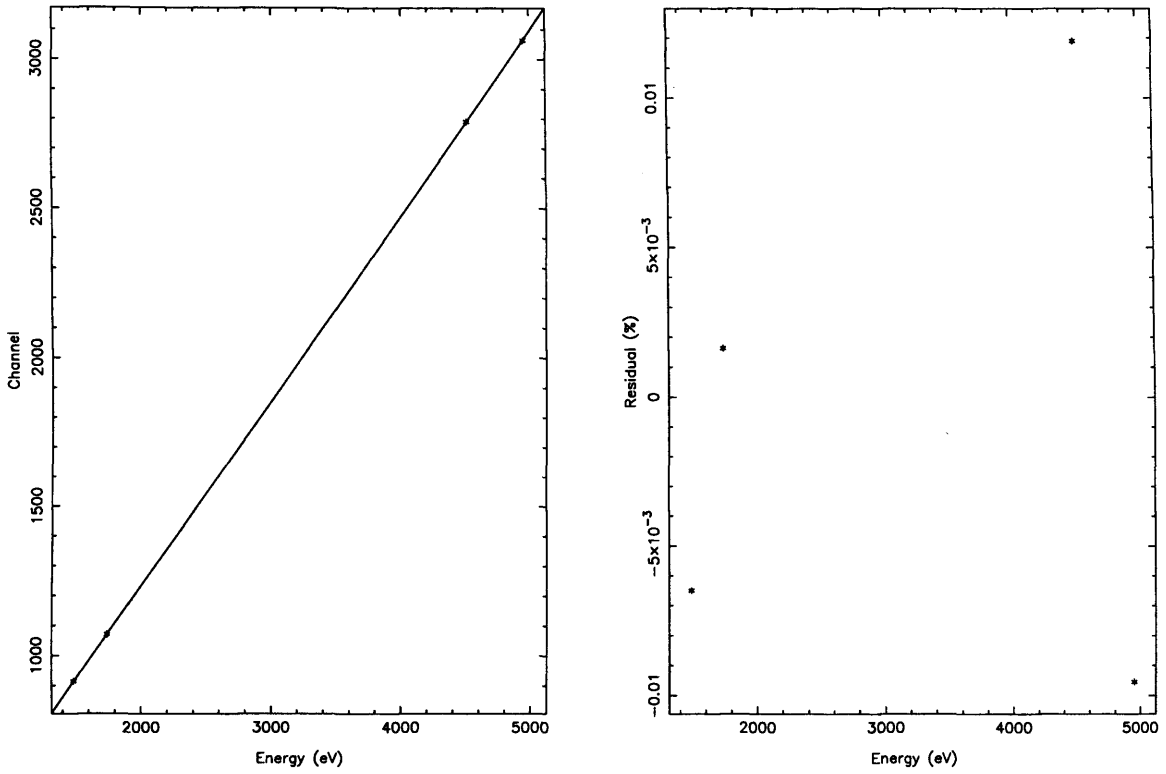

Figure 7.2: The figure to the left gives the peak channel as a function of energy. The solid line is the best fit line to these points determined using linear regression. The plot to the right gives the residual from this line for each of the data points.

of the noise peak in the data.

7.5.2 Synchrotron Calibration

For further verification of the noise calibration and for an investigation of the CCD/Filter quantum efficiency, the devices were also calibrated using a synchrotron source. The CCD was exposed to continuum synchrotron radiation from a 1 GeV electron beam-line at the University of Wisconsin-Madison Synchrotron Radiation Centre (SRC). Since the typical broadband X-ray flux produced in the normal mode of operation would destroy the CCD, it was necessary to reduce the number of electrons in the beam to allow single photon counting. This was achieved by operating the beam in a special "pico-beam" mode where only a few electrons are injected into the beam. The beam line used was the SRC Mark V Grasshopper Monochromator Beam-line. The beam was extracted from the storage ring using a bending magnet and was then reflected off a chromium coated flat onto a toroidal mirror to focus it onto a double crystal monochromator. This provided a

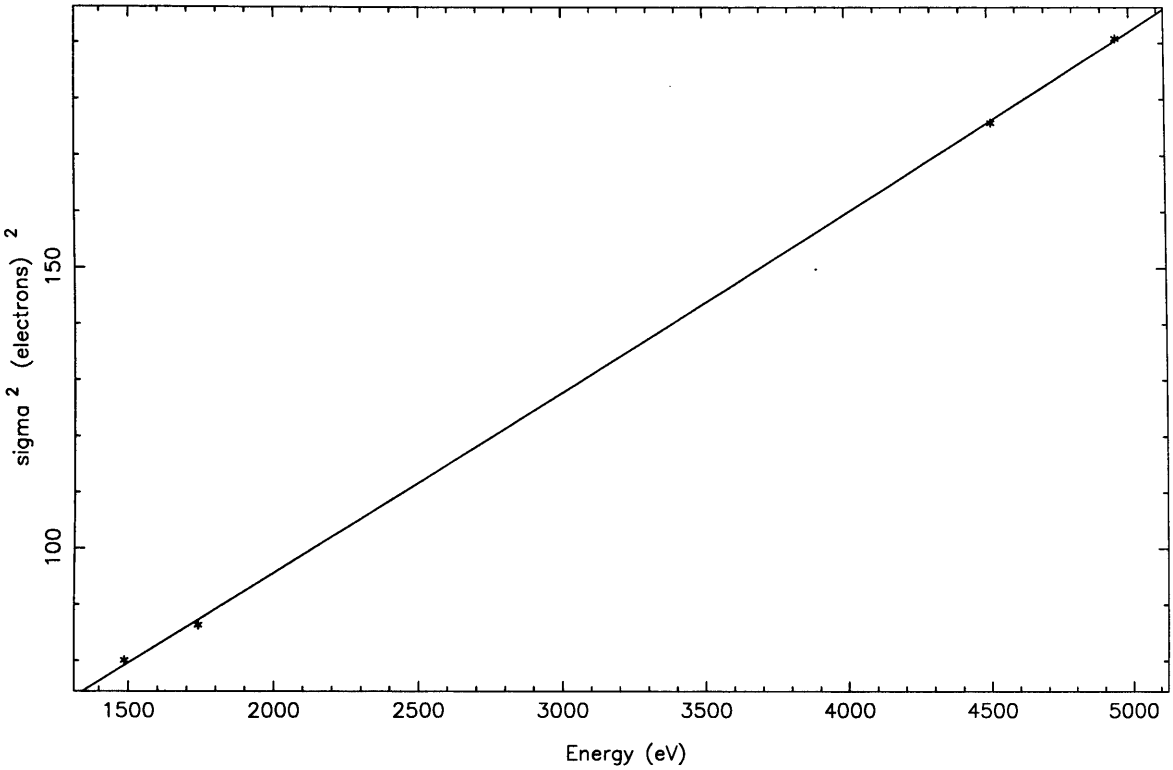

Figure 7.3: A plot of σ^2 as a function of energy for each of the data points. The solid line represents the best fit obtained from linear regression.

collimated monochromatic beam at the sample with the energy of the beam selected by shifting the grating. The movement of the grating was computer controlled using stepper motors with its position measured by a Heidenhain linear encoder. The encoder reading then represented a beam energy according to the grating equation shown below.

$$WL = d(sin(a) + sin(arcsin((D+L)/R) - (180 - a))) \tag{7.12}$$

a	=	angle of incidence on grating (degrees)	=	88.134
d	=	groove spacing on grating (Angstroms)	=	11111.1
L	=	slit to slit distance at zero order (mm)	=	130.015
R	=	radius of curvature of grating (mm)	=	2000.00
D	=	Heidenhain linear encoder reading (mm)		
WL	=	Wavelength (Angstroms)		
E	=	Energy (eV)		

The strength of the beam was measured for calibration purposes before and after each CCD reading. This was performed using a well calibrated photo diode (NIST-traceable photodiode). The CCD was operated in frame store mode with a shutter to prevent the collection of photons during readout. The data was passed through the CUBIC electronics which performed reset correction and digitisation to a SUN workstation for collection,

storage and analysis. For the calibration of the QE, measurements were taken at 0.1 keV intervals until an edge was passed at which point the intervals were reduced to 0.02 keV.

7.6 The response matrix

Figure 7.4 presents a two dimensional image of the final CUBIC response matrix resulting from the statistical model. The x-axis gives the input energy of a photon and the y-axis gives the probability distribution of the channel that the final count may be observed in. The intensity is plotted on a log scale and represents the QE associated with each energy and channel pair.

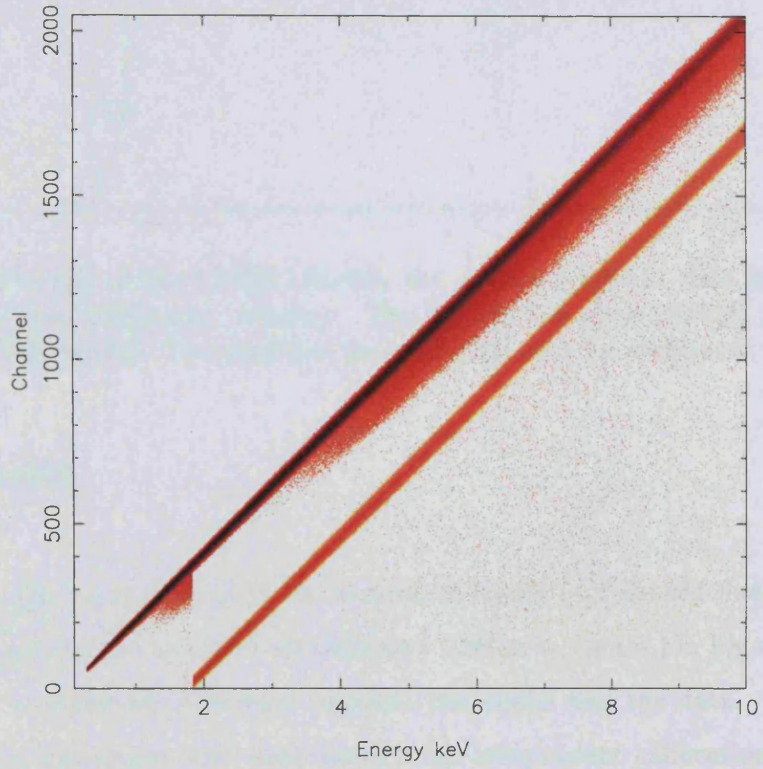

Figure 7.4: The CUBIC response matrix. The y-axis represents the channel in which a photon will be counted. The intensity is the convolution of the probability distribution of the channels in which a photon will be collected and the QE of the CCD.

Summing across this redistribution function gives the quantum efficiency of the device at a particular energy (see Figure 7.5). The main diagonal in Figure 7.4 represents the main response peak of the device while the secondary peak observed for energies above 1.8 keV represents the escape peak. The actual structure of the main peak (see Figure 7.6

is composed of two Gaussians because of the contribution from multi pixel events.

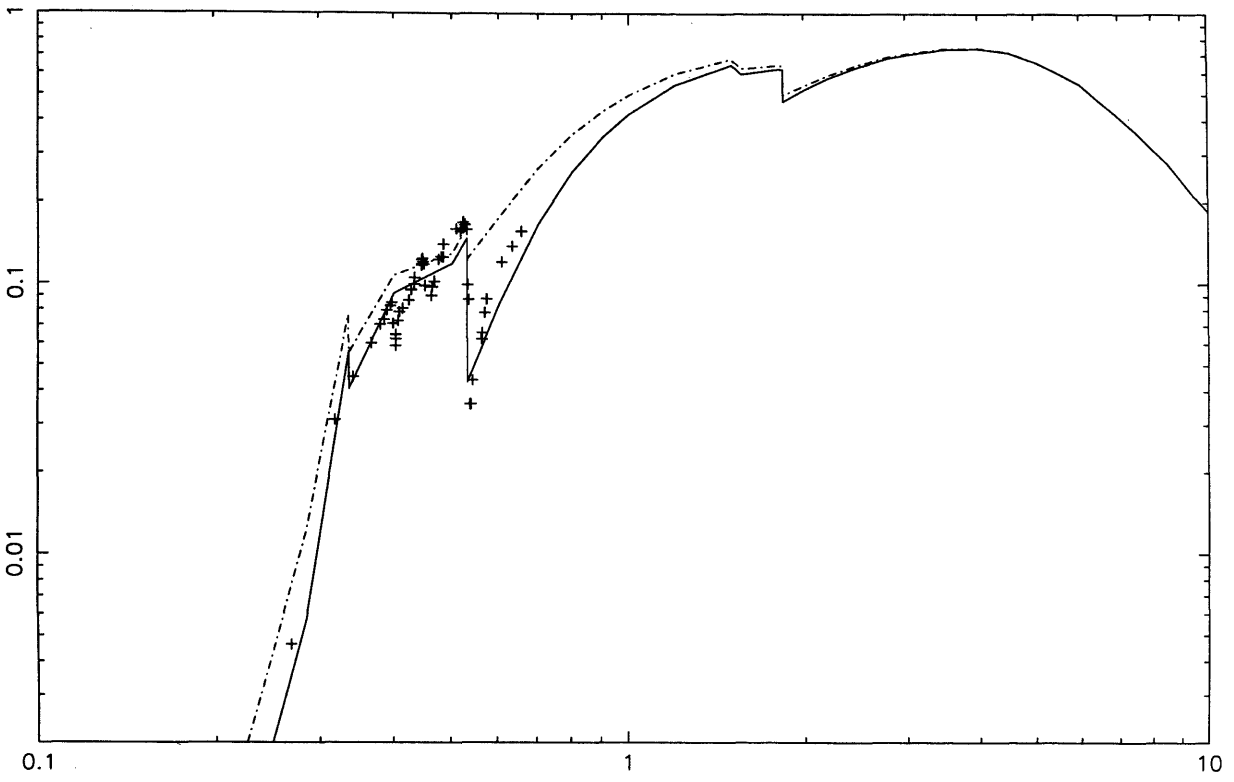

Figure 7.5: The QE of the CUBIC device, the crosses represent data taken at the synchrotron (Burrows 1996; *priv. comm.*). The dashed line gives the QE predicted by the standard CUBIC model. The solid line gives the QE with an additional VAPOX layer.

7.7 Results

A plot of the QE curve derived in the statistical model (dot-dashed line) is compared to the data gathered at the synchrotron (Burrows 1996;*priv. comm.*) in Figure 7.4. It is clear that there is considerable difference between the model and the data. The synchrotron data is in good agreement with data taken in an independent calibration (Burrows 1996; *priv.comm.*) so it would appear that it is the modelling which is inaccurate. However, by replacing the parameter quoted for the vapox layer on the third electrode with a value equivalent to that on the other pixels, a very good fit is achieved (see solid line in Figure 7.5; Burrows 1996 (*priv. comm.*)). It would seem that during the production process, the final vapox layer on the third electrode was not removed. This is conceivable since an SEM analysis of a previous batch of CCD's which use the same gate structure, has shown the final vapox layer to be still there. We await the results of an SEM analysis of the CUBIC

chip. The response matrix derived above (corrected for the additional oxide layer on the third electrode) is compared to the data using the XSPEC package. Spectral fits to two particular line energies are shown in Figure 7.6. In general, we found that the energy of a spectral line was determined to within 5% of the true value. The second plot in Figure 7.6 demonstrates how well the non-Gaussian response is modelled by the inclusion of charge spreading in the model.

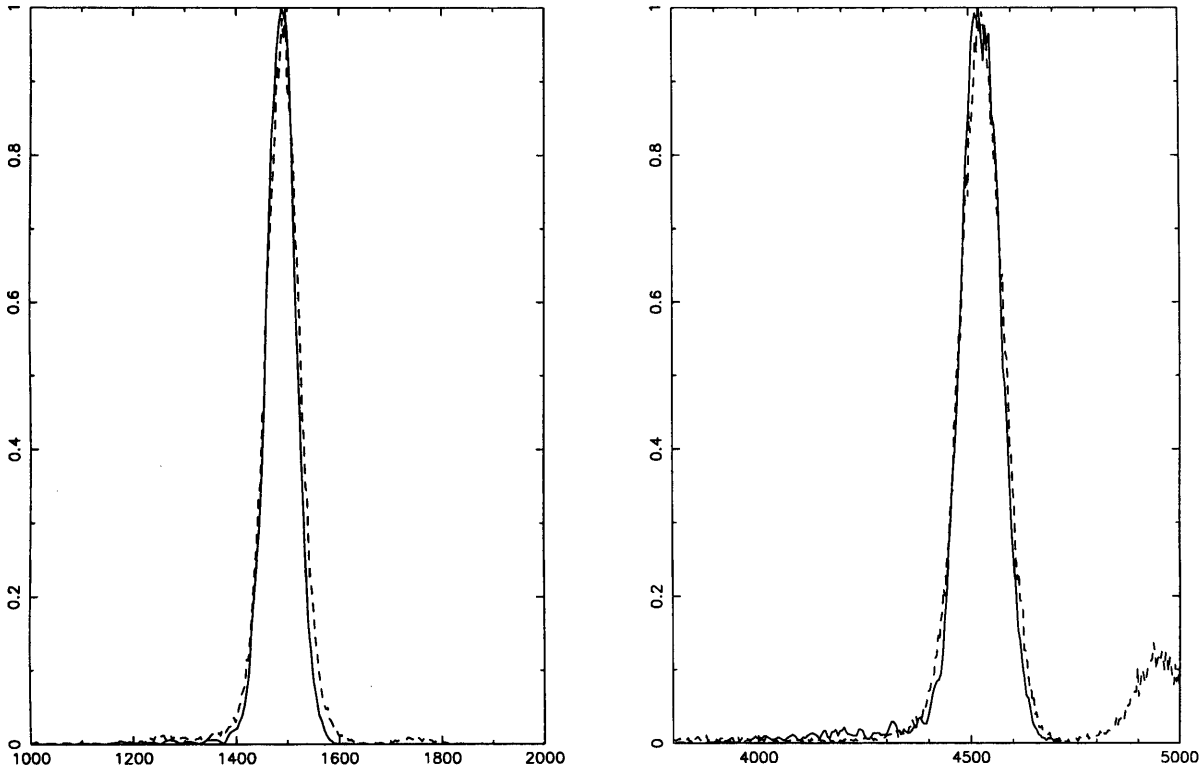

Figure 7.6: A comparison of the spectral response of CUBIC and the model predictions. The plot to the left is for Al(1487eV) and the plot to the right is for Ti(4510 eV). The secondary peak seen on the Ti plot is the X-ray emission from TiKβ which is not included in the simulation.

7.8 Summary

We have calibrated both the quantum efficiency and the spectral resolution of the CUBIC CCD's for a variety of energies between 0.2 and 10 keV. Using these results and models for the theoretical performance we have produced an instrument response matrix. This provides a good interface to general spectral fitting packages such as XSPEC for the analysis of CUBIC data. The calibrations were accurate to the 5 percent level. A good

improvement on this can be made in the future using a broadband calibration technique.

Chapter 8

Conclusions and future expectations

Overview

This chapter gives a review of the investigations into the the local ISM, the soft X-ray background and the performance of CUBIC that are presented in this thesis. In addition the performance and hence impact that future missions will have on this field of study are discussed.

8.1 General Conclusions

This thesis has considered the properties and distribution of the interstellar gas. The cooler components have been mapped through their absorbing effects on the EUV/X-ray spectra of stellar sources (in Chapters 3 and 4) and the hotter components have been investigated through their X-ray emission (in Chapters 6 and 7). Here, I summarise the major points from each chapter and also consider the progress that can be made in these areas in the near future.

In Chapter 3, a sample of 1987 late-type stars which were observed by both the ROSAT and HIPPARCOS satellites was compiled. Two colour diagrams were used to investigate the ability of various spectral models to describe the X-ray/EUV emission from the stars and we found that a two temperature model was the most successful. However, we also found that no single two temperature model could be used to fit the spectra of all the sources. Consequently, we were unable to perform spectral fits to determine the column density towards each source because of the small number of spectral bins available. Instead, we determined $\sim$ 90% confidence limits for the HI column density which allowed for the spectral diversity of the dataset. The resulting sample is amongst the largest of its kind and represents a factor two improvement in sky coverage over the majority of previously published studies. These data were combined with other published data sets in Chapter 4 to enable an investigation of the distribution of cool absorbing gas in the local interstellar medium. We have shown that the best fit model to this distribution is a non-spherical cavity with a constant internal density in the range 0.045-0.08 cm^{-3}. In contrast to previously published work we show that both the distance to the edge of this cavity (and hence also the external density) vary with sky direction. However, the range of distances to the cavity edge that we found using this model (29-280 pc) and the all-sky average of the external density range (0.10-0.85 cm^{-3}), both agree very well with results obtained elsewhere. In fact in some regions there is no evidence for a cavity edge at all and the n_1 density extends to the distance limit of our sample ($\sim$ 1000 pc). The improved resolution offered by these data (scale size $\sim$45 degree^2) also allowed us to identify the two major regions of the sky which demonstrate most variance from a spherical cavity with much more accuracy than previously possible. Perhaps the most interesting result though, comes from

the statistical fluctuations about the best fit model. It was shown that there are significant variations in N_H up to ($\log_{10}(N_H)$=1.4) at scale sizes $<45^0$, which would indicate that the local ISM contains a complex blend of high and low density material with a scale size in the range; 10-100 pc. If this is the case, it will have profound implications on the current understanding of the X-ray background and models for the distribution of material throughout the ISM.

Using the techniques developed in this thesis for studying these kinds of data, much progress can be made in this area in the future. In particular, an initial investigation of all the sources in the ROSAT Bright Source Catalogue shows that a spherical harmonic analysis of hardness ratios alone reveals significant information about the distribution of cool gas across the Galaxy out to distances beyond 1000 pc. The plot in Figure 8.1 shows the map obtained by reconstructing the first 32 harmonics of the 18465 hardness ratios quoted in the RBSC. The hardness ratio itself does not provide a direct measure of absorption, and significant work is required to account for the class of each source and hence its intrinsic emission to quantify the column density to each source. In addition, there is no distance information included for these sources. However, a comparison of the map obtained using these data (see Figure 8.1) with the 0.25 keV map of the X-ray background (see Figure 1.5) reveals excellent spatial correlation. The quality of this correlation is remarkable given that the two data-sets are independent. The 0.25keV map results from the ROSAT all-sky survey data with all the sources removed, while the hardness ratio map represents information from the sources themselves.

Clearly, much progress can be made with a careful analysis of the hardness ratios and this will provide an alternative (and relatively high resolution) picture of the ISM.

Chapter 5 considered the diffuse 0.25 keV emission from a 10 degree^2 region of the sky. The spatial variation in intensity seen across the field was compared to the variation in absorbing column density and its effect corrected for. It was found that residual fluctuations remained in the data with a typical magnitude of 10% and a scale size of $20'$. Detailed modelling of the count-rate distribution expected due to source confusion demonstrated that they were statistically significant, while a spectral analysis revealed that they were most likely explained by variations in the emission measure of halo gas. However, the

Figure 8.1: The RASS hardness ratio smoothed image

possibility that they were caused by variations in absorption column density across the filed-of-view could not be completely ruled out.

In Chapter 6, the study of 0.25 keV emission was extended to other sky directions using data from the ROSAT pointed survey. We found evidence for spatial fluctuations (scale size $20'$ and magnitude $\sim 10\%$) in all of the fields. In fact, the fractional intensity of the fluctuations was shown to be remarkably constant across the sky. After correcting for the effects of absorption, source confusion modelling demonstrated that the fluctuations observed were significant ($> 3\sigma$) in five of the six fields. However, the observation of the plane of the Galaxy did not contain enough counts to prove that the fluctuations were not due to source confusion alone. Assuming that they are not due to source confusion, then there is evidence for fluctuations in every sky direction we have chosen and this would suggest that they are at least partially associated with a local source, since a distant source would be completely absorbed in the Galactic plane. Clearly, further work on Galactic plane observations is required to verify this.

A full understanding of both the true nature of these fluctuations and of the interstellar medium in general awaits improvements in the spectral modelling of hot, non-equilibrium plasmas which should surely result from the large number of new X-ray missions planned for the next decade. The impact that these missions are likely to have is discussed in detail in the next section.

In Chapter 7, the calibration and modelling of the CUBIC CCD's has resulted in the production of an accurate response matrix which should enable the optimum science to be

extracted from observations of the hot, diffuse ISM in the near future. With the simplicity of this instrument, very rapid progress regarding the state and distribution of the plasma in the local ISM should be achieved soon after launch.

8.2 Future Prospects

The launch of several major X-ray observatories in the next few years opens the door to an exciting era for all of the fields of study discussed in this thesis.

The Joint European X-ray Telescope (JETX) which makes up part of the payload on the Spectrum-X mission is due for launch in the very near future. The instrument incorporates a Wolter I telescope (which will provide a total effective area of $\sim$ 200 cm^2 at 5 keV) and CCD detectors which will provide X-ray spectroscopy of medium/bright sources in the energy range: 0.15-10 keV. The energy resolution which will be achieved with these devices will be a considerable improvement on that provided by the ROSAT PSPC and should consequently allow a better determination of the spectral properties of late-type stars and hot (10^6 K) gas.

The Advanced X-ray Astronomy Facility (AXAF), now renamed the Chandra X-ray Observatory, will be launched in 1999. It will provide very high spatial resolution data (5″), capable of resolving the extra-galactic component of the X-ray background (the limiting flux will be $\sim 10^{-16}$ erg cm^{-2} s^{-1}). This will enable a more accurate subtraction of this component of the 0.25 keV emission studied in this thesis.

In contrast to the AXAF mission, the XMM satellite (which was discussed in Chapter two) will offer very high spectral resolution and a high throughput which will enable detailed studies of the spectral emission from hot plasmas. Through expected improvements in thermal emission models which should result result from such data, this will allow a better determination of the temperature, equilibrium state and density of of the interstellar gas. Along with the high effective area of the XMM mirrors, the enhanced low energy QE of the CCD's will provide high sensitivity to the absorption features in the spectra of stellar sources and so provide more reliable HI column densities than could be determined by ROSAT. In addition, as discussed in Chapter 2, XMM will include an optical monitor

which should enable the rapid identification of stellar sources. Clearly, this presents an ideal opportunity to add to the database of stellar sources compiled in Chapter 3.

In addition to the major missions discussed above, the recent and future launches of some smaller satellites will also make a significant impact on the study of hot plasma emission (and hence our understanding of the Local Bubble).

For example, EURD (the Extreme Ultraviolet Spectrograph for the Observation of Diffuse Radiation; Morales *et al.* (1997)) was successfully launched in 1997 and will provide observations of the diffuse emission in the 350-1100 $\AA$ wave-band with a spectral resolution of 4-5 $\AA$. This will clearly provide diagnostics of the physical properties of the gas thought to fill the local cavity. Other proposed missions include CUBICII (see Chapter 7) which will observe the diffuse X-ray emission in the 0.2-10 keV band, and GRADES (the Grating Array Diffuse EUV Spectrometer) which will be optimised for the spectroscopy of diffuse emission in the 90-260 $\AA$ wave-band (Hurwitz *et al.* 1997).

8.2.1 The predicted X-ray performance of XMM

A Monte-Carlo simulation similar to that used for the CUBIC CCD's was used to create a response matrix for the EPIC MOS CCD on XMM and is used here to compare the performance of XMM with ROSAT. The matrix was used in the XSPEC spectral fitting package with the *fakeit* procedure to determine the spectrum observed by the instrument for a given model.

Figure 8.2 shows the spectrum observed by the ROSAT PSPC for a 10^6 K plasma (0.5-2 keV source flux $\sim 2\times 10^{-13}$ ergs cm^{-2} s^{-1} using the Raymond-Smith code) with an absorption column density of 5×10^{19} atoms cm^{-2}, while, Figure 8.3 shows the spectrum observed for the same model by the MOS camera on EPIC. The difference in spectral resolution between the two instruments is clear, while the increased number of counts provided by the much larger effective area of XMM is also evident.

Clearly, if this performance is realised, data returned from XMM will have a significant impact on the studies presented in this thesis. From purely serendipitous source detections

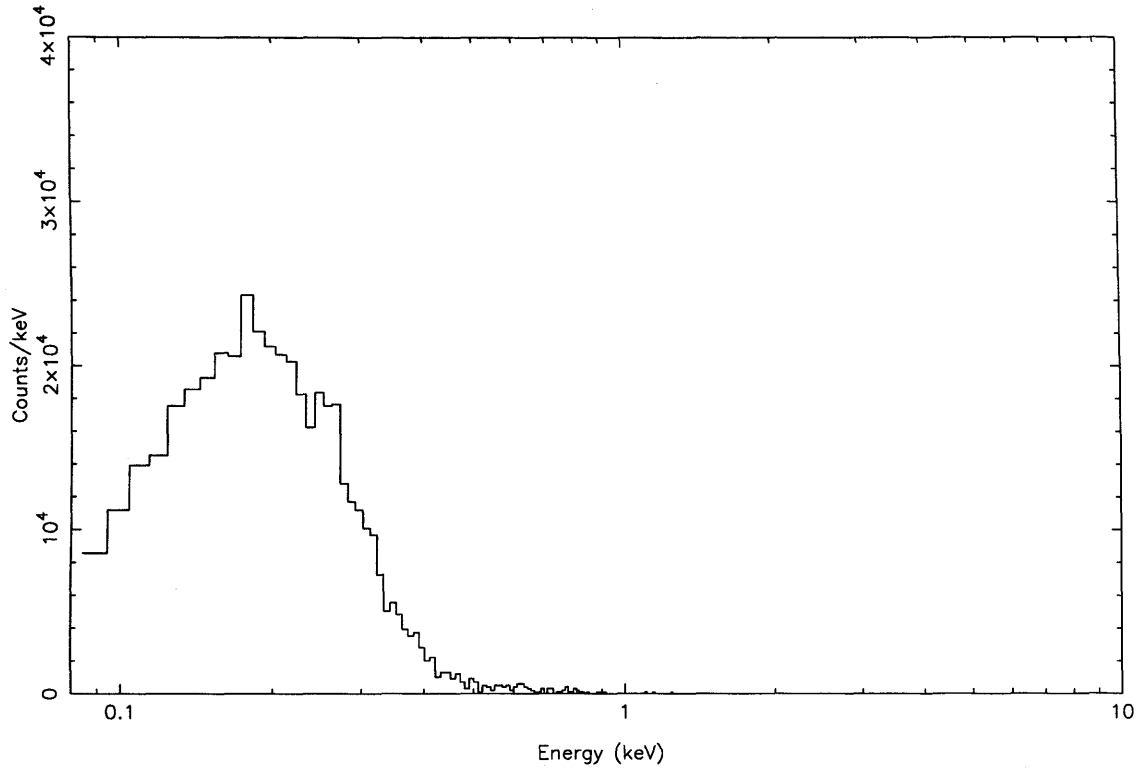

Figure 8.2: The ROSAT PSPC spectrum of a 10^6K plasma with a column density of 5×10^{19} atoms cm^{-2}

alone there will be a very large database with which to investigate late-type star spectra. With improvements to the current spectral models this will lead to a better determination of the line-of-sight HI column density and hence more accurate maps of the cool gas in the local ISM. In addition, the improvements in determining line energies and equivalent widths will result in a better understanding of the conditions in the ISM leading to better models for the dynamic nature of the interstellar medium.

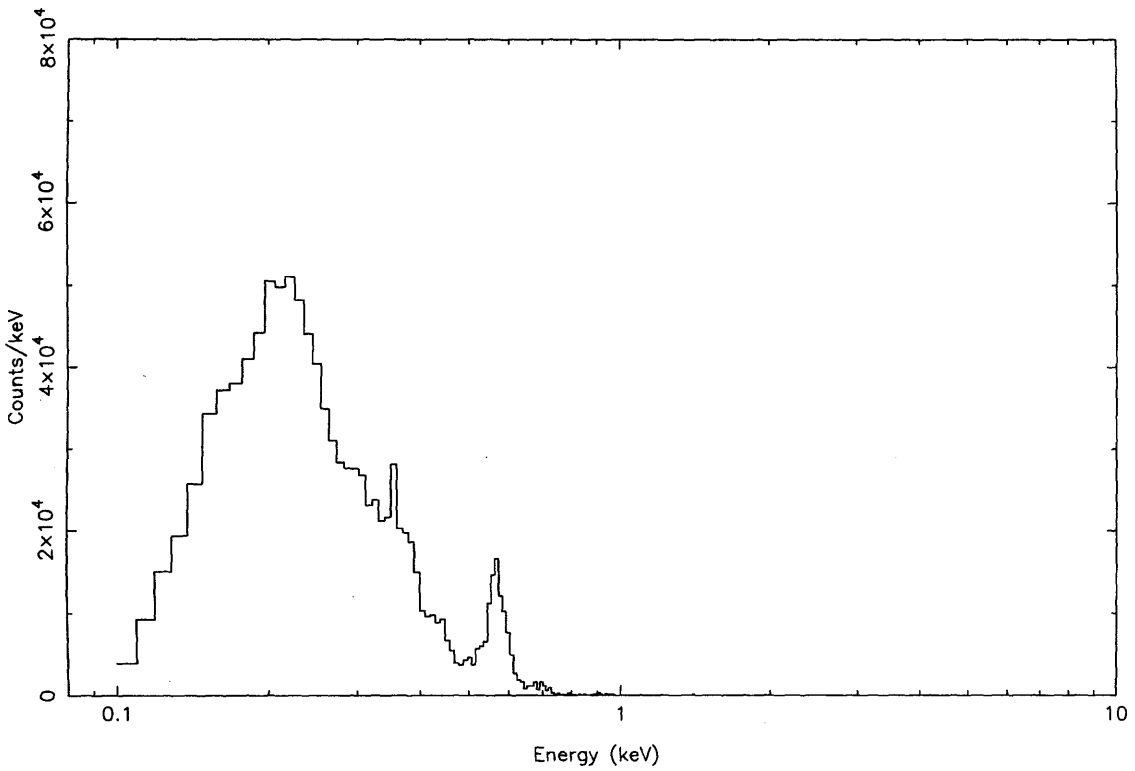

Figure 8.3: The XMM EPIC-MOS spectrum of a 10^6K plasma with a column density of $5\times$ 10^{19} atoms cm^{-2}

References

Adams, D. J. *Cosmic X-ray Astronomy.* Adam Hilger Ltd, 1980.

Aschenbach, B., 1988. *Appl. Opt.*, **27**, 1404.

Barber, C., Roberts, T. & Warwick, R., 1996. *Mon. Not. R. astr. Soc.*, **282**, 157.

Barber, C. R., Warwick, R. S. & Snowden, S., 1996. In: *Röntgenstrahlung from the Universe*, Zimmerman, H. U., Trümper, J. E. & Yorke, H., eds., MPE Report, p. 319.

Barber, C. R., 1994. *PhD thesis*, University of Leicester.

Bertolini, G. & Coche, A. *Semiconductor devices.* Elsevoir-North Holland Amsterdam, 1968.

Bevington, P. R. & Robinson, D. K. *Data Reduction and Error Analysis for the Physical Sciences.* Mc Graw-Hill, 1992.

Bloch, J., Jahoda, K., Juda, M., McCammon, D., Sanders, W. & Snowden, S., 1986. *Astrophys. J. Letts.*, **308**, 59.

Bohlin, R., Savage, B. & Drake, J., 1978. *Astrophys. J.*, **224**, 132.

Boulanger, F. & Perault, M., 1988. *Astrophys. J.*, **330**, 964.

Bowyer, S. *et al.*, 1994. *Astrophys. J. Suppl.*, **93**, 569.

Bowyer, S. *et al.*, 1996. *Astrophys. J. Suppl.*, **102**, 129.

Bowyer, C., Field, G. & Mack, J., 1968. *Nature*, **217**, 32.

Briel, U. G. *et al. The ROSAT User's Handbook.* MPE, 1994.

Brinkmann, A. C., Harts, H. J., Den Boggende, A. J., Bootsma, T. M., Dubbedam, L., Den Herder, J.-W., Kaastra, J. S., De Korte, P. A., Van Leeuwen, B. J., Mewe, R., Van Zwet, E. J., Decker, T. A., Hailey, C. J., Kahn, S. M., Paerels, F. B., Pratuch, S. M., Rasmussen, A., Branduardi-Raymont, G., Guttridge, P., Bixler, J. V., Thomsen, K., Zehnder, A. & Erd, C., 1996. In: *EUV, X-ray and Gamma-ray*

instrumentation for astronomy VII, Siegmund, O. H. & Gummin, M. A., eds., SPIE vol. 2808, p. 463.

Burrows, D. & Mendenhall, J., 1991. *Nature*, **351**, 629.

Burrows, D., McCammon, D., Sanders, W. & Kraushaar, W., 1984. *Astrophys. J.*, **287**, 208.

Burrows, D., Singh, K., Nousek, J., Garmire, G. & Good, J., 1993. *Astrophys. J.*, **406**, 97.

Burrows, D. *et al.*, 1995a. *Proc. SPIE Int. Soc. Opt. Eng.*, **2518**, 163.

Burrows, D. N., Skinner, M. A., Catalano, M. A., Cawley, L., Cocklin, E. J., Engel, L. G., Entingh, T. J., Garmire, G. P., Green, R., Janches, D., Kelly, D. A., Mendenhall, J. A., Nousek, J. A., Lumb, D., Holland, A. & Pool, P., 1995b. *Proc. SPIE Int. Soc. Opt. Eng.*, **2518**, 141.

Buscombe, W. *General Catalogue of MK spectral Classifications, volumes 7-10 Northwestern University, Evanston Illinois.* 1992.

Ciaravella, A., Peres, G., Maggio, A. & Serio, S., 1996. *Astr. Astrophys.*, **306**, 553.

Cox, D. & Anderson, P., 1982. *Astrophys. J.*, **253**, 268.

Cox, D. & Reynolds, R., 1987. *Ann. Rev. Astron. Astrophys.*, **25**, 303.

Cox, D., 1981. *Astrophys. J.*, **245**, 534.

Diamond, C., Jewell, S. & Ponman, T., 1995. *Mon. Not. R. astr. Soc.*, **274**, 589.

Dickey, J. & Lockman, F., 1990. *Ann. Rev. Astron. Astrophys.*, **28**, 215.

Egger, R., 1997. In: *The Local Bubble and Beyond*, Breitschwerdt, D., Freyberg, M. & Trümper, J., eds., Springer, p. 287.

Everhart, T. P. & Hoff, P. H., 1971. *Appl. Phys.*, **42**, 5837.

Fabian, A. C. & Barcons, X., 1992. *Ann. Rev. Astron. Astrophys.*, **30**, 429.

Fano, U., 1947. *Physical Review*, **72**, 26.

Ferlet, R., Vidal-Madjar, A. & Gry, C., 1985. *Astrophys. J.*, **298**, 838.

Field, G., Goldsmith, D. & Habing, H., 1969. *Astrophys. J. Letts.*, **55**, 149.

Fitting, H., Glaefeke, H. & Wild, W., 1977. *Phys. Status Solidi A*, **43**, 185.

Fraser, G. *X-ray Detectors in Astronomy.* Cambridge University Press, 1989.

Fried, P., Nousek, J., Sanders, W. & Kraushaar, W., 1980. *Astrophys. J.*, **242**, 987.

Frisch, P. & York, D., 1983. *Astrophys. J. Letts.*, **271**, 59.

Fruscione, A., Hawkins, I., Jelinsky, P. & Wiercigroch, A., 1994. *Astrophys. J. Suppl.*, **94**, 127.

Georgantopoulos, I., Stewart, G. C., Shanks, T., Boyle, B. J. & Griffiths, R. E., 1996. *Mon. Not. R. astr. Soc.*, **280**, 276.

Grove, A. S. *Physics and Technology of Semiconductor Devices.* Wiley, 1967.

Gry, C., York, D. & Vidal-Madjar, A., 1985. *Astrophys. J.*, **296**, 593.

Hasinger, G., Burg, R., Giacconi, R., Hartner, G., Schmidt, M., Trümper, J. & Zamorani, G., 1993. *Astr. Astrophys.*, **275**, 1.

Hasinger, G. *The X-ray background.* Cambridge University Press, 1992.

Heiles, C., Kulkarni, S. & Stark, A., 1981. *Astrophys. J. Letts.*, **247**, 73.

Holland, A. D., Turner, M. J., Abbey, A. F. & Pool, P., 1996. In: *EUV, X-ray and Gamma-ray instrumentation for astronomy VII*, Siegmund, O. H. & Gummin, M. A., eds., SPIE vol. 2808, p. 414.

Holland, A., 1990. *PhD thesis*, University of Leicester.

Hopkinson, G., 1987. *Proc. SPIE Int. Soc. Opt. Eng.*, **26**, 766.

Hurwitz, M., McKee, C., Edelstein, J., Vallerga, J., Jelinsky, P., Freyberg, M. & Breitschwerdt, D., 1997. In: *The Local Bubble and Beyond*, Breitschwerdt, D., Freyberg, M. & Trümper, J., eds., Springer, p. 91.

Iwan, D., Marshall, F. E., Shafer, R. F. & Stottlemyer, R. A., 1982. *Astrophys. J.*, **260**,

111.

Iwan, D., 1980. *Astrophys. J.*, **239**, 316.

J. Nousek, P. F., Sanders, W. & Kraushaar, W., 1982. *Astrophys. J.*, **258**, 83.

Jacchia, L. G., 1972. *COSPAR International Reference Atmosphere 1972 compiled by The Committee for CIRA of COSPAR Working Group 4 Akademie-Verlag Berlin*, , 227.

Jahoda, K., McCammon, D., Dickey, J. & Lockman, F., 1985. *Astrophys. J.*, **290**, 229.

Jahoda, K., Lockman, F. & McCammon, D., 1990. *Astrophys. J.*, **364**, 1.

Jahoda, K., McCammon, D. & Lockman, F., 1986. *Astrophys. J. Letts.*, **311**, 57.

Janesick, J., Elliot, T., Collins, S., Daud, T., Campbell, T. & Dingzian, A., 1985. *Proc. SPIE Int. Soc. Opt. Eng.*, **597**, 364.

Kahn, F., 1997. In: *The Local Bubble and Beyond*, Breitschwerdt, D., Freyberg, M. & Trümper, J., eds., Springer, p. 483.

Keay, A., 1997. *PhD thesis*, University of Leicester.

Lockman, F., Jahoda, K. & McCammon, D., 1986. *Astrophys. J. Letts.*, **302**, 432.

Longair, M. S. *High Energy Astrophysics, Volume 2.* 1994.

Maggio, A. & Peres, G., 1996. *Astr. Astrophys.*, **306**, 563.

Marsh, M., Barstow, M., Buckley, D., Burleigh, M., Holberg, J., Koester, D., O'Donoghue, D., Penny, A. & Sansom, A., 1997. *Mon. Not. R. astr. Soc.*, **287**, 705.

Marshall, F. E. & Clark, G. W., 1984. *Astrophys. J.*, **287**, 633.

Mason, K. *et al.*, 1995a. *Mon. Not. R. astr. Soc.*, **274**, 1194.

Mason, K. O., Bignami, G. F., Brinkman, A. C. & Peacock, A., 1995b. *Adv. Space Res.*, **16**, 41.

Mason, K. O., Cropper, M. S., Hunt, R., S, D, H., Priedhorsky, W. C., Ho, C., Cordova, F. A., Jamar, C. A. & Antonello, E., 1996. In: *EUV, X-ray and Gamma-ray instrumentation for astronomy VII*, Siegmund, O. H. & Gummin, M. A., eds., SPIE vol.

2808, p. 438.

McCammon, D., Burrows, D., Sanders, D. & Kraushaar, W., 1983. *Astrophys. J.*, **269**, 107.

McClintock, W., Henry, R., Moos, H. & Linsky, J., 1976. *Astrophys. J. Letts.*, **204**, 103.

Meidinger, N., Bräuninger, H. W., Hartmann, R., Hartner, G., Krause, N., Metzner, G., Pfeffermann, E., Popp, M., Reppin, C., Reidel, J., Stoetter, D., Strueder, L., Trümper, J., Weber, U., Hauff, D., Holl, P., Kemmer, J., Krisch, S., Soltau, H., Van Zanthier, C., Bihler, E., Boettcher, H., Kendziorra, E., Kraemar, J., Pflueger, B. & Staubert, R., 1996. In: *EUV, X-ray and Gamma-ray instrumentation for astronomy VII*, Siegmund, O. H. & Gummin, M. A., eds., SPIE vol. 2808, p. 492.

Mewe, R., Gronenschild, E. & VandenOord, G., 1985. *Astr. Astrophys. Suppl.*, **62**, 197.

Mewe, R., Lemen, J. R. & VandenOord, G., 1986. *Astr. Astrophys. Suppl.*, **65**, 511.

Morales, C., Trapero, J., Gomez, J. F., Bowyer, S., Edelstein, J. & Lampton, M., 1997. In: *The Local Bubble and Beyond*, Breitschwerdt, D., Freyberg, M. & Trümper, J., eds., Springer, p. 41.

Morrison, R. & McCammon, D., 1983. *Astrophys. J.*, **270**, 119.

Owens, A., Abbey, A. F., Brauninger, H., Burkert, W., Castelli, C., Chapman, H., Dowson, J., Li, Y., McCarthy, K., Pool, P., Sims, M., Spragg, J., Watson, D. J., Wells, A. & Willingale, R., 1996. *Journal of X-ray Science and Technology*, .

Pallavicini, R., 1989. *Astr. Astrophys. Review*, **1**, 177.

Paresce, F., 1984. *Astron. J.*, **89**, 1022.

Plucinsky, P. P., Snowden, S. L., Briel, U., Hasinger, G. & Pfeffermann, E., 1993. *Astrophys. J.*, **418**, 519.

Pounds, K. A. *et al.*, 1993. *Mon. Not. R. astr. Soc.*, **260**, 77.

Preibisch, T., 1997. *Astr. Astrophys.*, **320**, 525.

Pye, J. P. *et al.*, 1995. *Mon. Not. R. astr. Soc.*, **274**, 1165.

Raymond, J. C. & Smith, B., 1977. *Astrophys. J. Suppl.*, **35**, 419.

Raymond, J. C. *Hot Thin Plasmas in Astrophysics.* Kluwer, 1988.

Rocchia, R. *et al.*, 1984. *Astr. Astrophys.*, **130**, 53.

Sanders, W., Kraushaar, W., Nousek, J. & Fried, P., 1977. *Astrophys. J. Letts.*, **217**, 87.

Schlegel, D., Finkbeiner, D. & Davis, M., 1997. *Astr. Astrophys. Suppl.*, **191**, 8704.

Schmitt, J., Collura, A., Sciortino, S., Valana, G., Harnden, F. & Rosner, R., 1990. *Astrophys. J.*, **365**, 704.

Shapiro, P. & Field, G., 1976. *Astrophys. J.*, **205**, 762.

Sims, M. R. *et al.*, 1990. *Opt. Eng.*, **26**, 649.

Snowden, S. L. & Freyberg, M. J., 1993. *Astron. J.*, **404**, 403.

Snowden, S. L., Cox, D., McCammon, D. & Sanders, W., 1990. *Astrophys. J.*, **354**, 211.

Snowden, S. L. *et al.*, 1991. *Science*, **252**, 1529.

Snowden, S. L., Plucinsky, P. P., Briel, U., Hasinger, G. & Pfeffermann, E., 1992. *Astrophys. J.*, **393**, 819.

Snowden, S. L., Hasinger, G., Jahoda, K., Lockman, F., McCammon, D. & W.Sanders, 1994a. *Astrophys. J.*, **430**, 601.

Snowden, S. L., McCammon, D., Burrows, D. N. & Mendenhall, J. A., 1994b. *Astrophys. J.*, **424**, 714.

Snowden, S. L., Egger, R., Freyberg, M., McCammon, D., Plucinsky, P., Sanders, W., Schmitt, J. & Voges, J. T. W., 1997. *Astrophys. J.*, **485**, 125.

Snowden, S. L., Egger, R., Finkbeiner, D., Freyberg, M. & Plucinsky, P., 1998. *Astrophys. J.*, **493**, 715.

Snowden, S. L. *Cookbook for analysis procedures for ROSAT XRT/PSPC Observations of Extended Objects and the Diffuse Background.* GSFC, 1994.

Spitzer, L. & Jenkins, E. B., 1975. *Ann. Rev. Astron. Astrophys.*, **13**, 133.

Spitzer, L., 1956. *Astrophys. J.*, **124**, 420.

Spitzer, L. *Physical processes in the interstellar medium.* Wiley, 1978.

Stark, A. A., Gammie, C. F., Wilson, R. W., Bally, J., Linke, R. A., Heiles, C. & Hurwitz, M., 1992. *Astrophys. J. Suppl.*, **79**, 77.

Trümper, J., 1984. *Physica Scripta*, **7**, 209.

Vaiana, G. S. *et al.*, 1981. *Astrophys. J.*, **245**, 163.

Vallerga, J., 1996. *Space Sci. Rev.*, **78**, 277.

Villa, G. E., Abbey, A. F., Arnaud, M., Balasini, M., Bignami, G. F., Boer, M., Brauninger, H., Butler, I., Cafagna, G., Cara, C., Chabaud, C., Chiappetti, L., Cole, R. E., Conte, M., Dowson, J., Dhez, P., Duc, R., Di Cocco, G., Ferrando, P., Goddall, C. V., Hippman, H., Kendziorra, A. D. H. E., Labeque, A., Meidinger, N., Moriggio, C., La Palombara, N., Musso, C., Poindron, E., Peres, G., Pferrerman, E., Pigot, C., Pye, J. P., Reppin, C., Schmidt, D., Sciortino, S., Serio, S., Spragg, J., Stephen, J. B., Struder, L., Trifoglio, M., Tua, P., Turner, M. J. & Whitehead, S., 1996. In: *EUV, X-ray and Gamma-ray instrumentation for astronomy VII*, Siegmund, O. H. & Gummin, M. A., eds., SPIE vol. 2808, p. 402.

Warwick, R., Barber, C., Hodgkin, S. & Pye, J. P., 1993. *Mon. Not. R. astr. Soc.*, **262**, 289.

Warwick, R. S., Pye, J. P. & Fabian, A. C., 1980. *Mon. Not. R. astr. Soc.*, **190**, 243.

Wells, A. *et al.*, 1990. *Proc. IAU Colloquium.*, **115**, 318.

Welsh, B., Crifo, F. & Lallement, R., 1998. *Astr. Astrophys.*, **333**, 101.

Welsh, B., Craig, N., Vedder, P. & Vallerga, J., 1994. *Astrophys. J.*, **437**, 638.

Welsh, B., Vedder, P. & Vallerga, J., 1990. *Astrophys. J.*, **358**, 473.

Welsh, B., 1991. *Astrophys. J.*, **373**, 556.

Worral, D., Marshall, F., Boldt, E. & Swank, J., 1982. *Astrophys. J.*, **255**, 111.

Dedication.

This thesis is dedicated to my wife, Lindsey and to my family for their endless support and encouragement. Thankyou.

Acknowledgements.

I would particularly like to thank my supervisor, Dick Willingale, for his encouragement, understanding and most importantly, patience. I would also like to thank Bob Warwick for giving me the opportunity to study at Leicester and for his invaluable help and direction (especially post CUBIC). Thanks also go to Andrew Holland for his help in the lab and to Geoff Mellor, Geoff Martin and Harby for maintaining the computers so well. Finally, I also gratefully acknowledge the help and advice given by Colin Barber and many other members of the XRA group.